

Structural controls on fluid flow in carbonate rocks: quantitative insights from the Maltese Islands

Master of Petroleum Geoscience

Vilde Dimmen



Department of Earth Science

University of Bergen

November, 2016

Abstract

This MSc thesis documents and quantifies the relationship between structural complexity and fluid flow through field based studies carried out in excellent outcrops along the coast of the Maltese Islands.

There is a wide agreement in the literature today that faults and fractures exert strong controls on fluid flow and fluid-rock interactions in the shallow crust. Faults and fractures are known to act as conduits and/or barriers to fluid migration, in which locations of structural complexity such as relay zones and fault intersections, have been found to be particularly prone to act as loci for focused fluid flow. Such zones are found to contribute with higher fracture density, higher connectivity, and to a certain degree wider fracture apertures than less complex zones. This can influence a wide range of fluid types, including magma, hydrocarbons, and hydrothermal and mineralizing fluids. Structural complexity may therefore control a series of different processes in the Earth's crust and is an important field of study.

Despite this wide recognition of structural control on fluid flow, there are currently no studies that systematically and directly quantify this relationship. This lack of documentation is where the motive for this study lies. To fill this gap, topological and geometric characterization of fracture systems in carbonate rocks has been conducted. Conjugant evidence of paleo-fluid flow in the form of diagenetically altered zones and localized cementation rates associated with the structures have been documented, and their varying extent are used to describe the amount of the fluid flow. The results show a direct relationship between the degree of structural complexity and evidence for paleo-fluid flow, as areas of increased cementation coincide with structurally complex zones, and the extent of redox fronts increases around zones of higher structural complexity.

These findings have a wide range of application, and concerns both environmental, scientific and economic aspects through the implications structural complexity has on fluid flow concerning e.g. CO₂ storage, ore deposition, hydrocarbon leakage, earthquake localization (by affecting pore fluid pressure), contamination of ground water, and more.

Acknowledgements

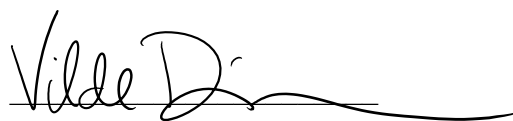
This study is part of my MSc degree in Structural Geology at the Department of Earth Science, University of Bergen, and would not have been possible without guidance and feedback from several contributors. First and foremost, I would like to thank my supervisor Prof. Atle Rotevatn for endless guidance, support, and motivation during the last two years. Thank you for sharing your knowledge and keeping me on the right track. In addition to Atle, I would like to thank Thomas B. Kristensen, Casey Nixon, David Peacock, Ulrike Freitag, and Arild Andresen for great company and inspiring discussions during the weeks of fieldwork in Malta.

A special thanks to Casey for introducing me to topology and teaching me ArcGIS, and to David for providing constructive reviews on my written work. Ray Leadbitter at the Independent Petrographic Services in Aberdeen is thanked for preparing excellent thin sections, and Irene Heggstad is thanked for assistance regarding the Scanning Electron Microscope. Irina Korneva and Toms Buls are thanked for guiding me through ImageJ and teaching me how to carry out the porosity estimations. I would also like to express my gratitude to Gunnar Sælen for his input on the part regarding sedimentology and thin section analysis, and for carrying out statistics on my porosity estimations.

I am also very grateful to Marthe Førland, Ingvild Blækkan, Synne S. Ågotnes, and Karoline Ertesvåg for proof reading, feedback, and instructions regarding software utilized throughout the project.

BKK are acknowledged for funding the fieldwork for this study through the BKK-UiB agreement.

Anna and Charles at Maple Farm B&B deserve special thanks for the outstanding hospitality and kindness they showed us during our fieldwork. And last, but definitely not least, I would like to thank my field partner, Kari Nærland, for excellent company, support, discussions, and lots of good memories throughout these years.

A handwritten signature in black ink, reading "Vilde Dimmen". The signature is written in a cursive style with a long, sweeping underline that extends to the right.

Vilde Dimmen

Bergen, November 2016

CONTENTS

1 INTRODUCTION	1
1.1 Background and rationale.....	1
1.2 Aims and objectives.....	2
1.3 Study area and locality characteristics.....	2
1.3.1 <i>Study area</i>	2
1.3.2 <i>Locality types and working hypotheses</i>	3
1.4 Thesis outline.....	4
2 GEOLOGICAL FRAMEWORK	7
2.1 Regional tectonic framework.....	7
2.1.1 <i>Tectonic Evolution of the Mediterranean Region</i>	7
2.1.2 <i>The Pelagian Platform</i>	7
2.1.3 <i>The Maltese Islands</i>	9
2.2 Regional stratigraphic framework.....	10
2.2.1 <i>Pre-rift succession</i>	11
2.2.2 <i>Syn-rift succession</i>	12
2.2.3 <i>Post-rift phase</i>	13
3 THEORETICAL BACKGROUND	15
3.1 Evolution of faults and damage zones.....	15
3.1.1 <i>Single fault geometries</i>	15
3.1.2 <i>Fault linkage and growth</i>	16
3.1.3 <i>Fault zone architecture</i>	18
3.2 Structural controls on fluid flow.....	20
3.3 Topology.....	21
3.3.1 <i>Origin and area of application</i>	21
3.3.2 <i>Nomenclature of topological elements</i>	23
4 METHODOLOGY	25
4.1 Field data.....	25
4.1.1 <i>Sedimentological logging</i>	25
4.1.2 <i>Topography profiles</i>	26
4.1.3 <i>Topology: preparatory data sampling in the field</i>	26
4.2 Topological characterization of the studied fracture networks: image based data collection and analysis using ArcGIS.....	26
4.3 Microscopic analysis.....	28
4.3.1 <i>Regular Light Microscopy</i>	28
4.3.2 <i>Scanning Electron Microscopy</i>	28
4.4 Image analysis for porosity determination.....	30
4.4.1 <i>Image analysis of photomicrographs</i>	30
4.4.2 <i>Image analysis of BSE-SEM images</i>	31
4.4.3 <i>Uncertainties related to the image-based porosity analysis</i>	31
5 RESULTS	33
5.1 Structure and stratigraphy of the study area at Ras ir Raheb.....	33
5.1.1 <i>Structural framework</i>	33
5.1.2 <i>Stratigraphic framework</i>	34
5.2 Host rock characterization.....	36
5.3 Mound-type localities at Ras ir Raheb.....	41

5.3.2 Mound locality V2.....	44
5.3.3 Mound locality V4.....	46
5.3.4 Mound locality V7.....	48
5.3.5 Mound locality V8.....	50
5.3.6 Mound locality V9.....	52
5.4 Porosity and connectivity	54
5.4.1 Mound vs. Host porosity.....	54
5.4.2 Porosity statistics.....	57
5.5 Redox-type localities at Ras ir Raheb.....	59
5.5.1 Redox locality V5.....	59
5.5.2 Redox locality V6.....	62
5.6 Redox-type localities at Marsalforn (Gozo)	64
5.6.1 Local structure and stratigraphy of the Marsalforn study area	64
5.6.2 Redox locality V10, Gozo.....	64
5.7 Summary of results.....	65
6. DISCUSSION	67
6.1 What does the preferential location of mounds and redox fronts at structurally complex areas tell us?.....	67
6.2 How do the structurally complex zones form, and what is their role in controlling the localization of flow and fluid-rock interaction?	69
6.3 An additional aspect of preferential flow localization in the redox-type localities.....	72
6.4 Why are structural controls on fluid flow important to understand?.....	74
7. FINAL CONCLUSIONS AND FURTHER WORK.....	79
7.1 Conclusions	79
7.2 Suggestions for further work	80
8. REFERENCES.....	81
Appendix I: Locality overviews	89
Appendix II: ArcGIS workflow	109
Appendix III: ImageJ workflow	117

1 INTRODUCTION

1.1 Background and rationale

Faults and fractures may exert strong controls on fluid flow and fluid-rock interaction in the shallow crust, where they are known to be able to act as conduits, barriers, or a combination of the two (Jolley et al., 2007). On the scale of single faults, important factors that control the flow properties include type and distribution of damage zone structures, fault core composition, cementation, timing and more (Caine et al., 1996, Jolley et al., 2007). At the scale of fault and fracture networks (*sensu* Peacock et al., 2016), important factors to consider include the locations of fault zone complexity, such as relay zones or fault intersections, as these are particularly prone to act as loci for focused fluid flow (Gartrell et al., 2004, Fossen and Rotevatn, 2016). Such complex zones can affect several types of fluids, including magma, hydrocarbons, and groundwater, which may further influence a wide variety of processes in the Earth's crust within different categories, like geo-hazards and natural resources. The flow of fluids of various types in relation to structural complexity have been a subject in several studies through time, (e.g. Oliver, 1996, Caine and Forster, 1999, Eichhubl et al., 2000, Bense and Van Balen, 2004, Dockrill and Shipton, 2010, Davidson et al., 2016, Ono et al., 2016). All of these studies contribute to the well-established agreement that there is a connection between structural complexity and fluid flow, through e.g. deformation-driven dilation during metamorphism (Oliver, 1996), fluid seepage related to faults and folds (Eichhubl et al., 2000), relay zones and clay smearing in relation to groundwater flow patterns (Bense and Van Balen, 2004), and through fracture filling mineralization as an indicator of fluid-rock interactions (Ono et al., 2016). However, there are currently no studies that systematically and directly document and, in particular, *quantitatively* explore this relationship. It is a goal of this study to do so.

The project is based upon data collected through fieldwork in a Miocene-age carbonate succession located in exceptionally well-exposed outcrops in Malta, looking at structurally complex zones in relation to evidence of paleo-fluid flow. To quantify structural complexity and connectivity, a method that analyses the *topology* of fault and fracture networks will be used (Manzocchi, 2002, Sanderson and Nixon, 2015). Knowledge of the network connectivity is crucial for the understanding of fluid flow through a rock body, and a topological characterization can give a more direct approach to the connectivity of the fracture network than traditional geometric characterizations (see Section 4.2 for full description of methods).

1.2 Aims and objectives

The main aims of this project are to improve the understanding of structurally controlled fluid flow, and to constrain and quantify the relationship between paleo-fluid flow and structural complexity through field-based investigations. The aims are achieved through the specific objectives listed below:

- i) Document and characterize the geometry and topology of small-scale fault (displacement generally < 1 m) and fracture networks in carbonate rocks.
- ii) Document evidence for paleo-fluid flow, in the form of diagenetically altered zones, and constrain their spatial relationship to the studied fault and fracture networks.
- iii) Determine the porosity, and variability thereof, in host rocks and in areas of elevated structural complexity.

1.3 Study area and locality characteristics

1.3.1 Study area

This project is based on fieldwork carried out on the Maltese Islands in the Central Mediterranean (Fig. 1.1a). The Maltese Islands are comprised of the islands of Malta, Comino and Gozo, located within the Pelagian Platform on the north-eastern shoulder of the WNW-ESE trending Pantelleria Rift system, about 95 km south of Sicily and 290 km east of Tunisia (Pedley et al., 1976, Micallef et al., 2013). Normal faulting is widespread, as ENE-WSW trending horst and graben structures dominate the archipelago (Fig. 1.1b) (Dart et al., 1993). The distinct Victoria Lines Fault is the largest fault on Malta, and marks the southernmost extent of the horst and graben structures. The only onshore tectonic feature with the same trend as the Pantelleria Rift system is the Maghlaq Fault on the southwestern coast of Malta (Pedley et al., 1976, Illies, 1981). The islands provide a rare opportunity to study the Pantelleria Rift-related Oligocene-Miocene succession above sea level (Reuther and Eisbacher, 1985, Micallef et al., 2013). The main study area used in this project, is located on the western coast of Malta, just south of Ras ir Raheb (Fig. 1.1b). Additionally, one locality on the northern coast of the island of Gozo was used (Fig. 1.1b).

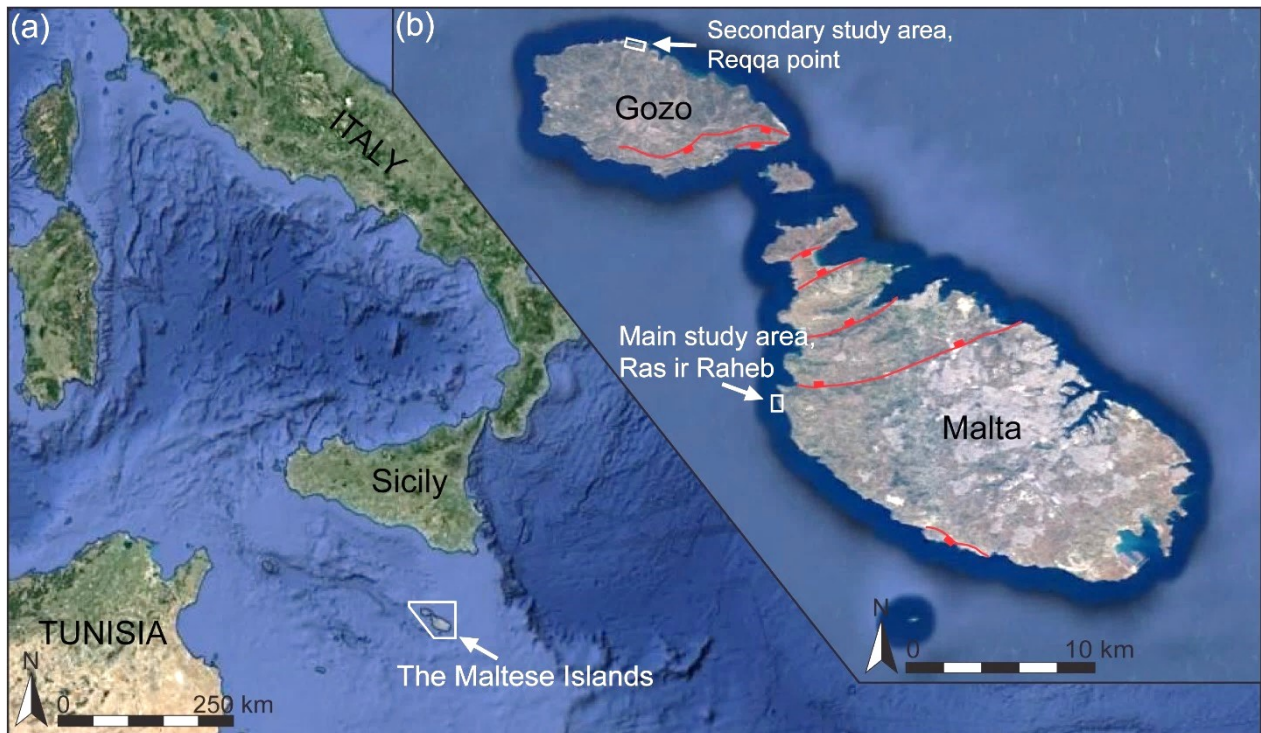


Figure 1.1. (a) Satellite photo of the central Mediterranean, pointing out the Maltese Islands. (b) Satellite photo, zooming in on the the Maltese Islands, pointing out the two study areas, Reqqa point and Ras ir Raheb. Red lines mark the main extensional faults. Imagery courtesy of Google Earth, after Dart et al. (1993).

1.3.2 Locality types and working hypotheses

Two distinct types of localities were used in this study:

1. The first type of localities that will be presented will be referred to as *mound-type localities* throughout this thesis. These localities constitute shorter sections of fracture networks related to the damage zones of small faults (displacement up to 7 m, but generally less than 1 m), generally 2-4 m long and 1-2 m wide. A characteristic feature of these localities is localized topographic highs, or mounds, which are found along fracture networks, typically in areas with higher structural complexity (Fig. 1.2). The mounds generally exhibit an elliptical shape and vary in size, from 10 cm up to 80 cm in diameter. These localities were chosen based on the fact that their relief variations appeared to coincide with structural complexity. Based on this the hypothesis that their formation was related to focused/localized cementation in areas of high structural complexity was set; the testing of this hypothesis drove the data collection.
2. The second type of localities will be referred to as *redox-type localities*. These localities show little to no change in the topographic relief, and their fracture networks are generally simpler. These localities were chosen because they show redox halos (sensu Ogata et al., 2014), or rims, that vary throughout the studied fracture networks (Fig.

1.3). The working hypotheses for these localities were that the width of the redox fronts were controlled by the level of structural complexity; the testing of this hypothesis drove the data collection for these localities.

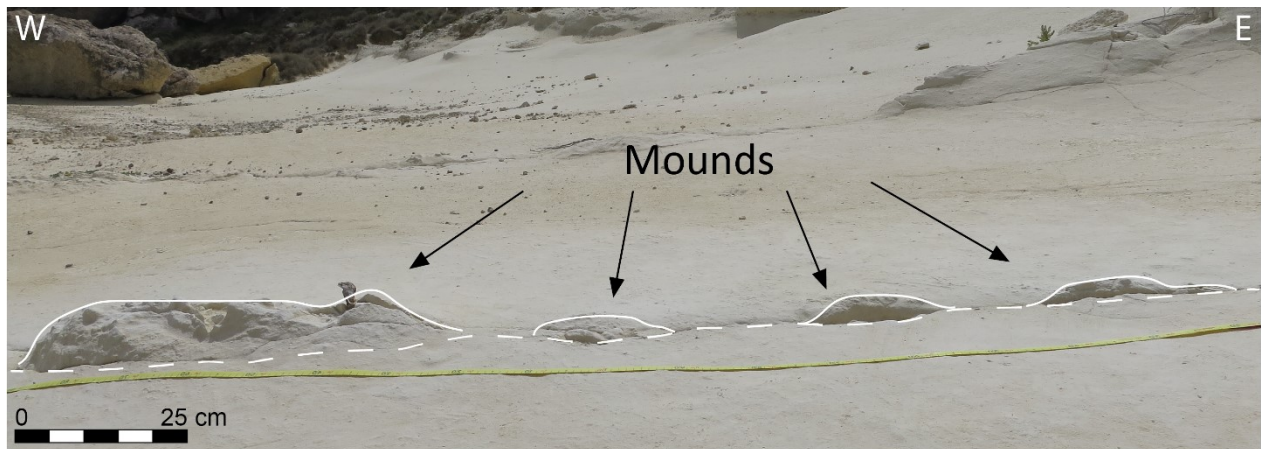


Figure 1.2. Field photo, illustrating the appearance of a mound-type locality. A large mound can be observed in the western end of the photo, and three smaller mounds towards the east. The dashed line indicates the base of the fracture network.

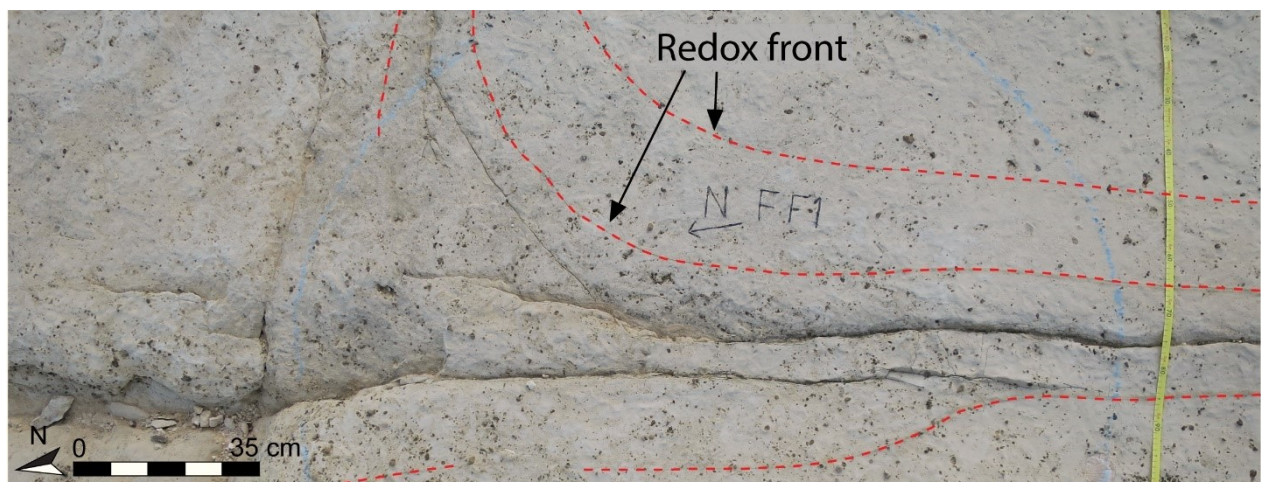


Figure 1.3. Field photo, illustrating the appearance of a redox-type locality. The red, dashed lines highlight the redox fronts surrounding the fault and fracture network.

1.4 Thesis outline

Following this introductory chapter, Chapter 2 will introduce the tectonic evolution of the Mediterranean, focusing on the Pelagian Platform in the Central Mediterranean, and present the tectonic and stratigraphic framework of the Maltese Islands. Chapter 3 provides a short overview of the terminology and theory concerning the evolution of faults and fault damage zones, structural control on fluid flow, and topology, as a backdrop for the following chapters. Chapter 4 presents the methods used, both in the field and for the following analysis. The results from the fieldwork and following analyses will be presented in Chapter 5, The results will be

interpreted and discussed in Chapter 6, after which conclusions and suggestions for further work are presented in Chapter 7.

2 GEOLOGICAL FRAMEWORK

This chapter introduces the tectonic evolution of the Mediterranean, focusing on the Pelagian Platform, and gives an overview of the stratigraphic framework of the Maltese Islands.

2.1 Regional tectonic framework

2.1.1 Tectonic Evolution of the Mediterranean Region

The present-day appearance of the Mediterranean region results from the creation and consumption of the Paleotethys and Neotethys oceanic basins in Paleozoic to Mesozoic times, and the convergence of the African and Eurasian plates in Late Paleogene-Neogene to present times (Rosenbaum et al., 2002, Cavazza and Wezel, 2003, Di Bucci et al., 2010). This has caused some areas to undergo contraction and other areas extension. The region is dominated by a series of connected fold-and-thrust belts and associated foreland and back-arc basins, that have different geometries, timings and tectonic settings (Dart et al., 1993, Cavazza and Wezel, 2003).

The Mediterranean Sea opened to form its present geometry after a reduction in the northwards movement of the African plate, about 30 Ma (Jolivet and Faccenna, 2000). Extension started in the Western Mediterranean, which consists of several irregular sub-basins with large variations in crustal thickness. These basins developed as back-arc basins from west (the Valencia Trough, Alboran Sea and Algerian-Provençal Basin) to east (the Tyrrhenian Sea and Ligurian Sea) due to roll-back and eastward migration of the Apennine-Maghrebian subduction zone (Gueguen et al., 1997, Gueguen et al., 1998, Rosenbaum et al., 2002).

The Eastern Mediterranean differs from the basins in the Western Mediterranean. Whilst Mesozoic oceanic crust is not found in the Western Mediterranean, remnants of continental crust and/or oceanic crust from Neotethys are probably preserved under the sediments in the Eastern Mediterranean (Reuther and Eisbacher, 1985, Ben-Avraham et al., 2002, Rosenbaum et al., 2002). Neotethys, a subdivision of the Tethys Sea, formed between Laurasia and Gondwana in Permian-Triassic times as the supercontinent Pangea was breaking up.

2.1.2 The Pelagian Platform

The Maltese Islands are situated on the Pelagian Platform, which is a relatively stable plateau in the foreland of the Apennine-Maghrebian fold and thrust belt (Dart et al., 1993) (Fig. 2.1). The Pelagian Platform stretches from the Hyblean platform of southern Sicily to eastern Tunisia and Libya, and is bound by the Ionian Sea to the east and the Apennine-Maghrebian fold and

thrust belt to the northwest (Reuther and Eisbacher, 1985). In general, it is situated under water depths less than 400 m, but locally the depth can reach 1700 m in deep submarine canyons (Boccaletti et al., 1984, Reuther and Eisbacher, 1985, Micallef et al., 2013). The platform consists of a 6-7 km thick succession of Mesozoic-Cenozoic carbonates with intercalated volcanic rocks, and overlies continental basement of unknown age (Reuther and Eisbacher, 1985, Civile et al., 2010, Putz-Perrier and Sanderson, 2010). Based on morphology and structures in the Pelagian Platform, four different morphological zones can be characterized: (1) the Apennine-Maghrebian fold and thrust belt along the margin to the north and west of the Pelagian Platform; (2) the Pantelleria rift system to the west; (3) the Malta and Hyblean plateaus; and (4) the Malta Escarpment to the east (Fig. 2.1) (Micallef et al., 2013).

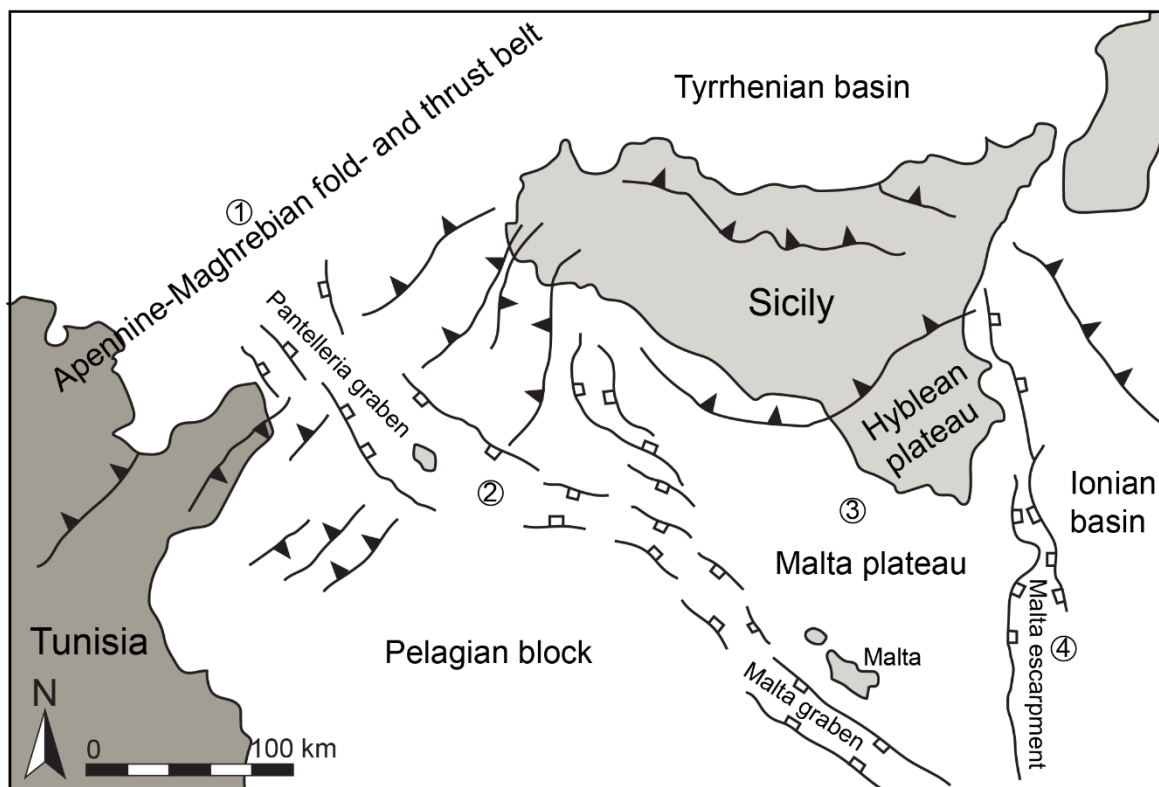


Figure 2.1. Overview of the Middle Mediterranean and the four structural domains that can be characterized: (1) the Apennine-Maghrebian fold and thrust belt along the margin to the north and west of the Pelagian Platform; (2) the Pantelleria rift system to the west; (3) the Malta and Hyblean plateaus; and (4) the Malta Escarpment to the east. From Granath and Casero (2004).

The Apennine-Maghrebian fold and thrust belt separates the Pelagian Platform from the Tyrrhenian Basin along the northern and western margin. This fold and thrust belt developed at the boundary between the European and African plate as the latter was subducted, from the latest Cretaceous to Early Pleistocene (Elter et al., 2003, Galea, 2007).

The Pantelleria Rift system, also known as the Sicily Channel Rift Zone, is SW of the Maltese Islands and oriented WNW-ESE, parallel to the south-western coast of Sicily (Reuther and Eisbacher, 1985, Micallef et al., 2013). The system is about 100 km wide and 600 km long (Dart et al., 1993), and forms three elongated troughs known as the Pantelleria, Linosa and Malta Troughs. These were created by N-S continental rifting in Neogene-Quaternary times, and was subsequently filled with Plio-Quaternary deposits (Reuther and Eisbacher, 1985, Dart et al., 1993, Civile et al., 2010). The driving force for the extension that created the Pantelleria Rift system has been interpreted in different ways (Galea 2007; Civile et al. 2010). Argnani (1990) suggests that the rifting could be a side-effect of the opening of the Tyrrhenian Sea, with extension caused by both slab roll-back and delamination due to slab-pull and mantle convection. More information is needed, however, to confirm this theory (Argnani, 1990). Illies (1981) proposes that the Pantelleria Rift system is an intraplate rift related to rotation of the controlling stress regime 10 Ma, while others (Reuther and Eisbacher, 1985, Ben-Avraham et al., 1987, Catalano et al., 2009) consider the troughs as pull-apart basins developed along a major dextral wrench zone called the Medina Wrench.

The Malta Plateau is on the north-eastern shoulder of the Pantelleria Rift system. Positive Bouguer anomalies over the area shows the extent of the plateau, which is an elevated area on the Pelagian Platform (Gardiner et al., 1995, Yellin-Dror et al., 1997). In the eastern direction, the Malta Plateau is abruptly separated from the deep Ionian Basin by the seismically active Malta Escarpment (Dart et al., 1993, Galea, 2007). North of the Malta Plateau, also bordered by the Malta Escarpment towards the east, is the Hyblean Plateau which comprise the southern part of Sicily (Fig. 2.1) (Grasso et al., 1986).

2.1.3 The Maltese Islands

The Maltese Islands are located within the Pelagian Platform on the north-eastern shoulder of the Pantelleria Rift, about 95 km south of Sicily and 290 km east of Tunisia (Fig. 2.2a), and comprise the main islands of Malta, Gozo, Comino, and a series of smaller islands (Micallef et al., 2013). The islands emerged from the Mediterranean during early Messinian times due to falling sea level and uplift of the Pelagian Platform (Bonson et al., 2007). The islands are one of few areas of the Pelagian Platform where a larger part of the Oligocene-Miocene succession appears above sea level, and provides the opportunity to study the Pantelleria Rift-related succession directly (Reuther and Eisbacher, 1985, Micallef et al., 2013).

The Maltese Islands are dominated by the ENE-WSW trending north Malta and north Gozo horst and graben structures, which dissect the Pantelleria rift at angles of 32° and 66° , respectively, and normal faulting is wide spread (Fig. 2.2b) (Dart et al., 1993). The largest fault on Malta, the Victoria Lines Fault, crosses the island from Fomm ir-Rih in the west to the Madaliena Tower in the east, and has a throw that varies between 100 m and 200 m. The Victoria Lines Fault separates two areas of different structural character, as the horst and graben structures are absent south of the fault (Pedley et al., 1976). The Maghlaq Fault on the southern coast of Malta is the only tectonic feature on the islands with a similar trend as the Pantelleria Rift system (Illies, 1981). Dart et al. (1993), interpret both fault trends as resulting from N-S extension.

Apart from faulting, large-scale gentle folding is an important structural feature of central and south Malta (Pedley et al., 1976).

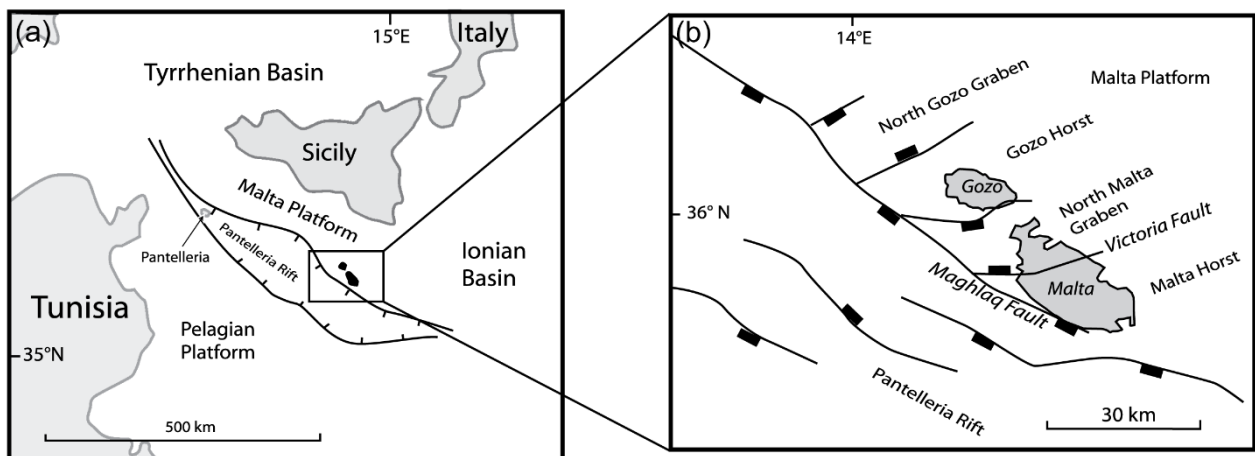


Figure 2.2. (a) Location of the Maltese archipelago, on the northern shoulder of the Pantelleria Rift. (b) The main structures on the Maltese archipelago, showing the Malta and Gozo horst and grabens that about the Pantelleria Rift. From Missenard et al. (2014).

2.2 Regional stratigraphic framework

The stratigraphy of the Maltese islands comprises a carbonate succession that can be subdivided into pre-, syn- or post-rift deposits with respect to the Pantelleria rifting event (Fig. 2.3) (Dart et al., 1993, Micallef et al., 2013).

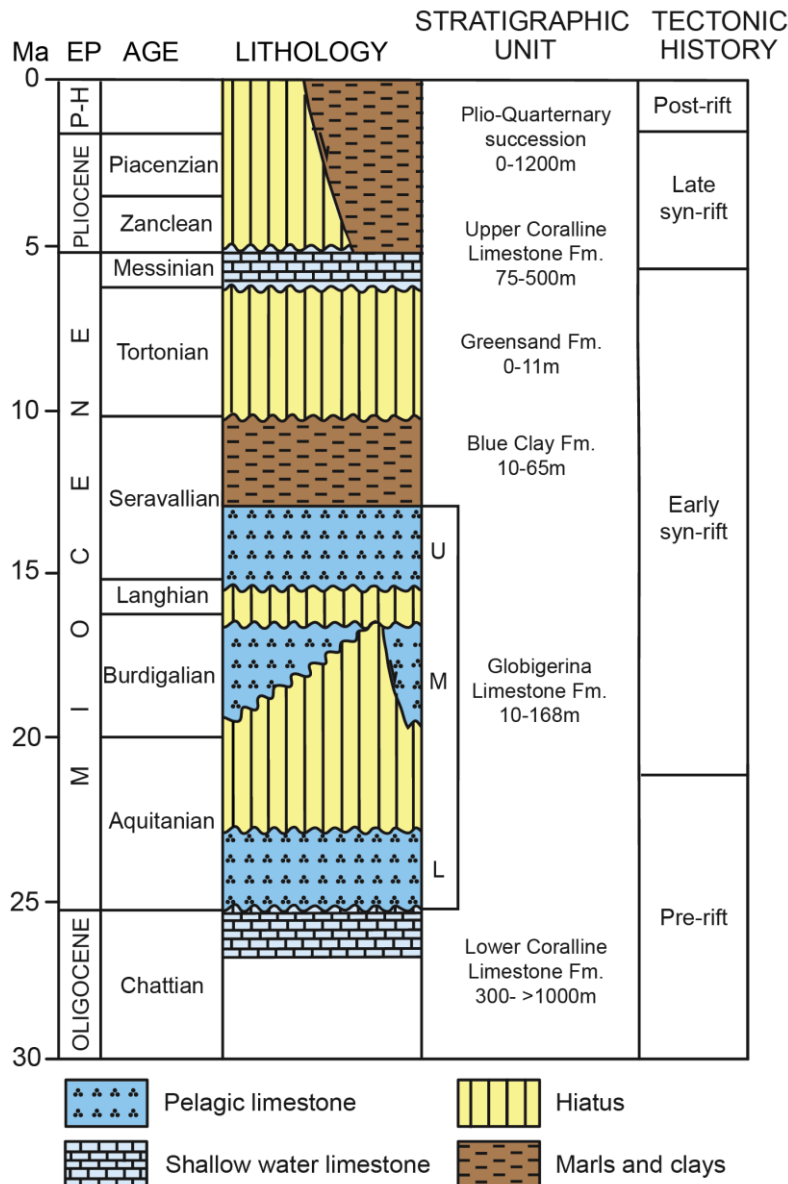


Figure 2.3. The stratigraphy of the Maltese islands comprises an Oligocene-Miocene carbonate succession, which can be subdivided into pre-, syn- or post-rift deposits with respect to the Pantelleria rifting event. After Bonson et al. (2007).

2.2.1 Pre-rift succession

The Lower Coralline Limestone Formation (LCL) and the Lower Globigerina Limestone Formation (LGL) constitutes the pre-rift phase on the Maltese archipelago. The uppermost 140 m of the LCL is the lowermost, and oldest part, of the carbonate succession exposed on the archipelago, where it forms the steep cliffs (Felix, 1973, Bonson et al., 2007). The formation is of Oligocene (Chattian) age, and is composed of massive beds of foraminifer-rich yellow biomicrites at the lowermost exposures, overlain by coarser, pale-grey coralline algal limestone. The lithology indicates that the depositional environment has evolved from a shallow, quiet environment to an open marine setting. Fossils are locally abundant in outcrops on the western

part of the island, where patch reefs are developed (Felix, 1973, Pedley et al., 1976, Bonson et al., 2007). A terminal hardground with an abundance of the echinoid *Scutella subrotunda* marks the top of the LCL formation (Pedley et al., 1976).

Overlying the LCL is the Lower Globigerina Limestone Member (LGLM), of Aquitanian age. It is part of the Globigerina Limestone Formation, which covers a large proportion of the Maltese Islands. LGLM consists of yellow, massive bedded, globigerinid biomicrites with a characteristic honeycomb weathering surface (Felix, 1973, Pedley et al., 1976). The top of the LGLM is marked by a phosphoritic conglomerate layer, which is cut by Neptunian dykes that mark the onset of the early syn-rift phase (Dart et al., 1993).

2.2.2 Syn-rift succession

The syn-rift phase is subdivided into an early and a late stage. The early syn-rift succession is comprised of the Middle (MGLM) and Upper Globigerina Limestone Members (UGLM), Blue Clay Formation (BCF), Greensand Formation (GF), and the lowermost part of the Upper Coralline Limestone Formation (UCL). The early syn-rift stage is characterized by minor fault-related thickness variations, neptunian dykes, evidence for minimal fault-related bathymetric relief, and preservation of unconformities and hiatuses in both uplifted and downthrown fault blocks (Dart et al., 1993). The late syn-rift phase includes the uppermost part of the UCL topped by a Plio-Quaternary succession of turbidites and hemi-pelagites. This phase is characterized by a strongly fault-controlled distribution of facies, areas of non-deposition, and major growth faults (Dart et al., 1993).

Early syn-rift

The MGLM commences just above the upper surface of the phosphoritic conglomerate in the LGLM. The unit is typically yellow to pale-grey, and consists of globigerinid biomicrites in the studied area south of Fomm ir-Rih bay, with a lateral transition to grainstone in the Hagar Qim-area further south (Rotevatn et al., 2016). As in the underlying formation, regional thickness variations occur but are hard to pinpoint due to post-Miocene erosion which has removed much of the strata (Pedley et al., 1976, Dart et al., 1993). The MGLM and UGLM are separated by a phosphatic conglomerate horizon (Dart et al., 1993). In the upper part of the UGLM, clay lenses may occur, and in the very top biomicrite grades into biomicritic marls and further into the clays of the BCF (Felix, 1973).

The BCF is relatively soft but is protected by the overlying UCL. The BCF consists of banded layers of blue clays of kaolinite and glauconite with small proportions of carbonate material, usually in the form of foraminifers. The BCF was deposited in a marine environment with water depths up to 150 m, shallowing to less than 100 m for the upper part of the Formation (Felix, 1973, Pedley et al., 1976). A 1 m thick zone characterized by an increase of glauconite, which gives a darker green color to the strata, indicates the transition from the BCF to the GF (Felix, 1973). The GF is rarely thicker than 1 m, and heavy bioturbation indicates deposition in a shallow marine environment (Pedley et al., 1976, Bonson et al., 2007).

The UCL can be subdivided into three depositional sequences, the first two of which are linked to the early syn-rift phase. The first sequence reflects the coralline algal biostrome facies, and shifts to coral and algal patch reefs in the second depositional sequence (Dart et al., 1993, Bonson et al., 2007). The dominance of algae indicates a shallow platform environment (Felix, 1973). These phases show changes in thickness and facies across faults, and therefore represent the main syn-faulting depositional packages (Dart et al., 1993).

Late syn-rift

The late syn-rift succession starts with the third depositional sequence of the UCL and ends within the Plio-Quaternary succession. The third sequence of the UCL consists of cross-bedded, oolitic, pelletoidal and bioclastic limestones, but is only locally preserved. A stromatolite horizon and a major decrease in fossils towards the top indicate an intertidal or supratidal zone (Pedley et al., 1976, Bonson et al., 2007).

Following the UCL is the Plio-Quaternary succession, which is the uppermost part of the late syn-rift phase. The deposits are discontinuous, and the sedimentology is therefore poorly known. Marls and carbonate mudstones were deposited in the Pantelleria rift when the central Mediterranean was re-flooded in Pliocene (Pedley et al., 1976, Dart et al., 1993).

2.2.3 Post-rift phase

Apparent low seismic activity and no significant movement in the faults indicate that today's deposition happens in the post-rift phase, but the data that supports this conclusion is sparse (Jongsma et al., 1985, Dart et al., 1993). Bottom sampling and shallow cores from the Pantelleria Rift show that hemi-pelagic, biogenic and turbiditic muds were deposited in late Quaternary (Dart et al., 1993). Alluvial fan deposits, caliche soil profiles and calcreted breccias stained by red iron are the youngest deposits onshore (Pedley et al., 1976).

3 THEORETICAL BACKGROUND

The purpose of this chapter is to provide a short overview of the terminology and theory related to the evolution of faults, structural control on fluid flow, and topology as a backdrop for this study. Evolution of faults and their corresponding damage zones is presented in Section 3.1, followed by a section about the existing theories about structural control on fluid flow in Section 3.2. Section 3.3 focuses on the theory around topology and topological data sampling.

3.1 Evolution of faults and damage zones

3.1.1 Single fault geometries

It is helpful to understand the geometries and development of single faults before considering fault linkage and fault evolution. Previous studies have documented a relationship between length and displacement within a fault surface (e.g. Watterson, 1986, Barnett et al., 1987, Marrett and Allmendinger, 1991). Such faults probably do not exist in nature, as faults are characteristically segmented, but an ideal, isolated normal fault can be presented as a plane, where the maximum displacement would be found close to its center and decrease to zero towards the edge or tip-line (Watterson, 1986, Cowie and Scholz, 1992a) (Fig. 3.1). The fault plane will have an elliptical shape, where the longest axis will be parallel to the length of the fault and the shortest axis will be parallel to the faults displacement direction, also referred to as its height (Kim and Sanderson, 2005).

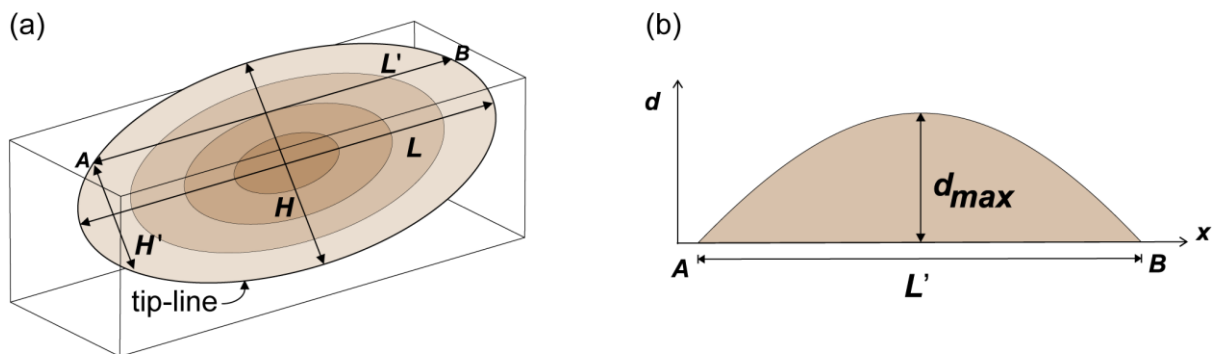


Figure 3.1. (a) Illustration of how displacement is distributed on an isolated fault plane with length L and height H . Darker color indicates higher displacement, meaning the displacement increase towards the center of the fault. (b) Profile A-B from where the fault breach the surface of the block showing how the displacement, d , varies along the fault. From Kim and Sanderson (2005).

The relationship between the maximum trace length of the fault (L) and the maximum displacement (D) has been addressed by several researchers (e.g. Rippon, 1985, Walsh and Watterson, 1988, Cowie and Scholz, 1992a, Cowie and Scholz, 1992c), and can be expressed by the function $D = cL^n$, where c is a constant that describe the properties of the rock, and n is

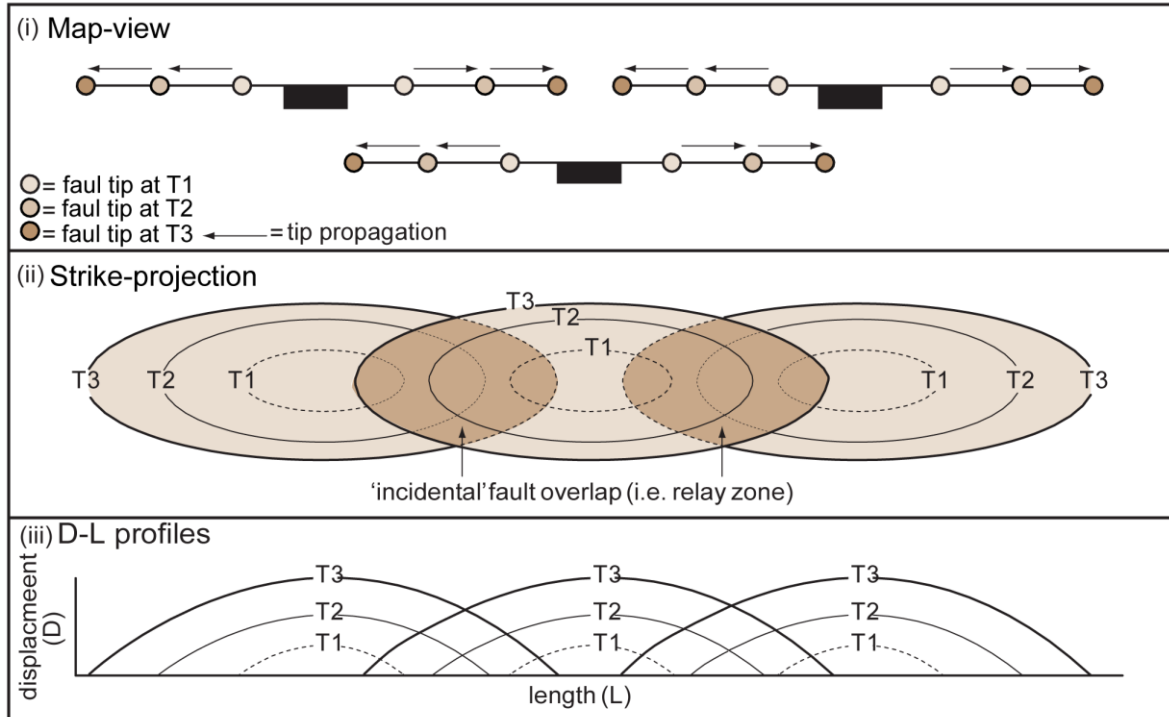
the linear relationship between length and displacement. n typically ranges from 0.5 to 2.0 in different data-sets, e.g. $n=0.5$ in Fossen and Hesthammer (1997), $n=1$ in Cowie and Scholz (1992c), $n=1.5$ in Gillespie (1992), and $n=2.0$ in Watterson (1986).

3.1.2 Fault linkage and growth

Normal fault growth has been presented through two different models by different authors through times. Walsh et al. (2003) refer to them as the “isolated fault model”, also called “fault growth by segment linkage”, which is the most widespread model (e.g., Walsh and Watterson, 1988, Cowie and Scholz, 1992b, Trudgill and Cartwright, 1994, Cartwright et al., 1995, Rykkelid and Fossen, 2002), and the “coherent fault model” (Childs et al., 1995, Walsh et al., 2002, Walsh et al., 2003). Figure 3.2 presents the evolution of normal faults through the isolated fault model (a) and the coherent fault model (b) illustrated by three time-steps (T1-T3) (Jackson et al.). Looking at the third and last step (T3 for both models) it is difficult to determine which of the two models best describes the fault evolution, since fault length, shape, and displacement are the same in both models.

The isolated fault model is based upon the theory that isolated faults grow by radial propagation as the length and displacement increase proportionally. The key premise for the isolated model is the sympathetic growth of length and displacement, but at continuous growth, the isolated faults will start to link and interact with adjacent faults (e.g. Walsh and Watterson, 1988, Trudgill and Cartwright, 1994). The coherent fault model is based upon the belief that the fault segments are spatially and mechanically related in the subsurface, but may appear as isolated faults on the surface. In other words, the faults may show limited interaction at one level, but may be linked at another level (e.g. Morley, 2002, Walsh et al., 2002, Giba et al., 2012). The coherent fault model assume that some faults reach their maximum length first, before accumulation of displacement (e.g. Walsh et al., 2003, Giba et al., 2012).

(a) The isolated fault model



(b) The coherent fault model

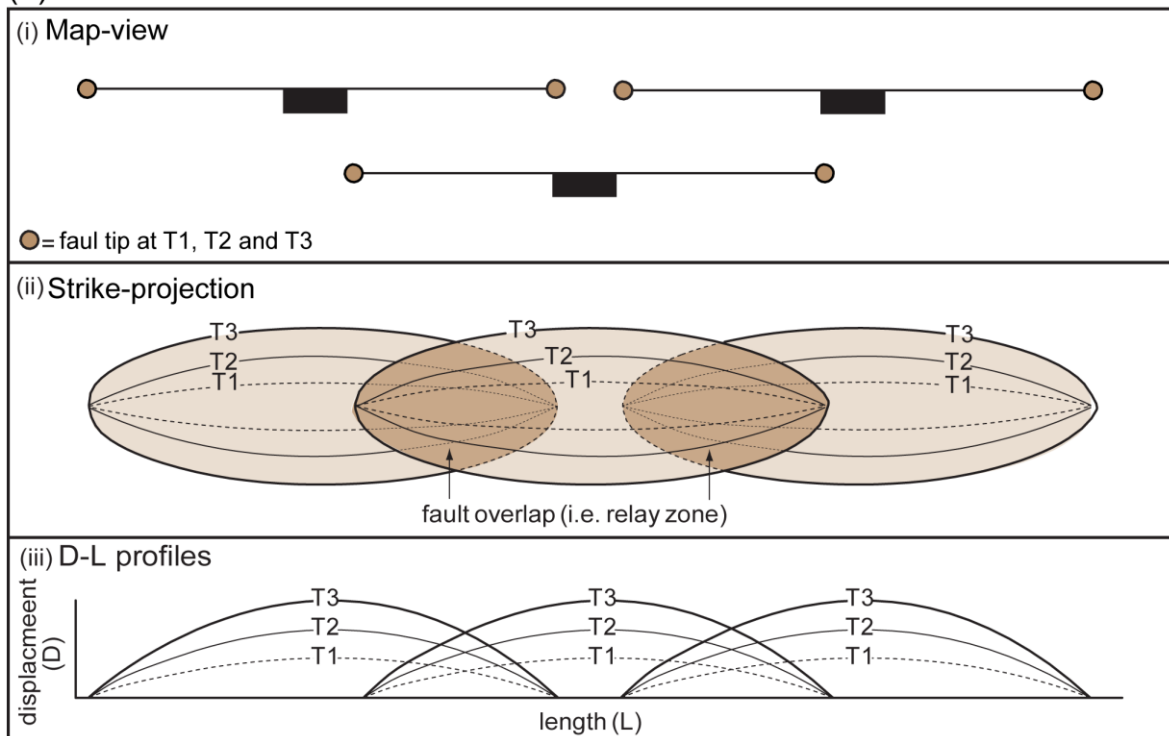


Figure 3.2. Illustration of the development of normal fault systems through two different models. (a) The “isolated fault model”. (b) The “coherent fault model”. Map view presented in (i), strike projection in (ii), and displacement-length (D-L) profiles in (iii), are meant to illustrate the most important features of the geometrical and evolutionary steps of each model. T1-T3 indicate time steps. From Jackson et al. ()

When single faults grow, they start interacting. Differentiation is made between two end member types called *soft-linked* and *hard-linked* (Walsh and Watterson, 1988, 1991). Soft-linked faults appear to be isolated at the scale of observation, but are overlapping and interacting through ductile strain of the rock volume between the faults, such as bed rotation in relay ramps (Walsh and Watterson, 1988). Hard-linked faults are faults that have a visible physical linkage, usually in the form of smaller faults (Walsh and Watterson, 1991, Peacock et al., 2016). The zone between normal fault segments in a soft-linked fault zone where displacement is transferred is referred to as a relay ramp. If fault segments link, creating a geometrically coupled (hard-linked) relay ramp it is termed a *breached relay* (Larsen, 1988, Peacock and Sanderson, 1994, Rotevatn et al., 2007).

Relay ramps can be divided into four stages for easier description, representing the evolution associated with deformation and displacement (Fig. 3.3) (sensu Peacock and Sanderson, 1994). Stage one is represented by isolated faults with no interaction to other faults or fractures. The second stage is characterized by soft-linked faults, as the faults propagate and start interacting through ductile strain of the rock body and create a relay ramp, but do not join. In the third stage fractures begin developing across the relay ramp and link the two segments together. The fourth, and last, stage is characterized by breaching of the relay by the fractures as they cut across the relay ramp, introducing the breached relay. (Peacock and Sanderson, 1994, Trudgill and Cartwright, 1994, Peacock et al., 2016).

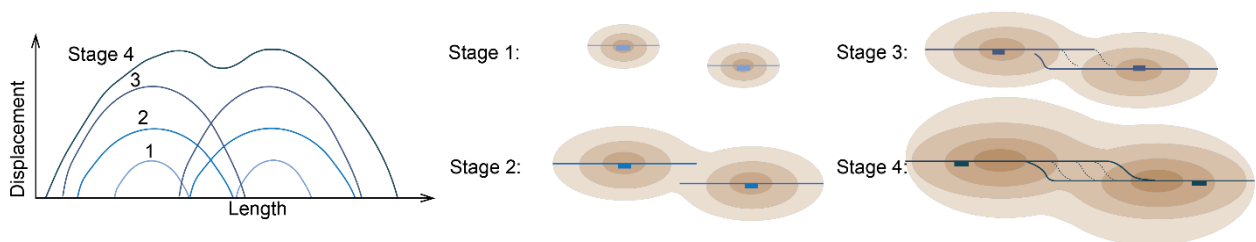


Figure 3.3. Illustration of the four evolutionary stages of a relay ramp. Stage 1) Isolated faults without interaction. Stage 2) Faults start interacting and displacement is transferred between them. Stage 3) Fractures start to link between the two segments. Stage 4) The relay is breached, producing one large fault instead of two smaller ones. After Peacock and Sanderson (1994).

3.1.3 Fault zone architecture

Faults expose their host rocks to deformation and modify certain volumes of the rock, called the *fault zone* (e.g. Childs et al., 1997, Bastesen et al., 2013). Fault zones are generally composed of a *fault core* and a *damage zone*, surrounded by intact, undeformed host rock, but all components are not necessarily present (Chester and Logan, 1987, Caine et al., 1996). According to Caine et al. (1996) the fault core is defined as the structural, lithological and

morphological part of the fault where most of the displacement is located, and its thickness can show great variations in both strike and dip direction. A core may contain single slip surfaces, fault gouge or breccia, fractures and deformation bands, shale smear, and lenses derived from the host or fault rock (Chester and Logan, 1987, Caine et al., 1996, Bonson et al., 2007, Bastesen and Braathen, 2010). The damage zone is the rock volume surrounding the core, associated with fault initiation, propagation and termination of the fault, and has a higher density of fractures than the protolith. Billi et al. (2003) describe the transition from damage zone to fault core in carbonate rocks, and show that the first part of the evolution is dominated by fracturing, which provides high permeability. The fault core develops in the most fractured part of the damage zone as rock fragments are broken down and reach a nearly isometric shape.

Damage occurs in the form of minor faults, joints, deformation bands, veins, and folds (e.g. Caine et al., 1996, Kim et al., 2004, Bastesen and Braathen, 2010, Choi et al., 2016). The structures may form prior to, during or after shear plane growth, due to stress increase at the fault tips (Cruikshank et al., 1991, Vermilye and Scholz, 1998), to accommodate displacement variations around faults (e.g. Vermilye and Scholz, 1998) and the strain in linkage zones of adjoining fault segments (Peacock and Sanderson, 1991, Childs et al., 1995).

Kim et al. (2004) propose a classification of damage zones around strike-slip faults based on their location within and around the fault zone, dividing them into *tip-*, *linking-* and *wall-* damage zones (Fig. 3.4). This classification can also be adopted for description of other types of faults. Tip damage zones occur around fault tips, and are also referred to as *process zones* (e.g. Cowie and Shipton, 1998). Damage in the footwall and hanging wall that is not controlled by linkage of faults comprise the wall damage zone, while the zone affected by fault linkage or fault overlap are referred to as the linking damage zone (Cowie and Shipton, 1998, Kim et al., 2004, Rotevatn and Bastesen, 2014).

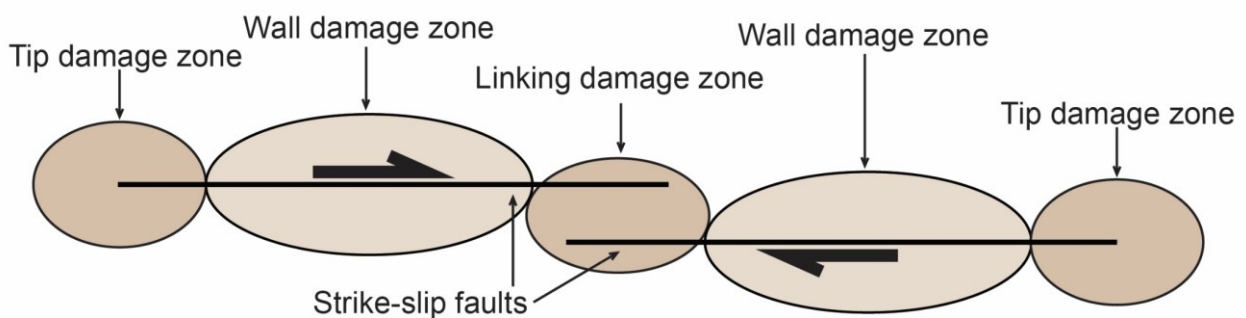


Figure 3.4. Schematic figure of location of the three main types of damage zones proposed by Kim et al. (2004), presented here around a strike-slip fault in map view. From Kim et al. (2004).

Several sub-types of fractures can occur within tip and linking damage zones. *Wing cracks* are secondary features that develop obliquely to the host fracture due to extension close to the tips of shear fractures, where they accommodate displacement variations, and may develop into pull-aparts with increasing displacement (Cruikshank et al., 1991, Wilkins et al., 2001, Crider and Peacock, 2004, Peacock et al., 2016). *Horsetail fractures*, referred to in same terms as *pinnate joints* by e.g. Kim et al. (2004), are wing cracks, but are more closely spaced and found in clusters with acute angles to the host fracture (Segall and Pollard, 1983, Wilkins et al., 2001).

3.2 Structural controls on fluid flow

Fluid flow in the subsurface are dependent on adequate porosity and permeability, where faults and fractures may play a significant role. Such structures can act as barriers preventing migration, as conduits which localize and promote fluid flow, or they can act as combined conduit-barrier systems which both promote and prohibit flow of fluids in the subsurface (Bouvier et al., 1989, Barton et al., 1995, Davatzes et al., 2005, Missenard et al., 2014).

Juxtaposition of impermeable layers and clay smear along the fault plane are some of the most well-known processes creating barriers for fluid flow, but also the presence of deformation bands can reduce the permeability and prohibit flow (e.g. Bouvier et al., 1989, Shipton et al., 2005, Jolley et al., 2007, Missenard et al., 2014). The fault plane itself can also act as a conduit, particularly along active faults due to dilation associated with the fault slip. Zones of higher structural complexity are in general revealed to be particularly prone to act as loci for focused fluid flow, enabling more flow through a more focused area. Such complex zones can be found in the areas around fault tips, fault bends, jogs, in active fault steps and fault intersection zones for instance (Gartrell et al., 2004). These zones provide higher connectivity through enhanced fracturing and dilation.

Stress perturbation may contribute to higher connectivity through optimal orientation of fractures in a network, which leads to an increase of the fracture aperture width (Martel, 1990, Davatzes and Aydin, 2003, Tamagawa and Pollard, 2008). Further, relay ramps between soft-linked faults can act as conduits across fault zones, either through folded, continuous beds or juxtaposition of high-permeable layers due to steep displacement gradient and folded layers (e.g. Rotevatn et al., 2009a, Rotevatn and Bastesen, 2014). Rotevatn and Bastesen (2014) propose that complex fault linkage zones may represent localized conduits for increased fluid flow both across and within fault zones in tight, brittle carbonate rocks. This differs from results in earlier studies focusing on porous sandstones, where low-permeable deformation bands were found to reduce the permeability in complex damage zones associated with fault linkage

(Fossen et al., 2005, Rotevatn et al., 2009b). Gartrell et al. (2004) present 3D-modeling of the Skua Oil field (in the Timor Sea) to investigate the role of fault intersections in hydrocarbon leakage. The study identifies fault intersections as the primary control on hydrocarbon leakage due to high dilation.

As mentioned above, fluid flow properties within a fault zone is not necessarily constant, but can vary spatially and temporally as a function of such factors as burial depth and fault throw (Fisher and Knipe, 1998, Mailloux et al., 1999, Bense et al., 2003, Kristensen et al., 2016). Mechanisms that can influence fault behavior include clay-smearing, drag of sand, and grain re-orientation (Bense and Person, 2006). Some faults may behave as conduits at an early stage during deformation, and change to barriers later in their evolutionary history due to mineralization (Ortega and Marrett, 2000, Verhaert et al., 2009). Alternatively, faults can initially be barriers, formed through deformation banding, and later get overprinted by joints or dilatant faults and hence change character to act as conduit (e.g. Davatzes and Aydin, 2003). Faults can influence fluid pressure dependent on their role as either conduit or barrier (Evans et al., 1997).

As geological structures control fluid flow, they also affect a variety of chemical processes that may occur as fluids percolate a rock. Such processes are also highly dependent on the composition of both the host rock and the fluid which pass through. Fluid migration can result in both dissolution and precipitation of minerals within the host rock, which may initiate cementation and create halos or fronts which are reduced or enriched in rare earth elements. Those processes are fundamental for this study, as they are serving as indicators of paleo-fluid flow. Cementation occurs due to oversaturation of the pore-fluids leading to precipitation of minerals (Flügel, 2010). The formation of redox fronts happens as a response to infiltration of oxidizing water, which carries rare earth elements to the front of the fluid flow (Akagawa et al., 2006). Both of these processes are primarily controlled by the pore-fluid composition, flow rate of the water passing through, and porosity and permeability of the host rock.

3.3 Topology

3.3.1 Origin and area of application

The term *fracture network* is herein used to describe a system of linked and interacting fractures with various lengths, orientations and apertures, formed as a result of strain accommodation (sensu Peacock et al., 2016). Their spatial distribution may vary through time, as fractures generally develop gradually. Fracture networks are important as they can act as fluid flow

pathways, and increase the amount of fluid flow in the subsurface (e.g. Davatzes et al., 2005, Zeeb et al., 2013).

Since fracture networks may act as conduits for fluid flow, a network characterization is essential in the process of quantifying fluid flow properties (Zimmerman and Main, 2003). Common approaches for characterizing fault and fracture networks have been based upon geometric properties of individual fractures, including lengths, apertures, orientations and intensities (e.g. Zeeb et al., 2013). However, these can be cumbersome methods that do not give any direct estimate of the network connectivity as they do not account for the relationship between the fractures. To meet the need for a better and more efficient method, Manzocchi (2002) introduced *topology* to fracture network characterization, a method which later was adapted and improved by Sanderson and Nixon (2015).

The topological approach considers the relationships between the geometrical elements in a fracture network and directly quantifies the network connectivity. As illustrated in Figure 3.5, two fracture networks can contain the same elements and hence have the same geometry, but still have very different topologies (Manzocchi, 2002, Sanderson and Nixon, 2015). Network A is arranged in a cross-joint network where the fractures interact, and would be more permeable than network B, where the fractures are randomly distributed as a stochastic network and shows poor connectivity. So, in contrast to geometry, which is defined by measurable unit dimensions such as lengths and orientations, topology is dimensionless and describes the relationships between elements or fractures in a network, directly quantifying the fracture connectivity (Morley and Nixon, 2016).

However, the estimates of connectivity from the surface of a fracture network may be considered as a minimum estimate. The topological analyses carried out through this project provide a two-dimensional portrayal of the network connectivity, but since the faults and fractures may also be linked in the subsurface, according to the coherent fault model (Walsh et al., 2002), the connectivity might actually be higher than it looks like at the surface.

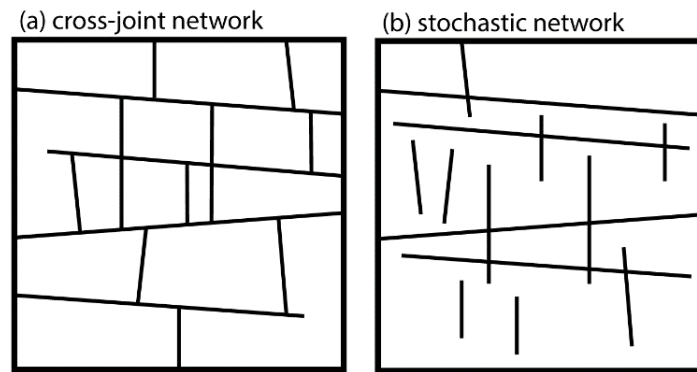


Figure 3.5. Two fracture networks with the same geometrical elements (same number, length, orientation), but different topology. (a) shows a highly connected cross-joint fracture system, while (b) shows the same elements in a stochastic manner. From Sanderson and Nixon (2015).

3.3.2 Nomenclature of topological elements

Topological characterization is based upon considering the elements of a fracture network as a combination of *nodes* and *branches* of different types (Sanderson and Nixon, 2015, Morley and Nixon, 2016). Nodes are end- or intersection points of fractures and are classified as either isolated nodes (I-nodes), abutting or splaying nodes (Y-nodes), or crossing nodes (X-nodes, Fig. 3.6). I-nodes represent isolated fault or fracture tips, Y-nodes represents points where fractures splay or abut against other fractures, and X-nodes are points where two fractures cross each other. Y- and X-nodes are also referred to as *connecting nodes* (Peacock et al., 2016). A *branch* is a segment of a line bounded by a node at each end, making the nodes define the classification of branches present in the network. Branches are classified as *isolated* (I-I), *partly connected* (I-C) or *fully connected* (C-C, Fig. 3.6). I-I branches are bounded by I-nodes at both ends, I-C branches are bounded by one I- and one connected node, and C-C branches are bounded at both ends by connecting nodes (Fig. 3.6) (Ortega and Marrett, 2000, Sanderson and Nixon, 2015). Branches that extend beyond the borders of the sample area are termed *unknown branches* (UKN) for this project, while unidentifiable nodes (e.g. nodes on the border of the sample area, or within unidentifiable zones) are termed *end nodes* (E-nodes).

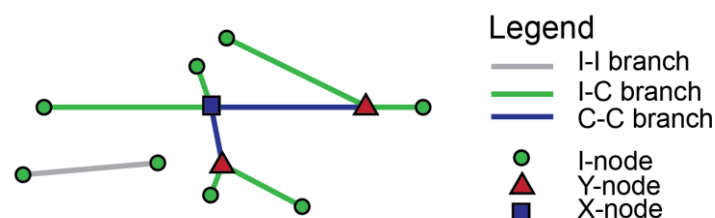


Figure 3.6. Sketch of simple network illustrating the different node and branch types used for topological network characterization. After Sanderson and Nixon (2015)

The proportions of the different node and branch types are what provide information about the connectivity of the fracture network, which is a crucial feature of fracture systems in terms of fluid flow (Ortega and Marrett, 2000). A network comprised solely of isolated nodes and branches is non-connective. Networks that are dominated by Y-nodes and I-C branches will have an intermediate connectivity, while a network containing a majority of X-nodes and C-C branches will be highly connective and thus increase the probability of fluid flow. An average number, between 0-2, of connections per branch can be derived from the number of different node types, providing a dimensionless measure of connectivity, which is one of the key advantages of topology. As a branch is constrained by one node in each end, and cannot possess more than two nodes, the highest number possible is two. The higher the number, the higher network connectivity (Sanderson and Nixon, 2015). This number is derived from a simple formula based on the fact that a Y-node indicates connection to three branches and an X-node indicates connection to four branches, while I-nodes are isolated and hence do not indicate any connections. The number of connections per branch (C_B) cannot exceed two and are found through the equation:

$$C_B = (3N_Y + 4N_X) / N_B \quad (1)$$

Where N_Y = number of Y-nodes, N_X = number of X-nodes, and N_B = number of branches (Sanderson and Nixon, 2015).

Data retrieved from the topological analysis of a fracture network can be portrayed and presented in a series of ways, including ternary diagrams portraying the degree of connectivity, density maps showing branch intensity, and density maps of connecting node frequency. These are powerful tools that provide good visualizations of the connective properties of fault and fracture networks. More information about the application of topology will be given in the mMethodology-chapter under Section 4.2.

4 METHODOLOGY

The purpose of this chapter is to provide an overview of the methods applied during fieldwork and following analysis. The project is based on data collected in Malta through two field seasons, three weeks in October 2015 and three weeks in April 2016. Data was obtained from different localities which were chosen based upon good access and exposure, and characteristic features in form of mounds or redox fronts in combination with faults and/or fractures. To address the study aims stated in Chapter 1, the specific localities were chosen with the purpose of investigating the relationship between evidences for paleo-fluid flow vs. the location of structural complexities of the studied fault and fracture networks.

4.1 Field data

As outlined in Section 1.3.2, mound-type and redox-type localities were used in this study. Field data were collected from nine localities, six mound-type localities and three redox-front type localities. At all localities the data collection included collecting;

- i) General information like coordinates and dimensions of studied area, orientation of faults and fractures etc.
- ii) Description of locality
- iii) Images
- iv) Topological data
- v) Rock samples

For the mound-type localities, topographic profiles were gathered in addition to the listed above, with the purpose of documenting topographic changes due to the mounds. Length-displacement profiles and width of the redox fronts was measured for the redox-type localities. In addition to the data from the localities, a stratigraphic log was created. The data and methods used for collecting them are further described in the following sub-chapters.

4.1.1 Sedimentological logging

In order to describe the local host stratigraphy in the study area, a stratigraphic log was collected by the northernmost localities, and information from laterally equivalent beds further south was extrapolated and included in order to ensure that the log was representative for the entire study area. The log is based on observations in the field, with some guidance from previous work by Dart et al. (1993) and Michie et al. (2014). The lithofacies of each unit were described following the Dunham (1962) classification scheme for carbonate rocks. All the studied

outcrops are situated within the same stratigraphic level; therefore, one log was considered representative.

4.1.2 Topography profiles

For all the mound-type localities, the mounds form localized topographic highs. Therefore, to constrain the location of the mounds along the studied fracture networks, topography profiles were acquired along the fracture network. The placement of the profile was chosen in order to include as much of the variations as possible. A reference point in form of a fixed datum line was stretched out along the network, approximately 20-30 cm above ground, and the distance from the line to the ground was measured with a yardstick (Fig. 4.1). The measuring was done in a consistent and systematic manner to secure accurate representations of the topography.

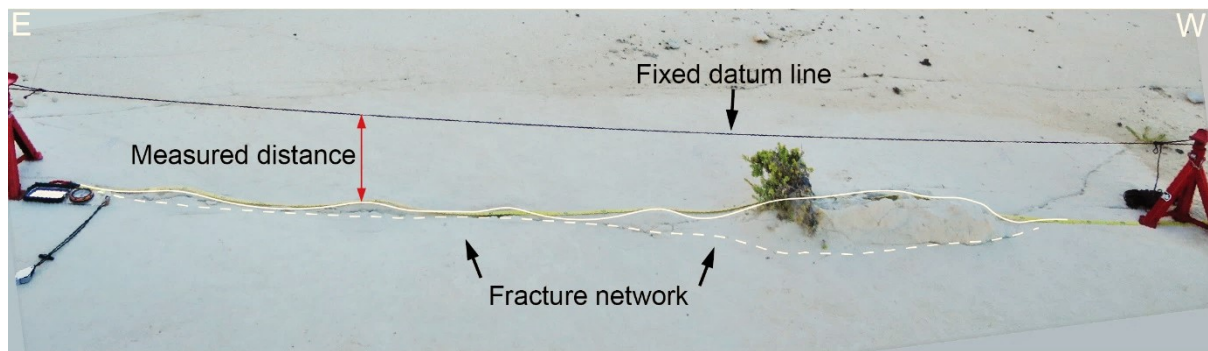


Figure 4.1. Field photograph showing an example of how the topography profiles were obtained, using a fixed line above the fracture network as a reference. The solid line marks the highest point along the network (the mounds standing out), whereas the dotted line represents the topographic “base” of the fracture network. The red arrow shows the distance measured between the fixed line and the network.

4.1.3 Topology: preparatory data sampling in the field

As mentioned in Chapter 3, topology quantifies connectivity by describing the relationship between elements in a fracture network, based on the amount of different node and branch types. To make it easier to distinguish branches in the fracture networks from the homogenous background, the whole fracture network was marked with a pencil, after which it was carefully documented through a series of close-up photographs. An example is presented in Figure 4.2a.

4.2 Topological characterization of the studied fracture networks: image based data collection and analysis using ArcGIS

Topological analysis of the fracture network for each location was carried out in the software ArcGIS based on the images acquired in the field. ArcGIS is a geographic information system, initially used for creating maps and work with geographical information, but the software’s area of application is broad and it can be a useful tool for solving different problems (Johnston et al., 2001). The full workflow for ArcGIS in this project is shown in appendix II.

The field photos of the fracture networks from the localities were stitched together to create a joint photomosaic from each locality. The imagery was then imported to ArcGIS, where all fractures were digitized. Feature classes for nodes and branches were created in the software, and the nodes and branches of the network were distinguished as the different feature classes. A feature class is a group of nodes or branches with the same characteristics; as an example, I-nodes are created as one feature class, Y-nodes as another, C-C branches as a third, and so on. An example of a plotted network can be seen in Figure 4.2b where branches are presented as polylines and nodes are marked as points. A map of the fracture systems with nodes and branches, like the one in Figure 4.2b, was made for each locality based upon the photomosaics.

The fracture networks digitized in ArcGIS are used to generate plots of the following topological parameters: i) density maps of the branch intensity, which presents the total branch length per square meter (m/m^2), and ii) density maps of the connecting node frequency, presenting the number of connecting nodes per square meter (N_c/m^2). In general, areas with high branch intensity would be characterized by several small branches, while areas with low branch intensity would have few but generally much longer branches. High connecting node density means that the studied area contains a high number of connecting nodes (Y- and X-nodes) per square meter. High connecting node density also signifies areas with short but numerous branches, as connecting nodes marks intersection points between branches.

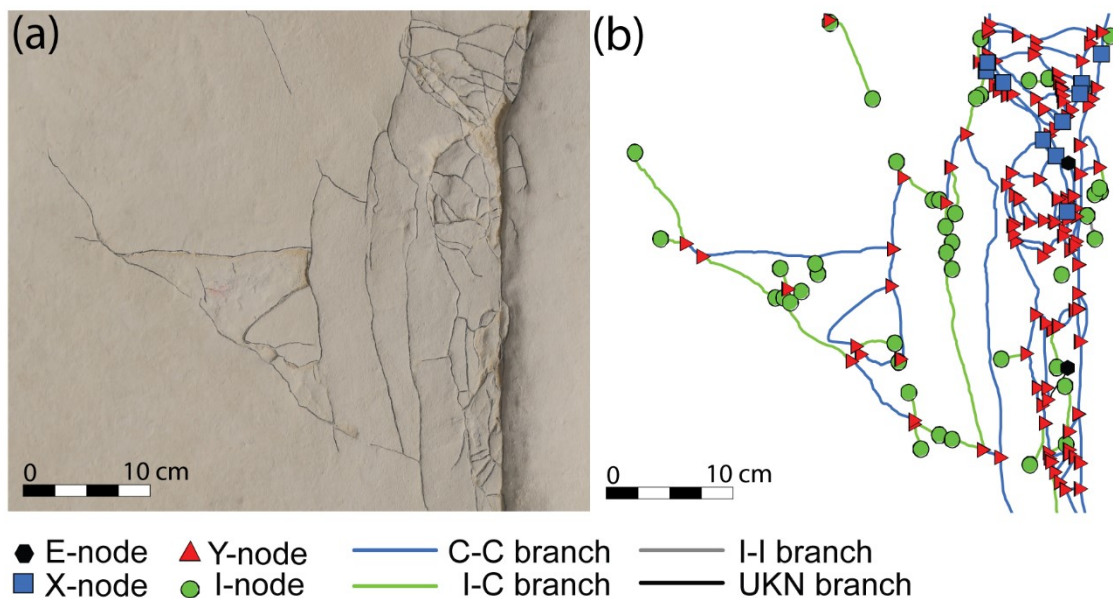


Figure 4.2. Cut-out section from a mound locality. (a) The fracture network is drawn on the ground with a pencil, for easier recognition of nodes and branches during following digitalizing and topological analysis. Several pictures like this were taken to cover a locality, and then stitched together to create a joint photomosaic. (b) Example of how the fracture network looks like after digitalization and topological analysis.

4.3 Microscopic analysis

Collected rock samples were sent to the *Independent Petrographic Services Ltd* in Aberdeen, UK, for preparation of thin sections. The samples were polished to a thickness of 30 microns and impregnated with a clear, blue epoxy with the purpose of easier pore space recognition.

4.3.1 Regular Light Microscopy

A *Nikon labophot 2-pol-* and a *Nikon Eclipse E400 POL* polarizing microscope were used for the thin section analysis. The *Nikon Eclipse E400 POL* was used together with a *Nikon digital sight DS-Fi2* camera and the imaging software *NIS Elements F* to acquire photos at different magnifications (4X and 10X) for 2D porosity estimations in the image-processing software *ImageJ*.

4.3.2 Scanning Electron Microscopy

A scanning electron microscope (SEM) was used to increase the resolution of the porosity measurements, and to do investigations at a much higher magnification than possible by the use of a regular light microscope. Instead of light, the SEM uses a beam of high-energy electrons to form an image of the thin section. This gives a larger depth of field, and the opportunity to study the samples at nanometer scale, looking at microstructure morphology and chemical composition characterizations (Zhou et al., 2007).

Before the samples were studied in the SEM they were covered with a thin layer of carbon to conduct electricity, which prevent accumulation of charge when the electrons hit the samples.

Electrons in the SEM hold a high amount of kinetic energy which scatters into a variety of signals when the electrons hit the solid sample and decelerates. Amongst these are heat, visible light, photons (x-rays), backscattered electrons (BSE), diffracted backscattered electrons (EBSD), and secondary electrons. Secondary electrons can show morphology and topography on samples, while BSE can illustrate contrasts in composition in multiphase samples (Egerton, 2006).

All SEMs include several components, where the most vital ones are the electron source (the “electron gun”), electron lenses, electron beam scanning coils, the sample chamber, and SEM detectors (Fig 4.3). The electron source produce electrons by thermionic heating, and then accelerate the electrons to an energy level of 0.1-30 keV (Zhou et al., 2007), compressing them into a narrow beam. Several electron lenses (i.e. condenser lenses and objective lenses) are used to focus the beam as it moves from the electron source towards the sample (Zhou et al., 2007,

Instruments, 2016). The electron beam requires a high-vacuum environment, which disables the electrons to scatter and simultaneously lower the chance of damaging the electron gun (Zhou et al., 2007). When the beam is focused, the scanning coil divert it in a way that makes it possible to scan the sample surface in a raster fashion along the x- and y-axis (Instruments, 2016). This takes place in the sample chamber, where the samples are placed after being covered with carbon. The detector is chosen based on the purpose of the research. The HDAsB detector, which records BSE, was mainly used for this project to get high quality images.

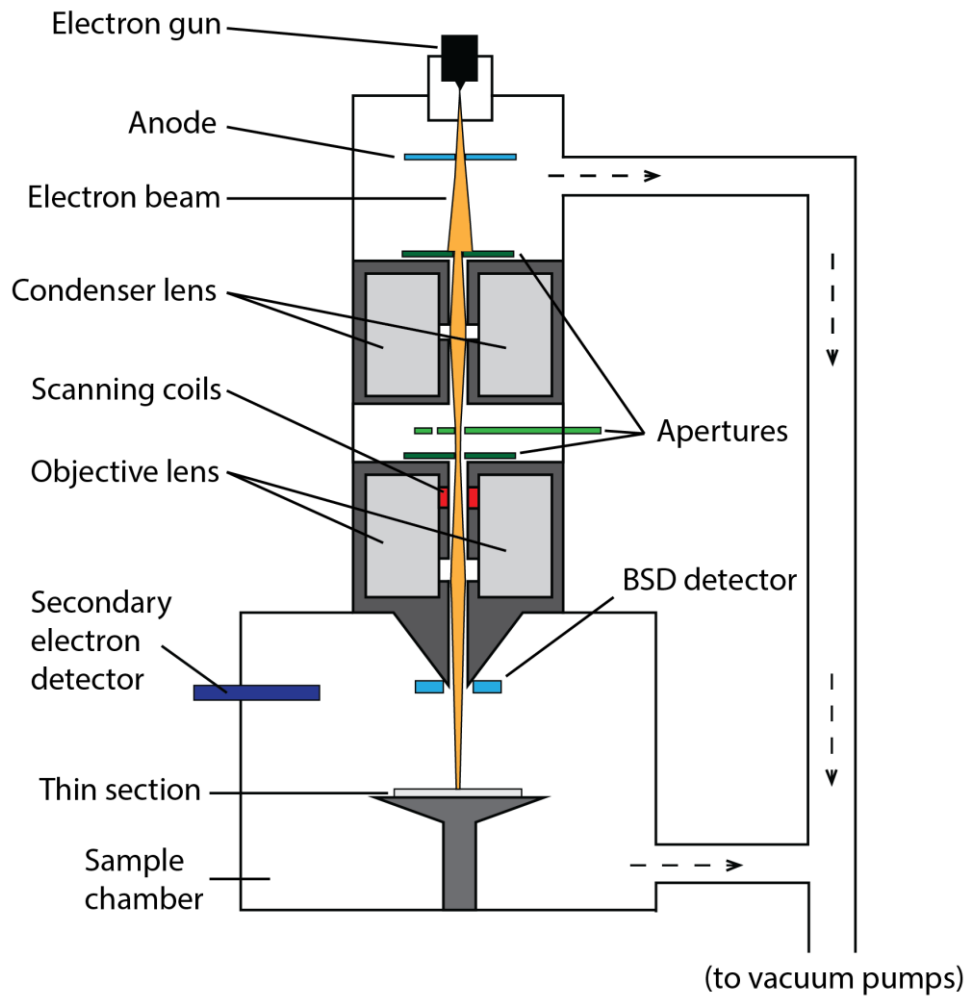


Figure 4.3. Simplified sketch of a Scanning Electron Microscope, showing the main components. It comprises an electron gun at the top, and several lenses and apertures to control the electron beam on its way to the sample chamber. Vacuum pumps establish vacuum in the chambers. Modified after Northern Arizona University (2015).

4.4 Image analysis for porosity determination

Images from the light microscope and SEM were further processed using the image processing software *Image J*. The photomicrographs from the light microscope provided information only on the 2D macro porosity, whereas the BSE images also provided information on the 2D micro porosity. Thin section images were imported in *Image J*, and porosity was further acquired from a binary version of the images.

4.4.1 Image analysis of photomicrographs

The images are first acquired, before the scale is set. The microphotographs were acquired in color, with the pore space shown in clear blue due to the epoxy. The method is therefore based upon converting the RGB images (Red, Green, Blue) to HSB (Hue, Saturation, Brightness) images. *Hue* describes the attribute of pure color, and therefore distinguishes between colors, *saturation* shows the purity or shade of the color (i.e. how much white is added to the pure color), while *brightness* shows the overall brightness of the color (Ferreira and Rasband, 2012). By setting the threshold color to red, the *hue* of the blue epoxy can easily be selected from the rest of the color spectrum in the image, before the threshold image is converted to black and white. The image type is set to 8-bit to acquire a binary image and enable the “particle” analysis. Automated measuring gives the total pore space area and individual pore area size. Schematic flow chart for the ImageJ process can be seen from Figure 4.4. Full workflow is presented in Appendix II.

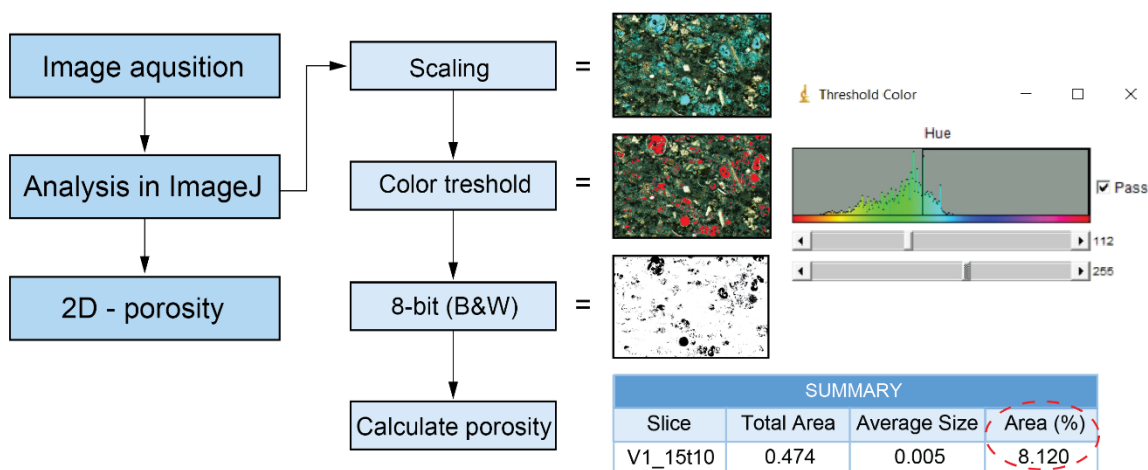


Figure 4.4. Schematic flowchart illustrating the steps performed in the digital image analysis of the microphotographs in ImageJ for porosity measurements. The dashed circle is pointing out the estimated porosity value. The process can roughly be divided into four steps. Scaling: image is imported to ImageJ where the scale is set. Color threshold: image is converted to HSB in which pore space is selected based on its distinct blue color. 8-bit B&W: image type is set to 8-bit to acquire binary image and enable particle analysis. Calculate porosity: pore space is automatically calculated from the black areas.

4.4.2 Image analysis of BSE-SEM images

The process for the BSE-SEM images in *ImageJ* is very similar to the one for the microphotographs. Since these images are in greyscale, the threshold is set so that the black areas represent the pore space, with the operator manually adjusting the threshold between the shades of gray and acquiring a binary image. Then the particles are analyzed to acquire the pore area through pixel counting. Schematic flow chart for the ImageJ process can be seen from Figure 4.5. Full workflow is presented in Appendix III.

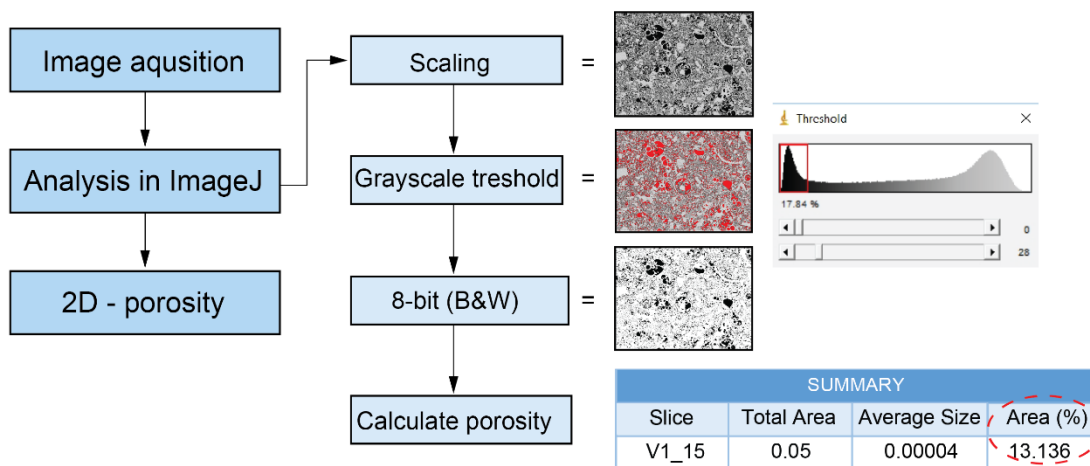


Figure 4.5. Schematic flowchart illustrating the steps performed in the digital image analysis of the BSE-SEM images in ImageJ for porosity measurements. The dashed circle is pointing out the estimated porosity value. The process can roughly be divided into four steps. Scaling: image is imported to ImageJ where the scale is set. Grayscale threshold: the black areas which represents pores pace are chosen. 8-bit B&W: image type is set to 8-bit to acquire binary image and enable particle analysis. Calculate porosity: pore space is automatically calculated from the black areas.

4.4.3 Uncertainties related to the image-based porosity analysis

Performing 2D-porosity estimations come with some limitations and possible sources of error. The thin sections provide a two-dimensional view of the pore space, which in reality is three-dimensional. The estimations of the porosity in the thin sections will be based on the grain boundaries that are visible at the top of the thin section. Grains, and adjoining pore space, smaller than the thickness of the thin section, may therefore be excluded. This problem is illustrated in Figure 4.6, showing a top-view and a cross sectional profile through a thin section.

Other pitfalls can be porosity variations throughout the rock and within the thin section. The porosity can vary significantly within a small area, and the porosity measurements will therefore depend on the heterogeneity of the rock. In this project the sampled rock appears homogenous when looking at hand specimens, but porosity variations were observed when examining the

thin sections through the microscope. To minimize this potential source of error, several photos were obtained of each thin section to capture the overall variation for each sample.

To ensure the quality of the porosity estimations, the populations of data can be arranged in a probability plot to check if they conform to normal distribution. If the data shows normal distribution it can be applied to parametric methods such as the Student's t-test and Snedecor F-test. A Student's t-test is used to check if the average values of two data sets are significantly different. The level of significance is described by α , and the lower the value, the more significant is the test. Snedecor F-test can state if populations of data have significantly different variances. Both the Student's t-test and Snedecor F-test was carried out on the data obtained from the porosity analysis in this project.

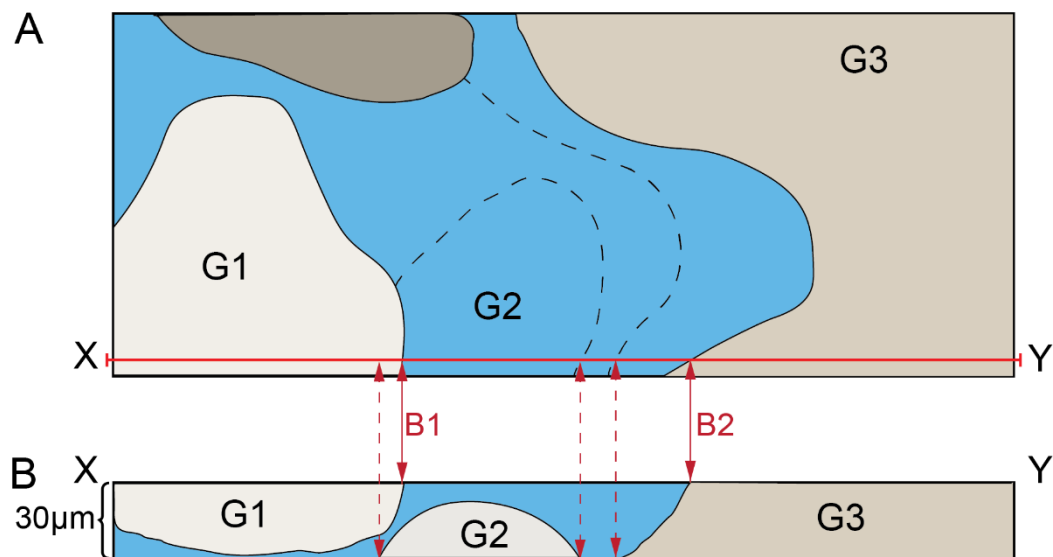


Figure 4.6. Schematic sketch of top- and cross sectional view of thin section. G is short for grain, B is short for boundary, and the blue color imitates the pore space. A) Top view of an imagined thin section, showing grains G1 and G3, pore space, and grain boundaries. The dashed lines are indicating grain boundaries located deeper in the thin section, illustrated in figure B. These will not be visible in the top view of the thin section. B) Cross sectional profile from the thin section, where all three grains, and the pore space in between, can be observed. After Thorsheim (2015).

5 RESULTS

In this chapter the field observations as well as the collection and analysis of quantitative structural data from each locality will be presented. Furthermore, micro-structural, petrographic and porosity analysis based on investigation of thin sections are presented. An overview of the structure and stratigraphy of the study area is first introduced, after which the results for each locality will be presented. All localities, except one, are located in the same area south of Ras ir Raheb outside the small town of Il Bahrija (Fig. 5.1). One locality is found on the northern coast of Gozo, west of the town called Marsalforn (Fig. 5.1); the local structure and stratigraphy in this location is briefly introduced for context in Section 5.6.1.

5.1 Structure and stratigraphy of the study area at Ras ir Raheb

5.1.1 Structural framework

The study area is located on the western coast of Malta, in Ras ir Raheb, at the cliffs outside Il-Bahrija (Figs. 1.1 and 5.1). Ras ir Raheb is situated just south of the Victoria Lines Fault, and the cliffs are affected by several ENE- and E-trending normal faults with displacements that varies between 3 cm and 25 m (Michie et al., 2014). The faults are exposed in a cross-sectional view through the cliffs, and in map view at wave-cut platforms, providing good conditions for studying.

Some faults in the area have been carefully documented by Michie et al. (2014), but complimentary mapping was done for this project to include more faults. A total of twenty-eight faults were documented with location, orientation and displacement during the fieldwork (Fig.5.1b). The smallest displacement measured on a fault was 3 cm, while the largest displacement measured was 5.2 m. Fault orientations are shown stereographically in Figure 5.1b, showing that the main trend is roughly E-W, but ranging from WNW- to WSW-trending. The majority of the faults are dipping towards the north, some dip towards the south, and a few faults change polarity along the fault plane.

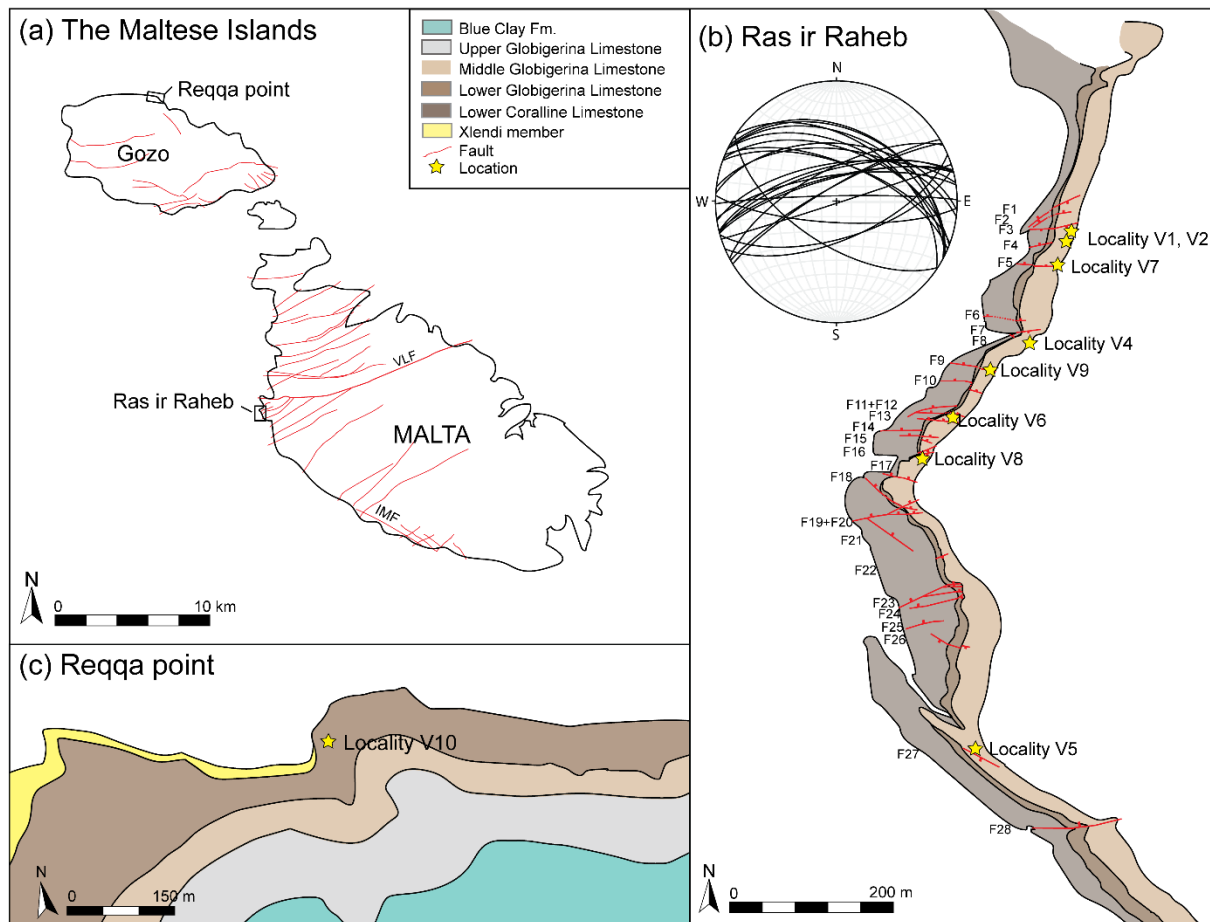


Figure 5.1. (a) Overview sketch map the Maltese Islands, showing the location of the field areas (after Pedley et al. 1976, Michie et al. 2014 and Missenard et al. 2014). (b) Field area on the west coast of Malta, just south of Ras ir Raheb. The localities are named V1, V2, and V4-V9, and marked by yellow stars. Faults documented during fieldwork, labeled F1-F28, are marked with red and presented in a stereonet showing strike and dip measurements (after Michie et al. 2014). (c) Field area on the north coast of Gozo, Reqqa point, west of Marsalforn, where locality V10 is situated (after Kim et al. 2003).

5.1.2 Stratigraphic framework

The localities at Ras ir Raheb chosen for this study are all situated within the MGLM, which forms part of the syn-rift succession. Logging of the formation has been carried out earlier, e.g. Pedley et al. 1976, Michie et al. 2014, and through Heidi Synnøve S. Fossmark and Elin Thorsheims' master thesis, Fossmark (2015) and Thorsheim (2015), but due to great local stratigraphic variation a new log was made for this specific study area (Fig. 5.2). For an easier overview the MGLM is divided into sub-units within the study area, which are given a closer description below. Description of the LGLM studied at Gozo are presented in Section 5.6.

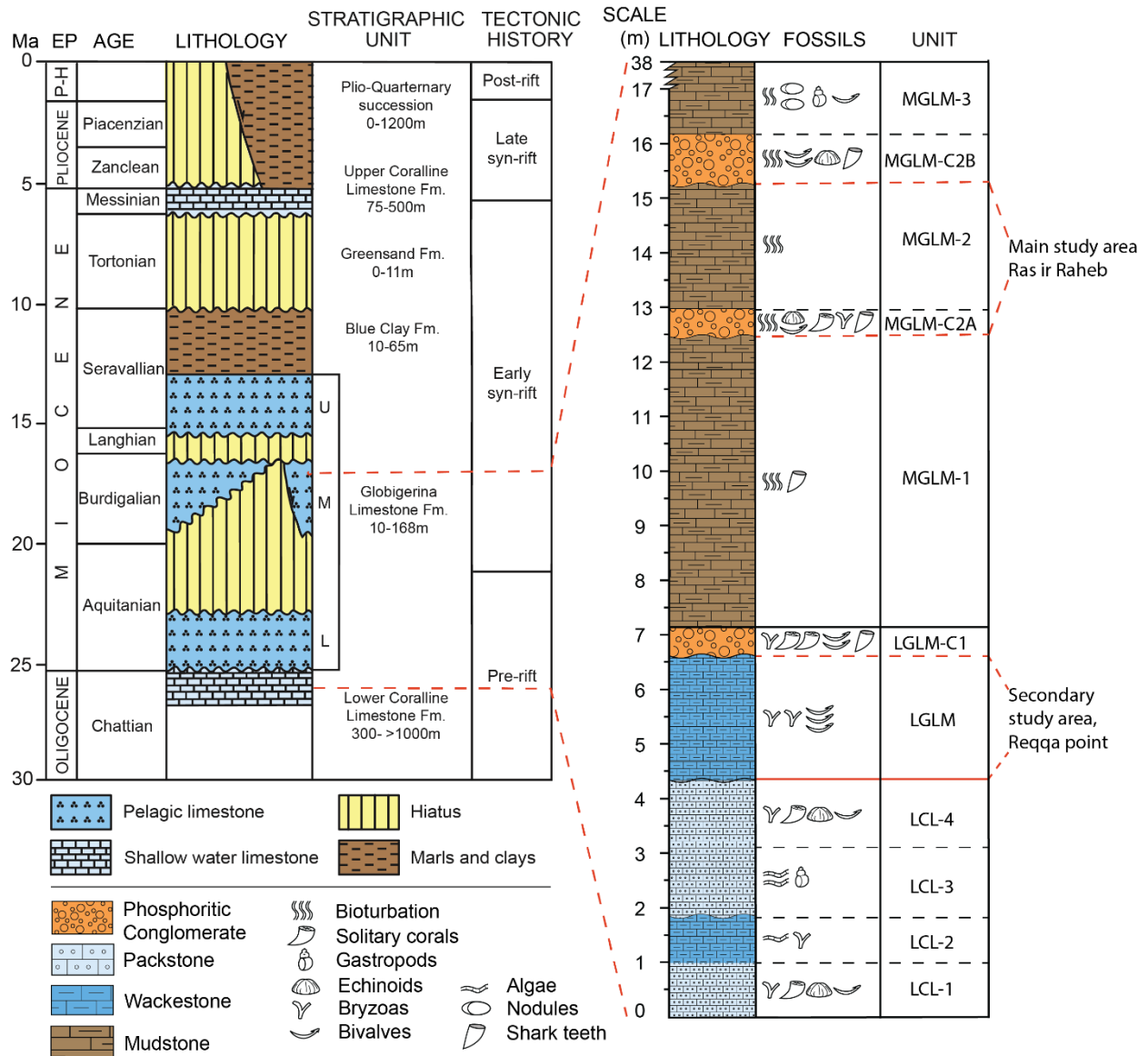


Figure 5.2. Generalized stratigraphy on the Maltese Islands shown on the left; modified from Dart et al. (1993). Stratigraphy of the studied succession in the field area shown to the right. The stratigraphy was logged in one area at Ras ir Raheb, but shows the interval of which the locality at Reqqa point is situated.

Unit LGLM-C1, MGLM-C2A and MGLM-C2B

Three distinct layers of phosphoritic conglomerate are found in the stratigraphic succession in the cliffs of Ras ir Raheb. The layers are easily recognizable and has an important role as marker beds in the stratigraphy. One of the layers is situated in the LGLM, and is named LGLM-C1, while the other two conglomerates are found within the MGLM and are named MGLM-C2A and MGLM-C2B (Fig. 5.3a). The thicknesses of the conglomerate units vary laterally, and are generally less than one meter thick. The phosphoritic conglomerate layers are brown, and an abundance of solitary corals, shark teeth and bivalves are found in the matrix along with some bryozoas. Echinoids was observed in the MGLM-C2 and MGLM-C3. The clasts are mainly

pebble sized (1-2 cm), with occasional occurrence of clasts that are cobble sized. The conglomerate is mainly grain supported, with a matrix of micritic limestone. Phosphate-rich solutions have cemented the conglomerate after deposition, making it a resistant horizon (Pedley et al., 1976).

The lowermost of these phosphoritic conglomerate layers, the LGLM-C1, marks the transition from the LGLM to the MGLM, and represents the top of the LGLM. MGLM-C2A and MGLM-C2B are situated within the MGLM, and contains pebble filled burrows in addition to the fossils mentioned above.

Unit MGLM-1, MGLM-2, MGLM-3

The three units MGLM-1, MGLM-2, and MGLM-3 constitutes the majority of the MGLM. These units are all comprised of homogenous carbonate mud (Fig.5.3b and c), and show signs of bioturbation. According to Dunham's classification scheme (1962) the MGLM can be classified as a mudstone.

Shark teeth were observed in the lowermost unit (MGLM-1), while nothing but traces of bioturbation could be found in the MGLM-2. More changes occur when moving into the MGLM-3 which contains an abundance of nodules and fossils of gastropods and bivalves in contrast to the other MGLM units. The MGLM-3 is approximately 22 m thick, and thus thicker than MGLM-1 and MGLM-2 which are 5.3 m and 2.3 m, respectively. Capping the MGLM-3 is another phosphoritic conglomerate layer, marking the transition to the Upper Globigerina Limestone Member.

The MGLM-2 is the area of interest in this project, as this is where the localities south of Ras ir Raheb is found stratigraphically. The following chapter will provide a detailed characterization of the MGLM-2, which constitute the host rock for the localities.

5.2 Host rock characterization

Due to local variations in the lithology, a host rock sample was collected for each of the mound localities. All samples were collected in the MGLM-2 unit, 1-2 meters from its' corresponding mound locality. The following characterization is based upon field observations and thin section analysis of all the host rock samples from the localities, aiming to provide a general description of the host rock in the study area.

The rock is mud-supported and contains less than 10% grains. The grains present are generally smaller than 250 μm , and according to Dunham's classification scheme (1962) the rock can be

classified as a mudstone. The carbonate mud predominantly consists of skeletal fragments from bivalves, echinoderms, and most abundantly planktonic foraminifera (Fig. 5.4). The foraminifers, being mostly *Globigerina*, are generally well-preserved and most of them still intact. The grain size of the foraminifers is generally in the range of 10 - 20 μm , but whole foraminifer shells with sizes up to 250 μm occur. Calcite cement is observed on some of the foraminifer shells (Fig. 5.5a), interpreted to be dogtooth cement, probably as a result of meteoric diagenesis. The dogtooth cement grows at a normal angle to its substrate, and appear as elongated crystals with blunted terminations in variable sized. The cement is most commonly present within the chamber of the foraminifers, but also occurs on the outside. The cement growth does not seem to favor any type of foraminifers or other features, but appear at various degrees throughout the samples. Some quartz grains with an average size of 120 μm are also found within the samples.

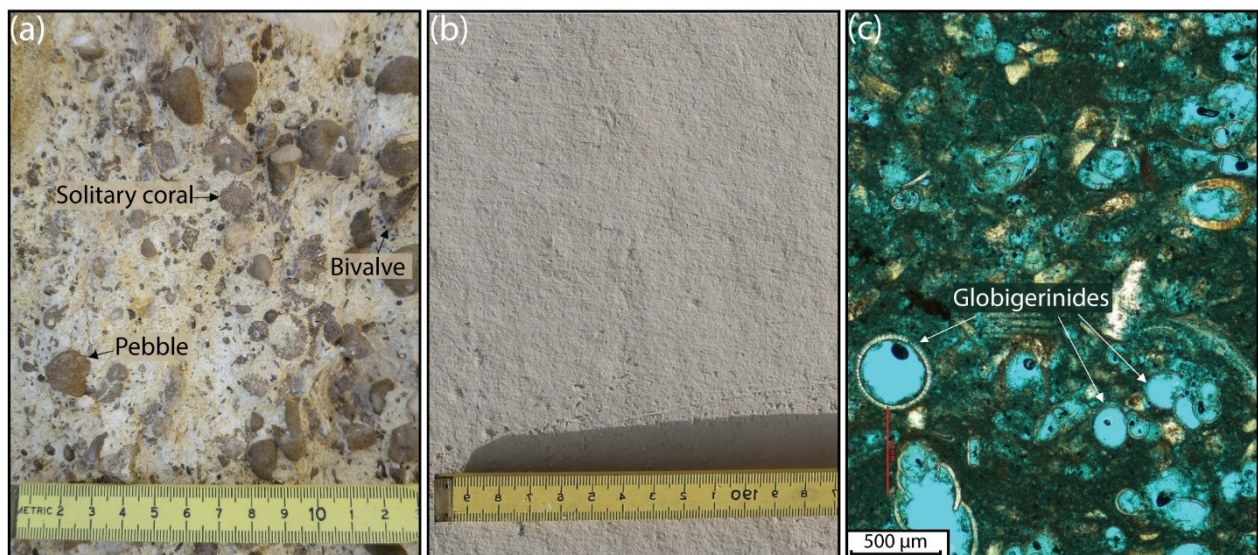


Figure 5.3. (a) The photo shows the MGLM-C1 unit, where an example of a solitary coral, a bivalve and a phosphoritic pebble is pointed out. Scale on yardstick is in cm. (b) The photo shows the very fine, micritic limestone of the MGLM-2. Scale on yardstick is in cm. (c) Photomicrograph of the MGLM-2, showing several globigerina foraminifers.

The matrix is seen as a dark brown mass with a cryptocrystalline texture in the optical microscope, filling in the area between the grains and fragments (Fig. 5.4). The SEM reveals that the matrix contains some very fine grains with traces of aluminum and magnesium, most likely being fine grained clays (Fig. 5.5). A relatively high content of quartz is also present in the matrix. Since the foraminifers are well preserved they contribute to the intragranular porosity in the rock, which is mainly obtained in the foraminifer chambers. This intragranular porosity is dominating, but some intergranular porosity is found in between the grains as well (Fig. 5.4).

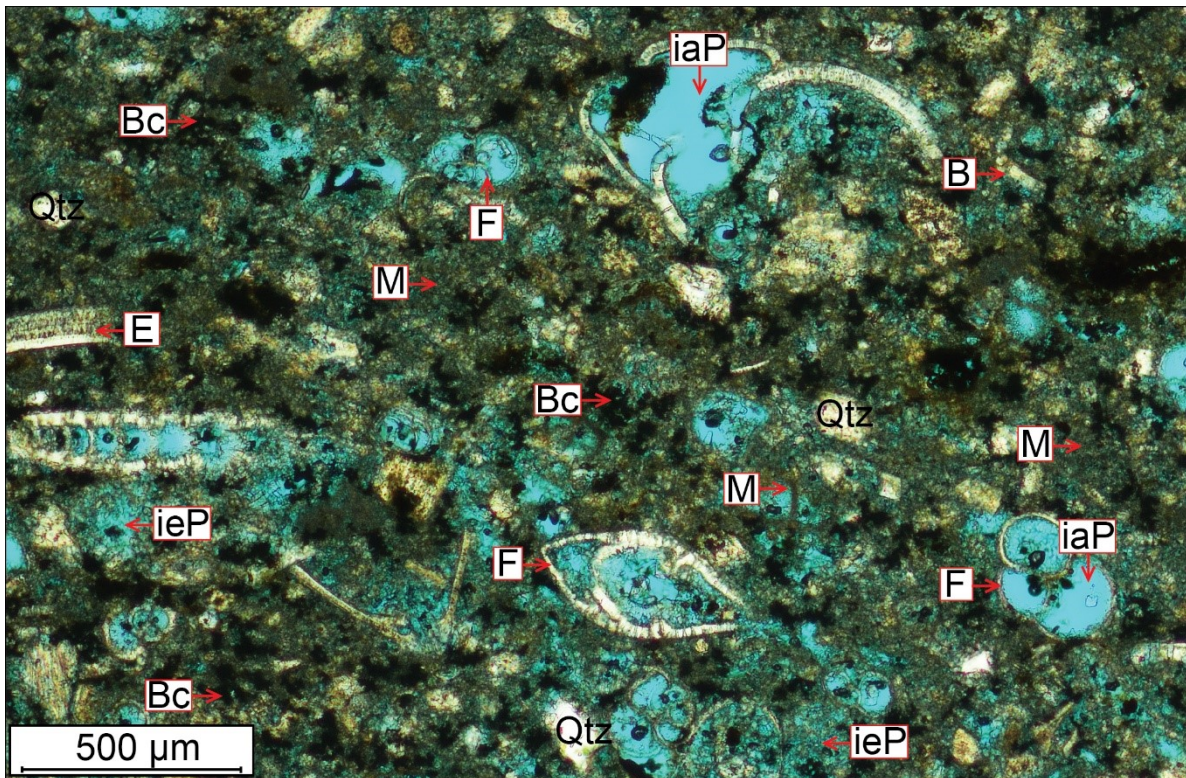


Figure 5.4. Thin section photomicrograph in plane polarized light of the MGLM-2, host rock between locality V1 and V2. The clear blue color is due to the epoxy in which the samples was prepared with, indicating pore space. Fossils of Echinoderm fragments (E), Bivalves (B), and Foraminifers (F) are highlighted, as well as the inter- (ieP) and intragranular (iaP) porosity and matrix (M). Dark brown to black patches are thought to be bacterial shrubs (Bc) as a result of hydrothermal activity.

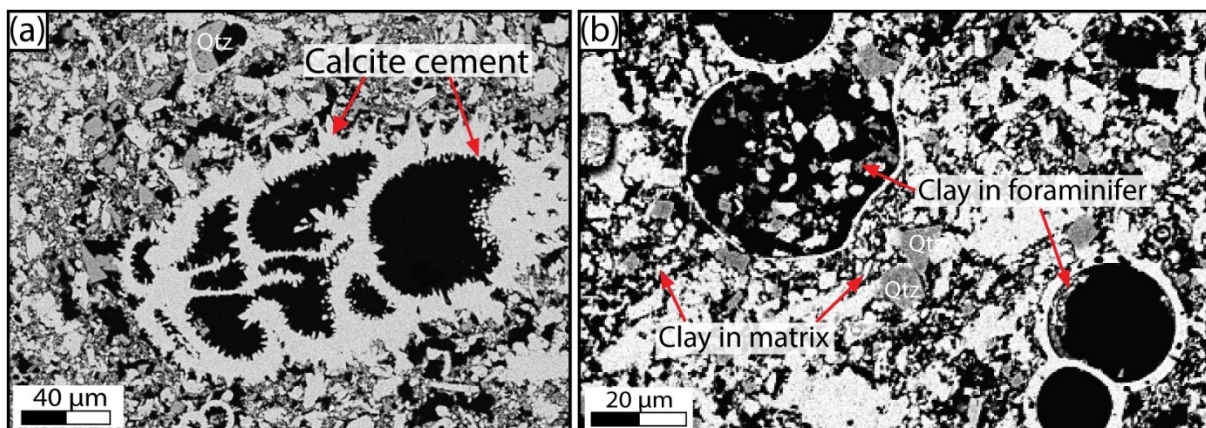


Figure 5.5. (a) Calcite cement (dog tooth) growth on both the inside and outside of a foraminifer shell. (b) Fine grained clay material can be observed both in the matrix and inside some of the foraminifer chambers. The foraminifers pointed out here do not show calcite cement growth.

The average porosity of the host rock, based upon porosity estimations from five of the host rock samples, is 4.1% based on photomicrographs and 13.6% based on BSE-SEM images. Although the MGLM-2 is generally homogenous, some less porous zones are observed in thin sections. Some of these zones coincide with microfractures, where the area around the fracture has lower porosity. Figure 5.6a shows a zone like this in the host rock, where an area extending

approximately 2 mm out from the fractures seem to contain more matrix and less pore space than the majority of the rock. Figure 5.6b shows a partly open fracture, contributing to the secondary porosity, but might also decrease permeability as a result of bacterial growth. Differential porosity is also observed in some of the thin section samples from the mounds. Figure 5.7 shows an example of this where both a more porous zone, or vein (A), and a less porous zone (B) is present in the same thin section.

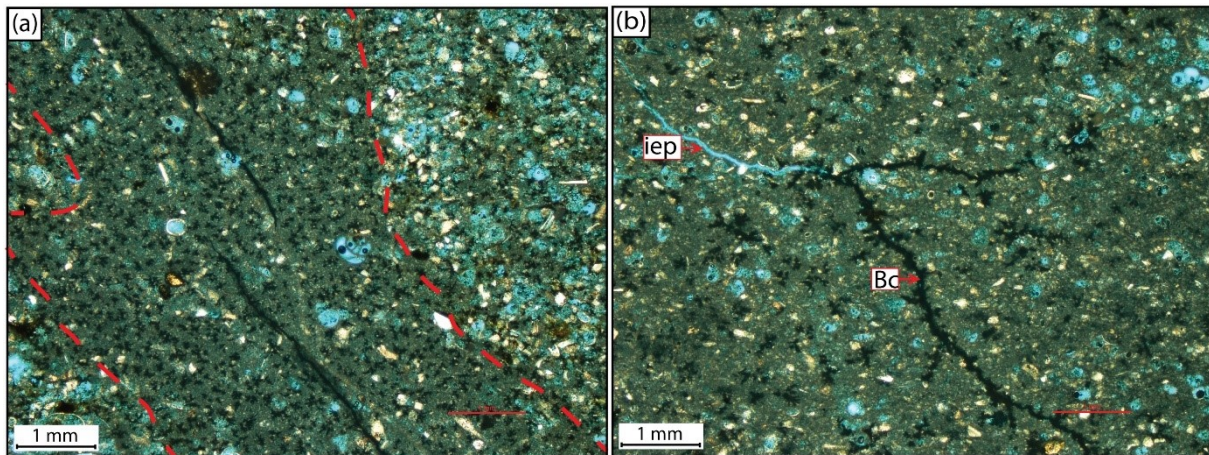


Figure 5.6. Thin section photomicrograph in plane polarized light of the MGLM-2, host rock between locality V1 and V2. (a) Two microfractures surrounded by a darker, less porous zone compared to the host rock. The transition is marked by the red dashed line. (b) A partly open fracture contributing to intergranular porosity (iep). The dark part of the fracture are blocked by what appear to be bacteria (Bc).

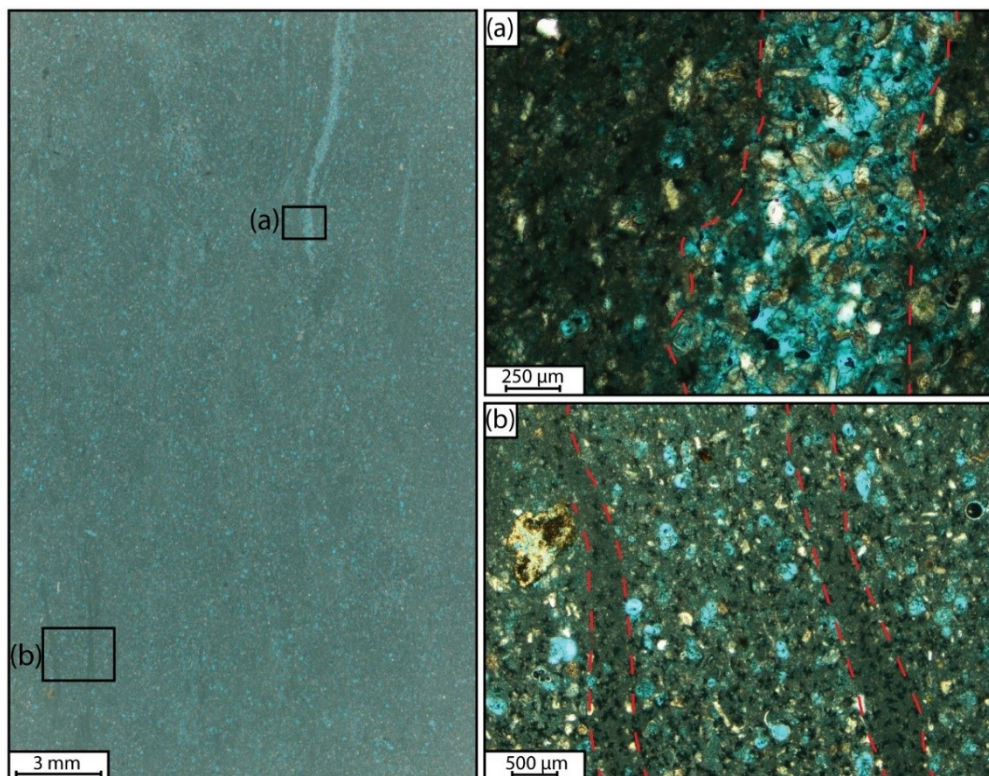


Figure 5.7. Scan of thin section from mound-type locality is shown to the left. The zones, or bands, with higher and lower porosity is visible from the scan, but obvious in microphotographs in (a) and (b) to the right.

5.3 Mound-type localities at Ras ir Raheb

As stated earlier, six of the nine localities in this project are mound-type localities (see Fig. 1.2 and Section 1.3.2). These are all situated at wave-cut platforms and cliff ledges immediately south of Ras ir Raheb. The localities are marked on the map in Fig. 5.1b. The fracture networks which constitute these localities are comprised of small-scale faults and extensional fractures in relation to fault damage zones. No veins were observed in the area. For each of these localities, a topographic profile, geometric and topological data were collected, as well as rock samples from mound and adjacent host rock. Line maps and summary figures for each locality are presented herein; for complete documentation, field photos, photomosaics and digitized map of the fracture networks of each locality, see Appendix I.

5.3.1 Mound locality V1

Locality V1 is a fracture network situated on the top of the wave-cut platform, in the MGLM-2 unit (Fig. 5.1), close to locality V2 and V7. It covers a 350 cm long part of a fault damage zone located in a shallow slope that steepens towards the east. A line drawing of the fracture system is shown in Figure 5.8a. The fracture system is comprised of three main segments. The easternmost of the segments is about 115 cm long and is NE-trending (segment III in Fig. 5.8a). The most prominent feature of this segment is the complex fracture network along it (complex zone E, Fig. 5.8a), and the high topographic relief it shows compared to the surroundings, which can be seen in Figure 5.8f. This mound extends for approximately 80 cm along the segment, is 40 cm wide, and forms the largest mound on this locality. Segment III runs out from a much longer, E-trending segment (segment II in Fig. 5.8a). Only 330 cm of this segment is included as a part of the locality, but it continues west where it links up to another fracture in a hard linked damage zone which is highlighted as complex zone A in Figure 5.8a. Parts of this linkage zone can be seen in the western end of this locality (segment I in Fig. 5.8a). Three smaller zones of complexity are found along segment II, named B-D in Figure 5.8a. The smaller zones are less complex, and do not show as big topographic relief changes as the larger mound to the east. These smaller mounds are approximately 25 cm × 20 cm in extent.

Figure 5.8b-f shows the fracture system aligned with the branch intensity map and the connecting node frequency map, as well as graphs showing fracture intensity, connecting node frequency, and the topographic profile along the system. The five complex zones can be recognized as areas with higher branch intensity (Fig.5.8b), which means they have a higher total branch length per square meter. The zones also show higher connecting node frequency (Fig.5.8c), meaning they have a higher amount of connecting nodes per square meter, than the

surrounding area. Looking at the graphs we can see that the large topographic high in the eastern end (Fig. 5.8f), along segment III, corresponds with an increase in connecting node frequency (Fig. 5.8e) and fracture intensity (Fig.5.8d). The two complex areas, C and D, in the middle of segment II, can be traced through the fracture intensity graph and the connecting node frequency graph as peaks. In the topographic profile, however, complex zone C and D is manifested as one wide mound instead of two. Complex area “B”, in the relay linkage zone, is not associated with a corresponding high on the topography profile, but shows a positive correlation through the branch intensity- and connecting node frequency maps as well as the fracture intensity and connecting node frequency graphs. A slight deflection in the topographic profile can be observed in the western end, where complex zone A along segment I is found. Complex zone A is also traceable through the graph of connecting node frequency and fracture intensity.

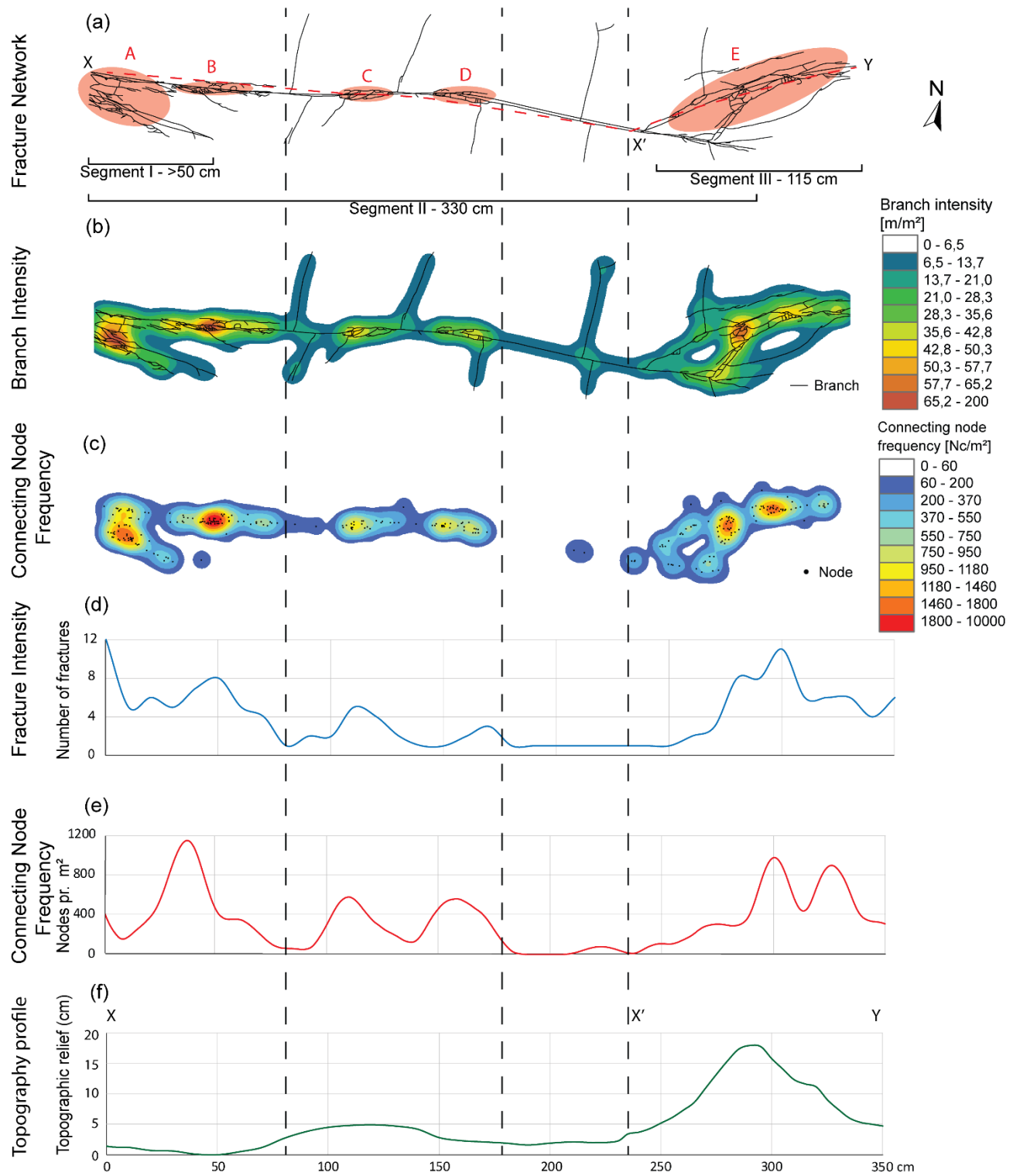


Figure 5.8. (a) Line drawing of locality V1, showing the three main segments. The more complex zones are marked with soft red and labeled A-E. (b) Branch intensity map (c) Connecting node frequency map (d) Fracture intensity graph (e) Connecting node frequency graph (f) Topographic profile. The black dashed lines are meant as guidelines for easier correlate between the maps and graphs.

5.3.2 Mound locality V2

The locality is found three meters south of locality V1, on the same platform (Fig. 5.1), covering a 275 cm long fracture system, including five complex zones, illustrated in Figure 5.9a. The system is oriented E-W and can be divided into two main segments, segment I and segment II in Figure 5.9a. Segment I comprise one large complex zone, complex zone A in Figure 5.9a. Complex zone A is approximately 85 cm long and 35 cm wide, and shows a clear topographic relief. This mound is heavily fractured, and a small bush growing within it was removed during data sampling. Several of the fractures along segment I contain soil and root fragments. Segment I splays into several fractures and dies out towards the west, but towards the east it is hard-linked to segment II through complex zone B. Segment II, approximately 135 cm, constitute the eastern half of the system and contains three small complex zones titled C, D and E in Figure 5.9a. These small complex zones range in length between 20 - 30 cm, with a width between 15 - 20 cm. Outside of the locality segment II links to another fracture set in a large complex relay zone.

Further, Figure 5.9 shows the fracture system (a) aligned with the branch intensity map (b) and the connecting node frequency map (c), as well as graphs portraying the fracture intensity (d), connecting node frequency (e), and the topographic profile. The three graphs are all located along the same profile, highlighted with soft red color in Figure 5.9a. The complex zones marked in Figure 5.9a, are easily recognized in the branch intensity map as areas with higher branch intensity, and in the connecting node frequency map as areas with a higher frequency of connecting nodes, although complex zone C is a little less evident than the others. The areas with higher branch intensity are characterized by several small branches, while the areas with lower branch intensity has few but generally much longer branches. The more complex zones also coincide with a deflection in the graphs. The positive correlation is best visible for the largest mound in complex zone A along segment I. Both the fracture intensity graph and the topographic profile show nice positive curves. The connecting node frequency graph does also show a positive correlation, but a very high, sharp peak stands out in comparison to the latter ones. Complex zone B show positive correlations through both the fracture intensity and the connecting node frequency graphs, but is not as evident in the graph showing the topographic profile. The small complex zone C can be recognized through a small deflection in all of the three graphs, while complex zone D and E shows a somewhat higher deflection in the fracture intensity graph and the connecting node frequency graph.

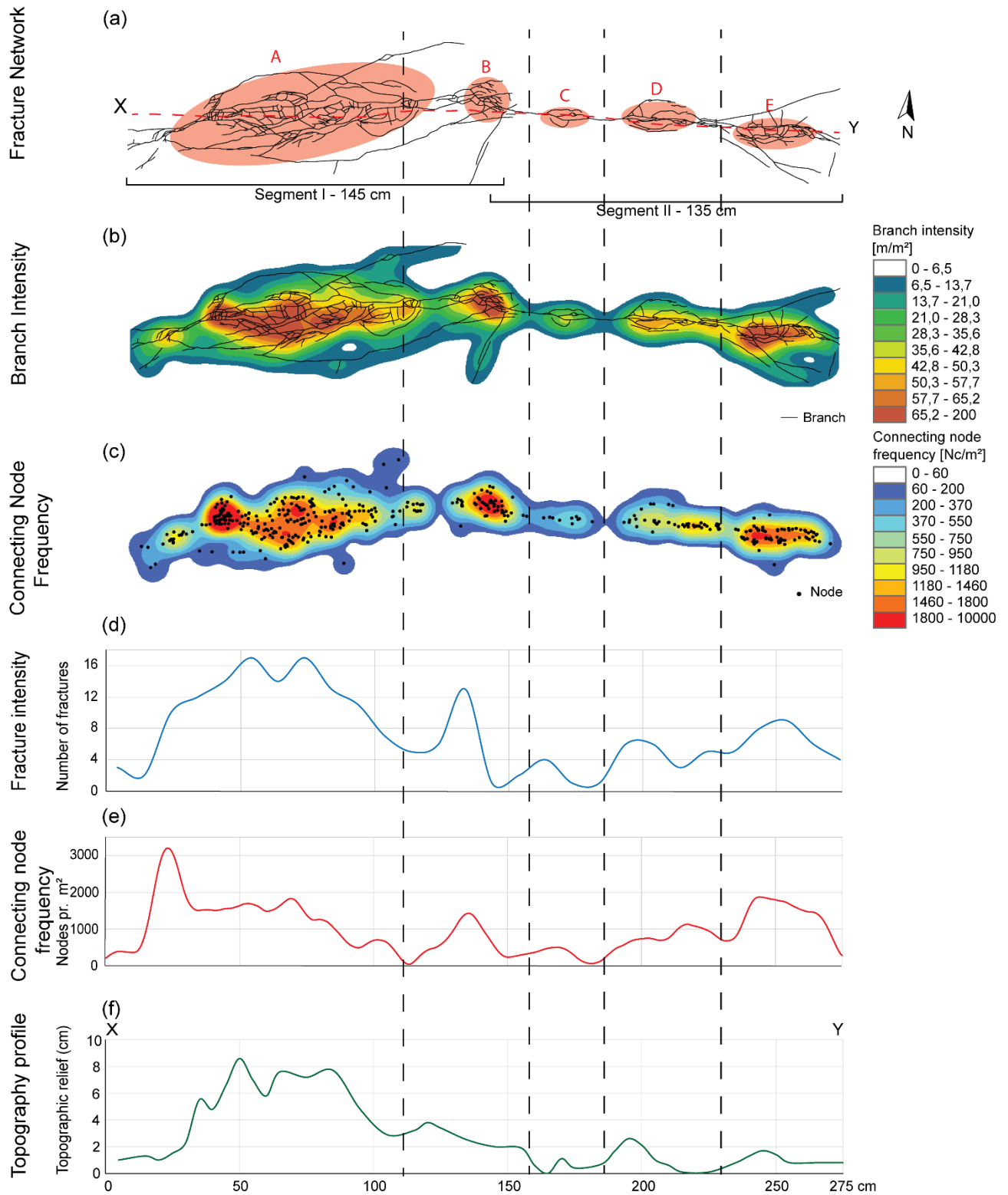


Figure 5.9. (a) Fracture network, locality V2. Showing the two main segments, and the more complex zones highlighted with a light red color. The red dashed line shows the placement of the graphs in Figs. d, e, and f. (b) Branch intensity map. (c) Connecting node frequency map. (d) Fracture intensity graph. (e) Connecting node frequency graph. (f) Topographic profile. The black dashed lines are meant as guidelines for easier correlation between the elements in the graphs and maps.

5.3.3 Mound locality V4

Locality V4 is situated in the damage zone in the hanging wall of fault F7 (Fig. 5.1b). Stratigraphically it is located immediately below the MGLM-C2B, in the MGLM-2. The fracture network of this locality is NW-trending, and comprises the easternmost part of a tip damage zone. The terrain, in which it is located, steepens towards the east where the MGLM-2 is capped by the MGLM-C2B. A digitized map of the fracture system is shown in Figure 5.10a. In contrast to the other mound localities, which are hard-linked, locality V4 consists of four soft linked main segments. The westernmost of these segments, segment I, (Fig.5.10a) is hard-linked to fault F7 outside the chosen area of study. Segment II is comprised of several smaller, hard-linked segments, and constitute complex zone A. Segment III is comprised of one segment, with a few smaller fractures splaying out from it, while segment IV is comprised of two hard-linked segments, marked as complex zone B in Figure 5.10a. All four main segments show displacement, with a maximum at the center and a decrease towards the tips, just like what one would expect of the displacement along a fault.

The fracture network in Figure 5.10a is aligned with the branch intensity map (b) and the connecting node frequency map (c), as well as graphs portraying the fracture intensity (d), connecting node frequency (e), and the topography profile (f). The three graphs are all located along the same profiles, marked with red dashed lines in Figure 5.10a. Complex zone A can be recognized in the branch intensity graph, just right of the area where segment I and segment II seems to merge. Segment III and segment IV appear as isolated bands, and complex zone B is hard to trace in the branch intensity map. Due to the simple structure of the fracture network there are few connecting nodes, and the connecting node frequency map only shows small clusters. However, the clusters observed in the connecting node frequency map can be traced to match the areas in the branch intensity map where the branch intensity increase, and they also coincide with higher fracture intensity in the graph portrayed in Figure 5.10d, and peaks in the connecting node frequency graph in Figure 5.10e. The topographic profile in Figure 5.10f, which portrays the total of the four segments, shows a decrease in relief towards the ends of the fracture network, and a peak in the middle which can be recognized as the overall trend for both the fracture intensity graph and the connecting node frequency map as well.

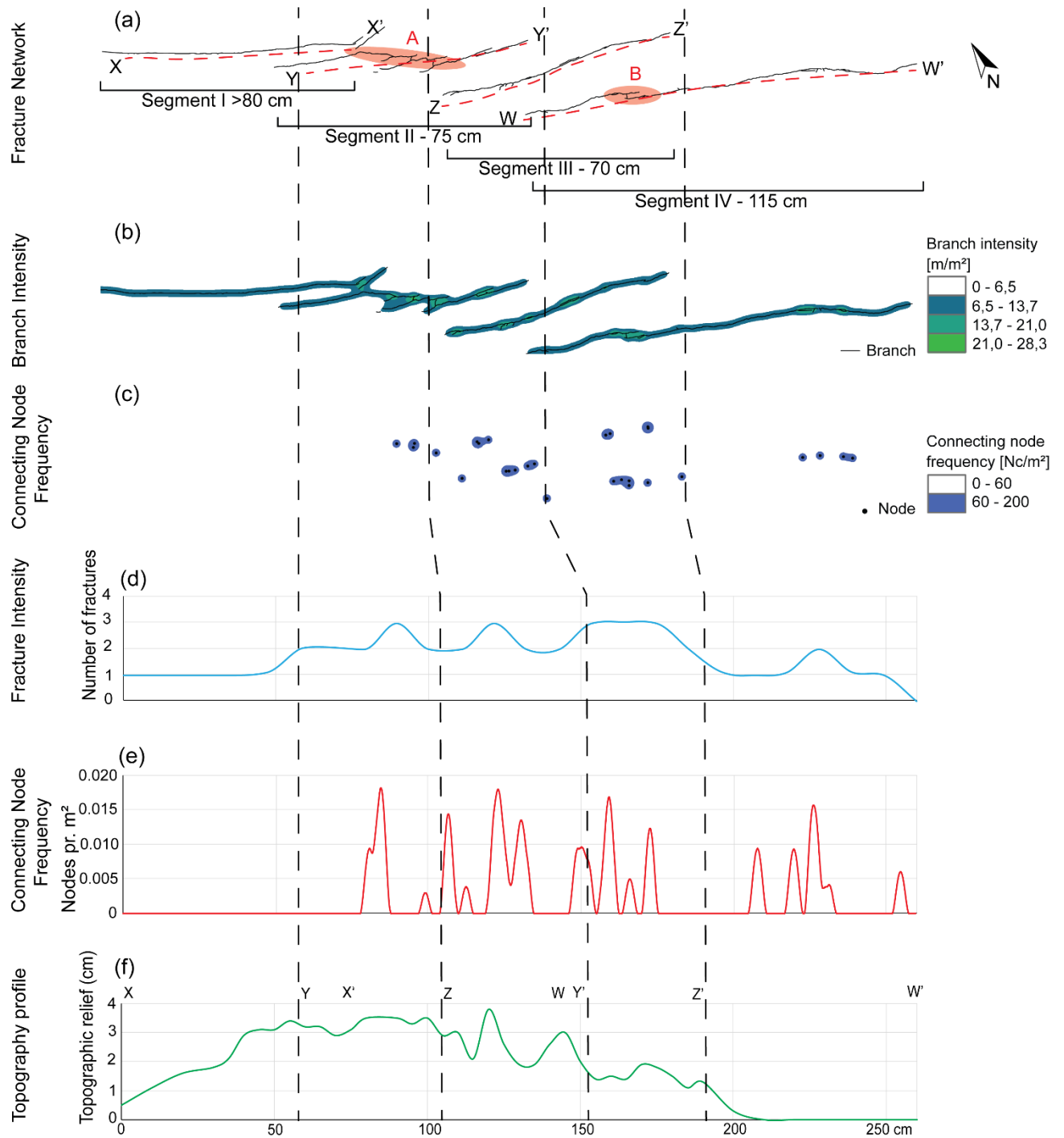


Figure 5.10. (a) Digitized map of the fracture network at locality V4. The light red color highlight the more complex zones, while the red dashed lines show the placement of the graphs in d, e and f. (b) Branch intensity map. (c) Connecting node frequency map. (d) Fracture intensity graph. (e) Connecting node frequency graph. (f) Topographic profile. The black dashed lines are meant as guidelines to easier correlate the maps and graphs.

5.3.4 Mound locality V7

The locality is situated in the MGLM-2 on top of the same wave-cut platform as locality V1 and V2, approximately 20 m further south (Fig.5.1b). As locality V1 and V2, it is located in the gently dipping slope. It constitutes a part of the W-trending fault F5 (Fig. 5.1b) which can be traced off the ledge to the west and down through the stratigraphy where it shows an offset of 20 cm in a marker horizon within MGLM-1. Digitized map the localities' fracture system can be seen in Figure 5.11a, where the more complex areas are highlighted with light red color and labeled A-D. The locality is limited to 3 m of the F5 fault, and is composed of two main segments, linked together in a relay with a more complex appearance and higher relief than the surrounding rock. This breached relay constitutes complex zone B, which is the largest complex zone of the V7 locality. Complex zone B is highly fractured and contain loose rock fragments, soil filled fractures and traces of old roots. A bush was growing in the middle of it, but was removed during collecting of the data, leaving a brecciated area behind. Segment I got a straight E-W trend, and comprise the western half of the locality. Complex zone A is found along segment I, as an initiation to the relay. Segment II shows a slightly more ESE-oriented trend, and can be traced into the MGLM-C2B, approximately 130 cm towards the east, where it shows an offset of 7 cm. Complex zone C and D are found along segment II.

The fracture network of the location is presented together with the branch intensity map, the connecting node frequency map, and graphs illustrating the fracture intensity, connecting node frequency and topography through Figure 5.11a-f. The three graphs are all located along the same profile, marked by a red dashed line in Figure 5.11a. The complex zones featured in Figure 5.11a can be recognized in both the branch intensity map (Fig. 5.11b) and the connecting node frequency map (Fig. 5.11c) as areas of higher branch intensity and connecting node frequency, respectively. Complex area B is easily recognized as the highest peak in both the topographic profile (Fig. 5.11f), the fracture intensity graph (Fig. 5.11d), and the connecting node frequency graph (Fig. 5.11e). The connecting node frequency graph, however, shows a down-dip in the middle of complex zone B where the bush was situated. Complex zone A along segment I is visible through the fracture intensity graph and the connecting node frequency graph, but does not give a deflection along the topographic profile. A peak in all the three graphs can be correlated with complex zone C, while complex zone D can only be recognized in the graph portraying the connecting node frequency.

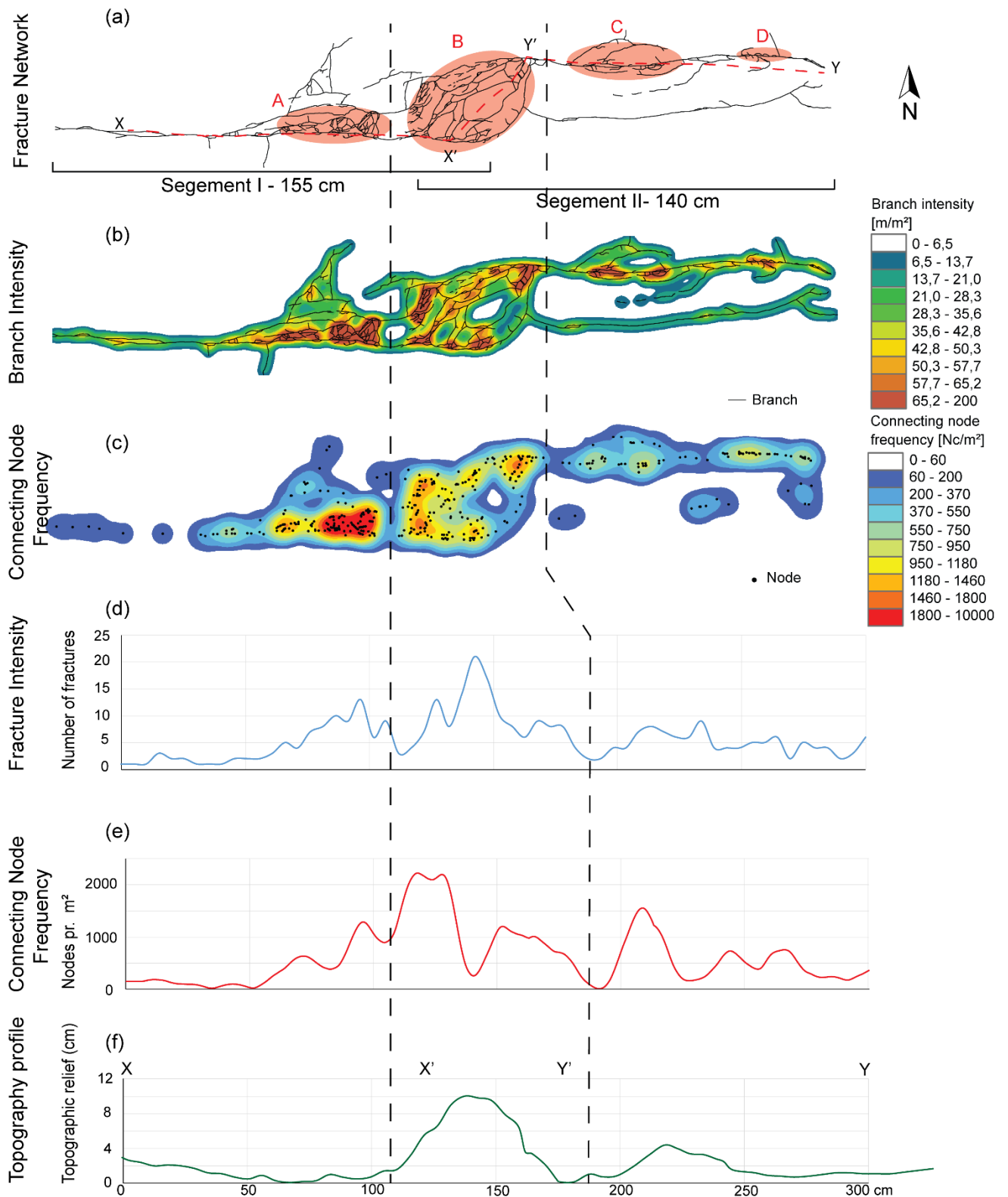


Figure 5.11. (a) Digitized map of the fracture network at locality V7. More complex zones are highlighted by a light red color, while the red dashed line shows the placement of the graphs in Figs. d, e and f. (b) Branch intensity map. (c) Connecting node frequency map. (d) Fracture intensity graph. (e) Connecting node frequency graph. (f) Topographic profile. The black dashed lines are meant as guidelines for easier correlation between the maps and graphs.

5.3.5 Mound locality V8

Locality V8 is a fracture system located in the hanging wall of one of the relatively large faults in the study area (displacement 5.1 m), F16 (Fig.5.1b), 10-12 m from the fault core. Like locality V4, it is situated in the slope of the MGLM-2, just beneath the MGLM-C2B. A digitized map of the locality's fracture system can be found in Figure 5.12a. The locality consists one 90 cm long segment, labeled segment I, and a 200 cm long segment, labeled segment II. Segment II continues in both directions outside the outlines of the locality and dies out a couple of meters in the western direction. Towards the east, segment II cuts through the MGLM-C2B where an offset of 4 cm can be observed. The segment carries on through the conglomerate layer for about 40 cm before it dies out. Segment I, which is approximately 90 cm long, breach out from segment II and dies out just before it reaches the MGLM-C2B. Three complex zones are found along segment II, marked in Figure 5.12a. Complex zone B comprise the area where segment I runs out from segment II. Complex zone C is stratigraphically situated just beneath the MGLM-C2B and the fractures within it show splaying tendencies as segment II approach the conglomerate bed.

The digitized map in Figure 5.12a is aligned with the branch intensity map (b) and the connecting node frequency map (c), above graphs portraying the fracture intensity (d), connecting node frequency (e), and the topographic profile (f). The three graphs are all located along the same profile, marked as a red dashed line across the digitized map of the fracture network. The three complex zones can be recognized in the branch intensity map as areas with higher branch intensity. Complex zone A and B can also be recognized in the connecting node frequency map as areas of higher connecting node frequency. Complex zone C is not that evident in the connecting node frequency map, but seems to merge into complex zone B. The highest peak in the topographic profile (Fig. 5.12f), connecting node frequency graph (Fig. 5.12e), and fracture intensity graph (Fig. 5.12d) all coincide and can be correlated to complex zone B. Complex zone A can also be traced through the three graphs, although the topographic profile and the fracture intensity graph apparently contain both a peak and a base within the same area. The easternmost complex zone, C, can only be observed in the connecting node frequency graph. A peak in the fracture intensity graph appears immediately before complex zone C.

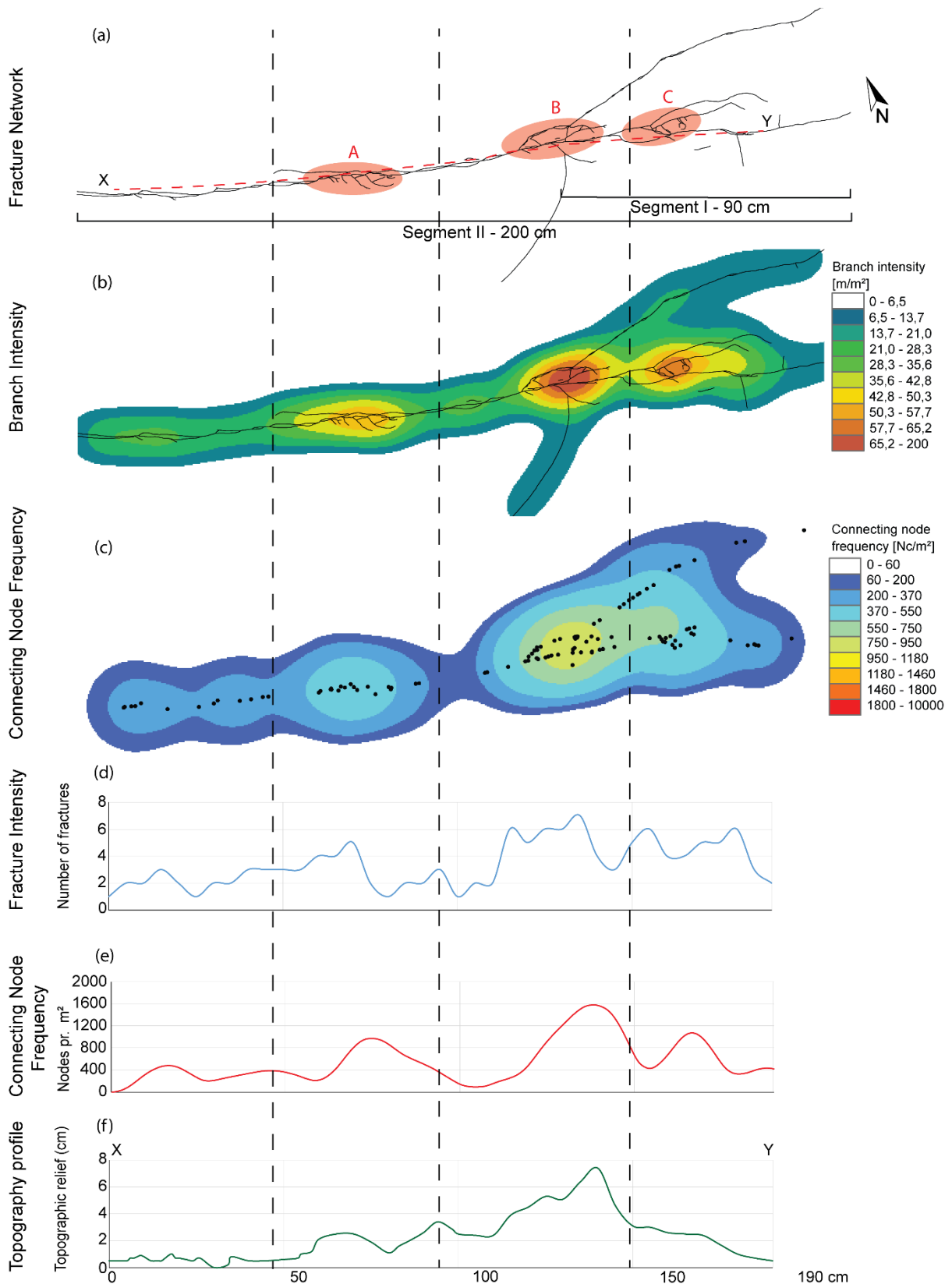


Figure 5.12. (a) Digitized map of the fracture network, at locality V8. More complex zones are highlighted by a light red color. The red dashed line shows the placement of the graphs in d, e and f. (b) Branch intensity map. (c) Connecting node frequency map. (d) Fracture intensity graph. (e) Connecting node frequency graph. (f) Topographic profile. The black dashed lines are meant as guidelines to easier correlate the maps and graphs.

5.3.6 Mound locality V9

Locality V9 is located approximately 100 m south of location V4, in the same stratigraphic level, just below the MGLM-C2B (Fig. 5.1b). The fracture network forms part of the damage zone of fault F9, which shows an offset of 35 cm measured in the LGLM-C1, although the offset along the studied part of the fracture network ranges from <1 cm to 5 cm. The chosen section includes 235 cm of the fault's damage zone fracture network, comprised of two main segments. The network shows an advanced system with four structurally complex zones. A digitized map of the locality's fracture system is found in Figure 5.13a. The four more complex zones are highlighted in this figure, and labeled A-D. The westernmost zone, A, is largest, and approximately 60 cm long. It shows fractures with higher aperture and higher relief than complex zone B, C and D and represent the largest mound at the locality. The smaller complex zones, B, C and D is about 20-30 cm long, and in which complex zone C constitutes the hard-linked relay zone between segment I and segment II. A small bush was growing in the mound that constitute complex zone A, but as for the other localities this was removed during collecting of data. The ground in which the locality is situated has a dip of 12° towards the west in the western end of the fracture network, increasing to 38° in the eastern end where the fracture network meets the overlying MGLM-C2B.

The digitized fracture map in Figure 5.13a is lined up with the corresponding map of the branch intensity (b) and the connecting node frequency (c), as well as graphs of the fracture intensity (d), connecting node frequency (e), and a topography profile (f). The fracture intensity graph, connecting node frequency graph, and topographic profile are all gathered along the same profile, marked on the map of the fracture network in Figure 5.13a as a red dashed line. A clear, positive correlation can be observed between the topographic profile (Fig. 5.13f), connecting node frequency (Fig. 5.13e), and the fracture intensity (Fig. 5.13d) in the area of complex zone A. Complex zone A can also be recognized in the western end of the branch intensity map (Fig. 5.13b) and the connecting node frequency map (Fig. 5.13c) as areas with higher branch intensity and connecting node frequency, respectively. However, a depression in the large mound/complex area A can be observed in the branch intensity map, connecting node frequency map, and the fracture intensity graph. This depression coincides with the area where the small bush was located. The three smaller zones of complexity, B, C and D, can also be recognized in the branch intensity map and the connecting node frequency map as areas of higher branch intensity and connecting node frequency. Complex zone B, next to the largest mound in complex zone A, can be recognized through all three graphs, though a bit weak in the

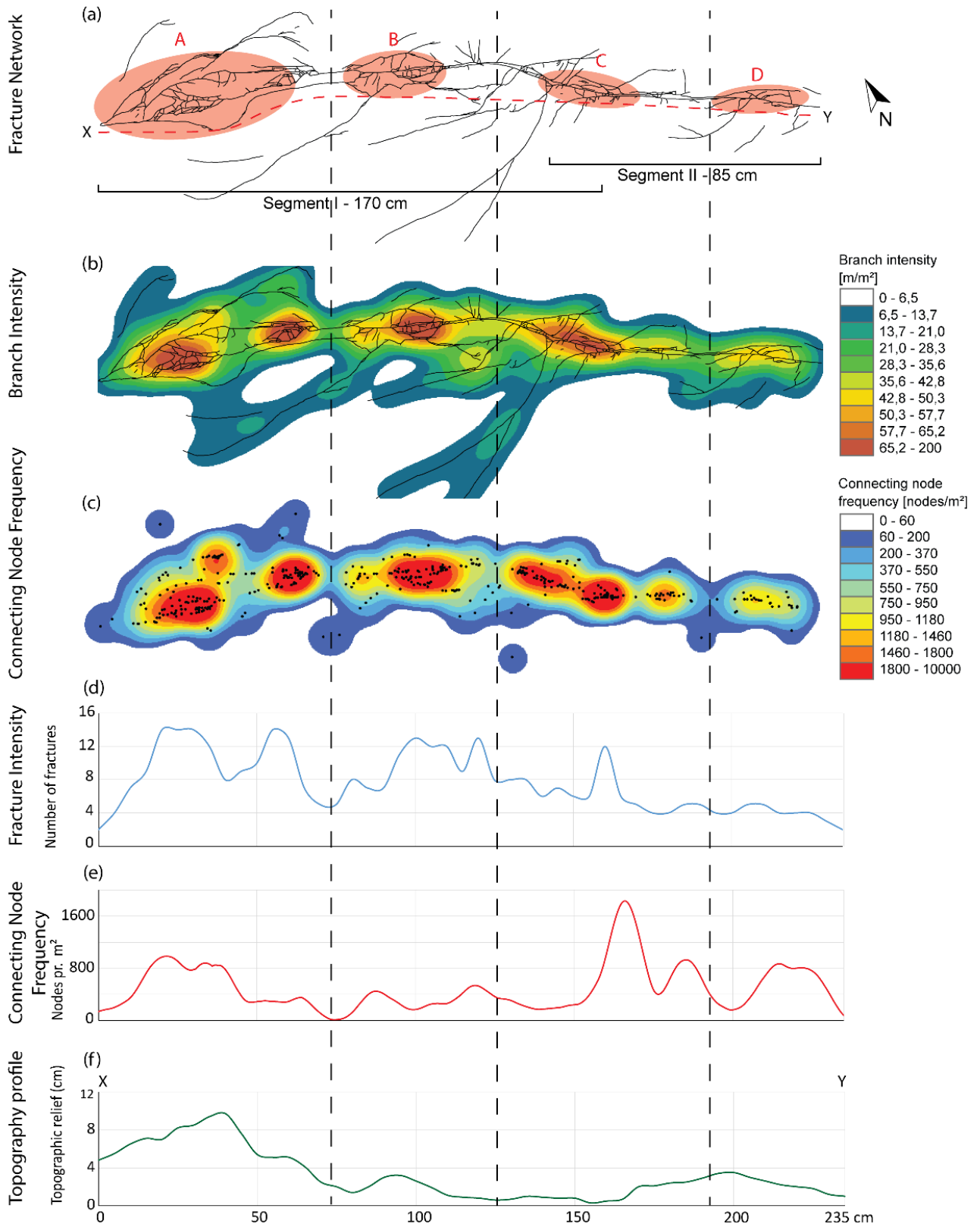


Figure 5.13. (a) Digitized map of the fracture network, at locality V9. The more complex zones are highlighted with a light red color. The red dashed line shows the placement of the graphs in Figs. d, e and f. (b) Branch intensity map. (c) Connecting node frequency map. (d) Fracture intensity graph. (e) Connecting node frequency graph. (f) Topographic profile. The black dashed lines are meant as guidelines to easier correlate the maps and graphs

topography profile and with a depression in the connecting node frequency map. Complex zone C shows a concentrated peak in both the fracture intensity graph and the connecting node frequency graph, but does not give any deflection in the topographic profile. The easternmost complex zone shows a positive correlation with the maps through the connecting node frequency graph.

5.4 Porosity and connectivity

5.4.1 Mound vs. Host porosity

Porosity estimations were carried out for one mound at each locality, and its corresponding host rock, as described in Chapter 4. The results from the digital image analysis of the photomicrographs and BSE-SEM imagery using ImageJ detected a subtle difference in host rock porosity and mound porosity. A minimum of 10 photomicrographs were analyzed for each thin section, half of them with 4× magnification and the other half with 10× magnification. The results from the porosity measurements from the *photomicrographs* are presented in Figure 5.14a, where each data point represents an analysis of one photomicrograph, and each column represents one thin section. The result shows great variations within each thin section/sample. The mound porosities vary from a minimum of 0.7% (location V8) to maxima 7.9% (location V2) with an overall average of 3.3%. The lowest porosity measured for the host rock is 0.3% (location V4) and the highest 8.0% (location V1/V2), with an overall average of 4.1%. However, the overall general trend is a slightly higher porosity in the host rock than the corresponding mounds.

Figure 5.14b display the results from the porosity analysis of the *BSE-SEM images*, the same way as the latter figure. Also here, a minimum of 10 images with 500× magnification were analyzed for each thin section. The mound porosities have a minimum and maximum value of 4.2% (location V8) and 31.6% (location V2) with an overall average of 12.2%. The host rock shows a minimum and maximum value of 8,2% (locality V8) and 21,7%, with an average of 14%. The analysis of the BSE-SEM images yields overall higher porosity values than the values attained using optical microscopy. This is due to the fact that both macro- and microporosity gets included in the measurements in contrast to the photomicrograph analysis where only the macroporosity are accounted for, naturally leading to lower values.

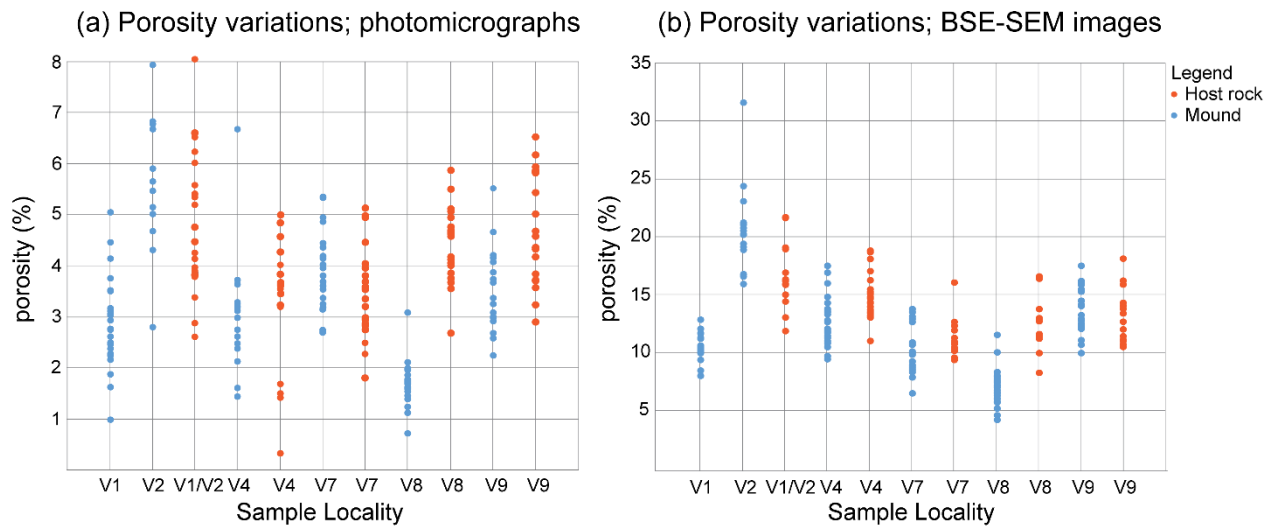


Figure 5.14. The diagrams present the results from the analysis of microphotographs (a) and BSE-SEM images (b) from the thin section samples from mound and host rock at each locality. Each dot represents one analyzed photo, and each column represents one thin section. The overall general trend shows a slightly higher porosity in the host rock compared to the mounds.

The difference in the 2D porosity can be visually observed when comparing binary BSE-SEM images from the mounds and their corresponding host rock sample (Figs. 5.15 and 5.16). In these images, the pore space is displayed in black, and the porosity numbers presented is the average porosity of the thin section from which the image is derived. Locality V1 has a host rock porosity of 16.5%, which is visually higher than the 10.7% pore space present in the corresponding mound. The host rock shows generally more macroporosity than the mound, which is dominated by microporosity. Since locality V1 and V2 are situated only a couple of meters apart, they are compared to the same host rock, and the same image is used to illustrate the host rock for locality V2. Comparing the host rock image from V2 with the mound image from the same location, it can be stated that the mound here holds a higher porosity than the host rock. This remark is reasonable as the mound porosity for V2 is estimated to be 20.6%, and thereby 4.1% higher than the porosity of the host rock. The difference in porosity is harder to observe by the naked eye in the images from the host rock and mound of locality V4, V7 and V9, as the host rock porosities is just a few percentage points higher than the mound porosities. The porosity of the host rock corresponding to locality V4 was estimated to 15%, 2.5% higher than the estimated porosity of the mound on locality V4. The images from locality V7 (Fig. 5.16) show a host rock with a porosity of 11.3% next to the image of the mound in which the porosity is estimated to 10.3%. The host rock of locality V9 contain only 0.3% more pore space than the corresponding mound, with porosity estimations of 14% and 13.7%, respectively. Locality V8 is the locality which show the greatest porosity differences between host rock and mound, with difference visible through the images in Figure 5.16. It can be observed that the

host rock image, with an estimated average porosity of 12.6%, has a higher amount of black and hence higher macro porosity than the corresponding mound image with a porosity of 7.1%.

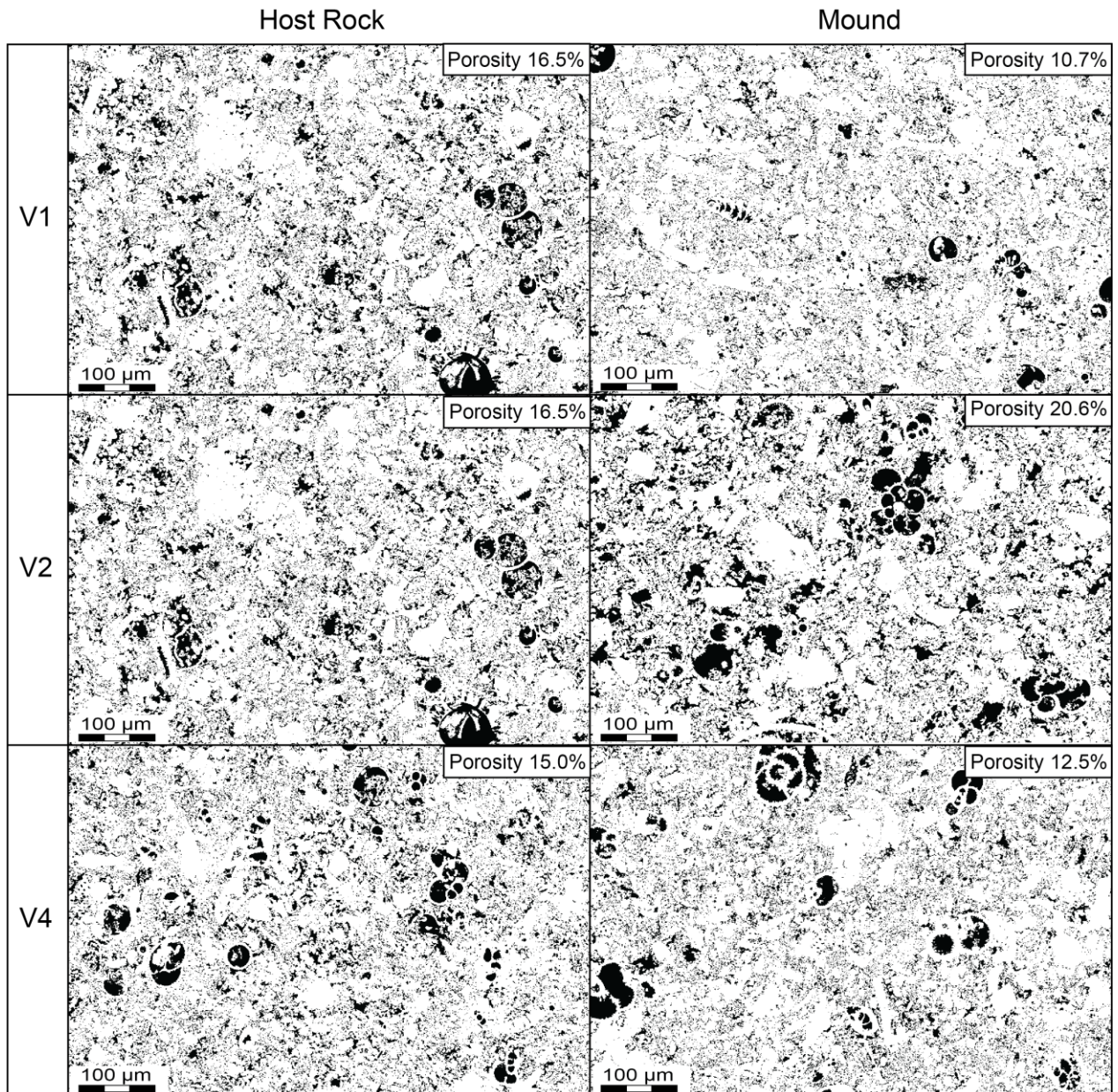


Figure 5.15. The figure shows a comparison of binary BSE-SEM images from the host rock and the corresponding mound for locality V1, V2 and V4. The general porosity for each thin section is pointed out in the uppermost right hand corner of each image (meaning it is not the porosity for the exact image displayed here).

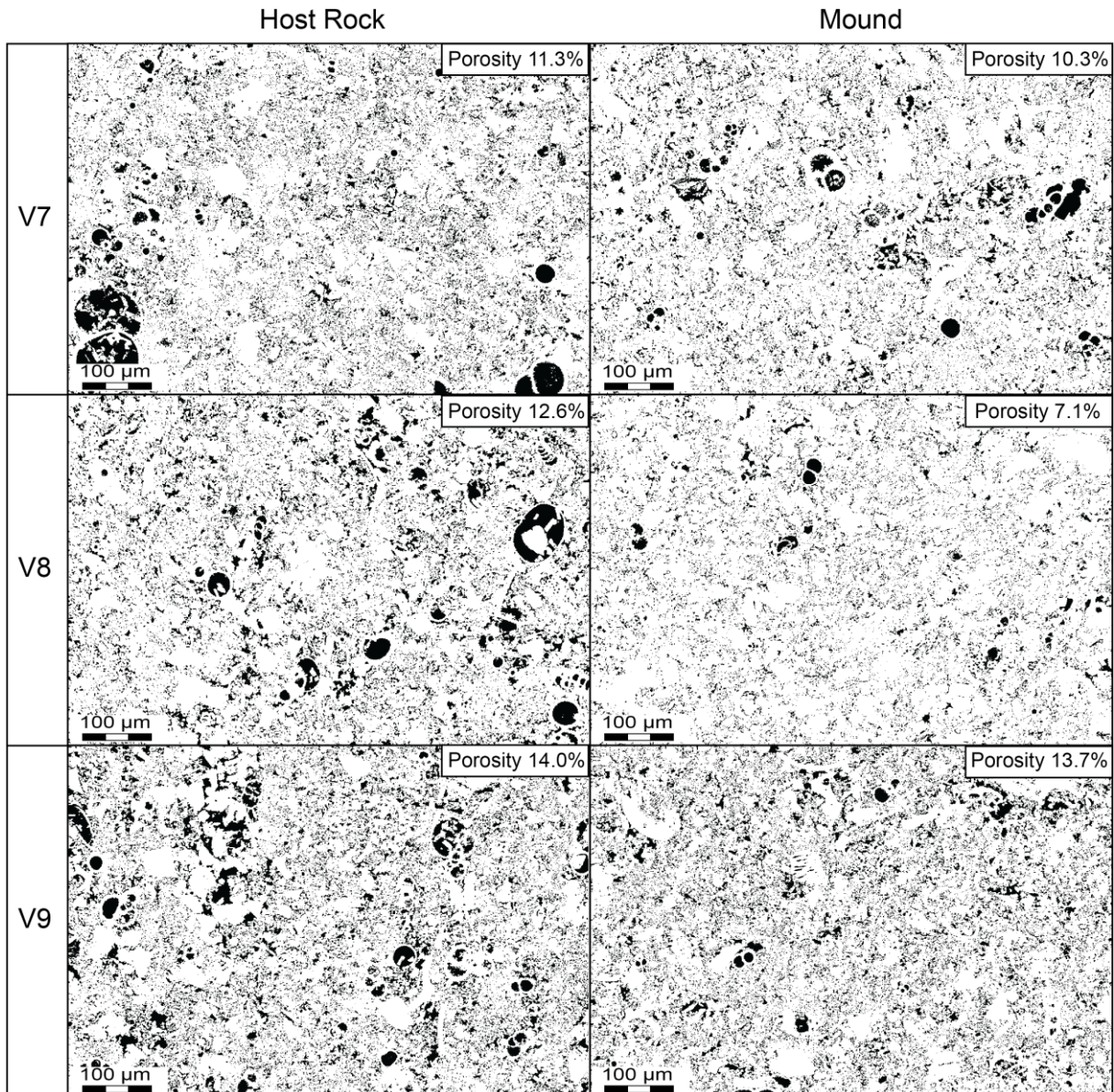


Figure 5.16. The figure shows a comparison of binary BSE – SEM images from the host rock and the corresponding mound for locality V7, V8 and V9. The general porosity for each thin section is pointed out in the uppermost right hand corner of each image (meaning it is not the porosity for the exact image displayed here).

5.4.2 Porosity statistics

Porosity statistics show that the values of the porosity measurements plot along a linear, straight line ($R= 0,98$ for BSE-SEM images and $R= 0,99$ for microphotographs) in a cumulative probability scale, indicating that the values are normal graded (Fig. 5.17). Since the values are normal graded they can be used in parametric tests to see if the populations show any significant differences in variance (squared standard deviation) or average values. Snedecor's F-test was used to check if the populations show significant differences in variance, while a Student's t-test was used to check if the average values of the populations show significant differences.

The level of significance is described by the factor α ; a low α - value indicate a test of high significance.

The porosity measurements are divided into three main data sets based upon the level of magnification on the photos used. One for 4 \times , one for 10 \times , and one for 500 \times magnification, and the possible difference in host rock and mound rock sample was kept in mind.

The results from Snedecor's F-test show that the variance for the mound values are greater than the variance for the host rock values for both the 4 \times - and 500 \times magnification, both with $\alpha=0.0005$, while the variances are not significantly different for the 10 \times magnification dataset which got $\alpha=0.005$.

The results from the Student's t-test show that average value for the host rock is significantly greater than the average value for the mound for all of the three data sets.

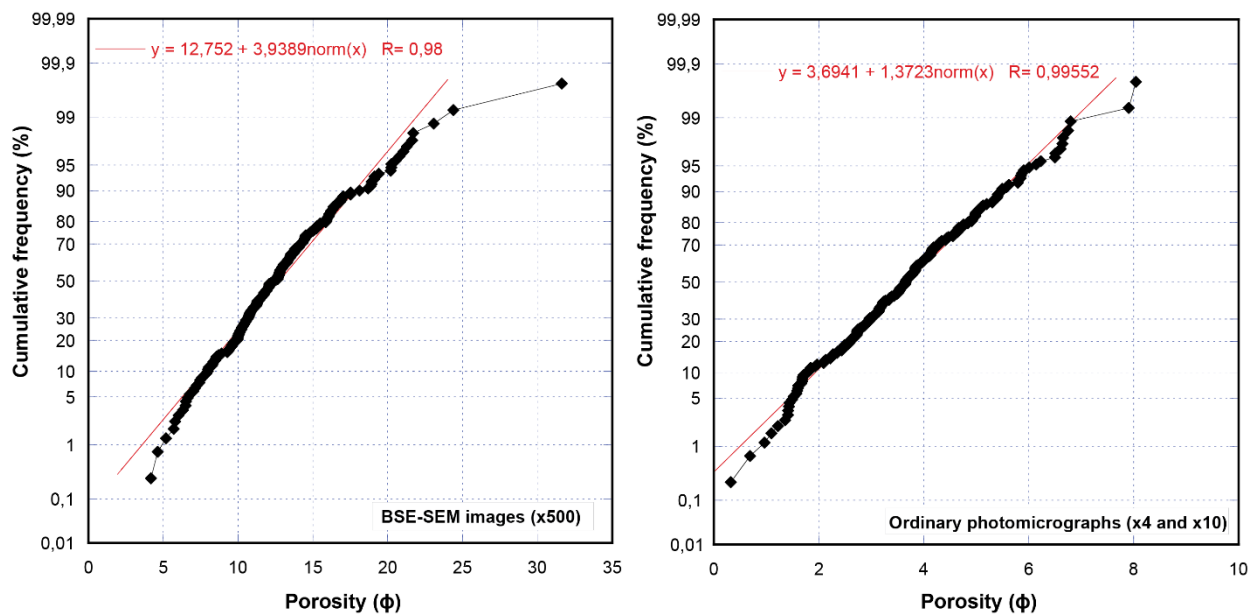


Figure 5.17. Probability scales showing the porosity vs. the cumulative frequency of the measurements for the BSE-SEM images to the left, and the microphotographs from the light microscope to the right. The R values are very close to one, and the values of the measurements plot along a straight line, showing that the values are normally distributed.

5.5 Redox-type localities at Ras ir Raheb

This chapter will present the redox-type localities found at Ras ir Raheb. These are stratigraphically located in the transition between the MGLM-C1A and the MGLM-2. Line maps and summary figures for each locality are presented herein; for complete documentation, field photos, photomosaics and digitized map of the fracture networks of each locality, see Appendix I.

5.5.1 Redox locality V5

This locality is situated approximately 400 m south of the other localities in the Ras ir Raheb area (Fig. 5.1b). Stratigraphically, it is located in the transition between the MGLM-C1A and MGLM-2, at a wave-cut platform. The studied system is a fault, labeled F27 in Figure 5.1b, with an outcropping trace length of 22 m consisting of several linked segments. It exhibits a SE-NW orientation, and dips approximately 60° towards the SW. Figure 5.18a shows a digitized map of the fracture network on the locality, pointing out the different segments and zones of structural complexity. Segment I is 795 cm long, and appears to link up with another segment (not labeled) through complex zone A in the northwestern end in a hard-linked relay zone. Linking up to segment I in the southeastern end is segment II, which in turn link with segment III. Also these linkage zones have high fracture density, and are marked as complex zone B and C. The 960 cm long segment IV constitutes the southeastern end of the studied part of the fault. In reality it stretches at least four meters further towards the SE, but do not show any displacement or redox-fronts. Another complex zone, E, is found along segment IV as the segment splays. The shorter segment, segment V, is found next to complex zone E. Segment V is linked to segment IV in both tips and the whole segment is included as a part of complex zone D.

Several redox fronts can be traced along the fault, some very clear and others more diffuse. A series of strong redox fronts are found in the footwall in an area in average 50 cm from the main fault segments. These strong redox fronts are tapering towards the SE, and disappear along segment IV. A couple of weaker, discontinuous redox fronts are observed further away from the main segments in the footwall. There are few redox fronts in the hanging wall in comparison to the footwall, and all redox fronts in the hanging wall are discontinuous. Figure 5.18a shows the fracture network of the locality and the outlines of some redox fronts. Two of the innermost redox fronts and the outermost observed redox front (discontinuous) of the footwall can be seen northeast of the fault segments, while two discontinuous redox fronts are marked in the hanging

wall at the southwestern side of the fault segments. These fronts are highlighted as they are the most prominent ones, and represents the main trend of the redox fronts at this location.

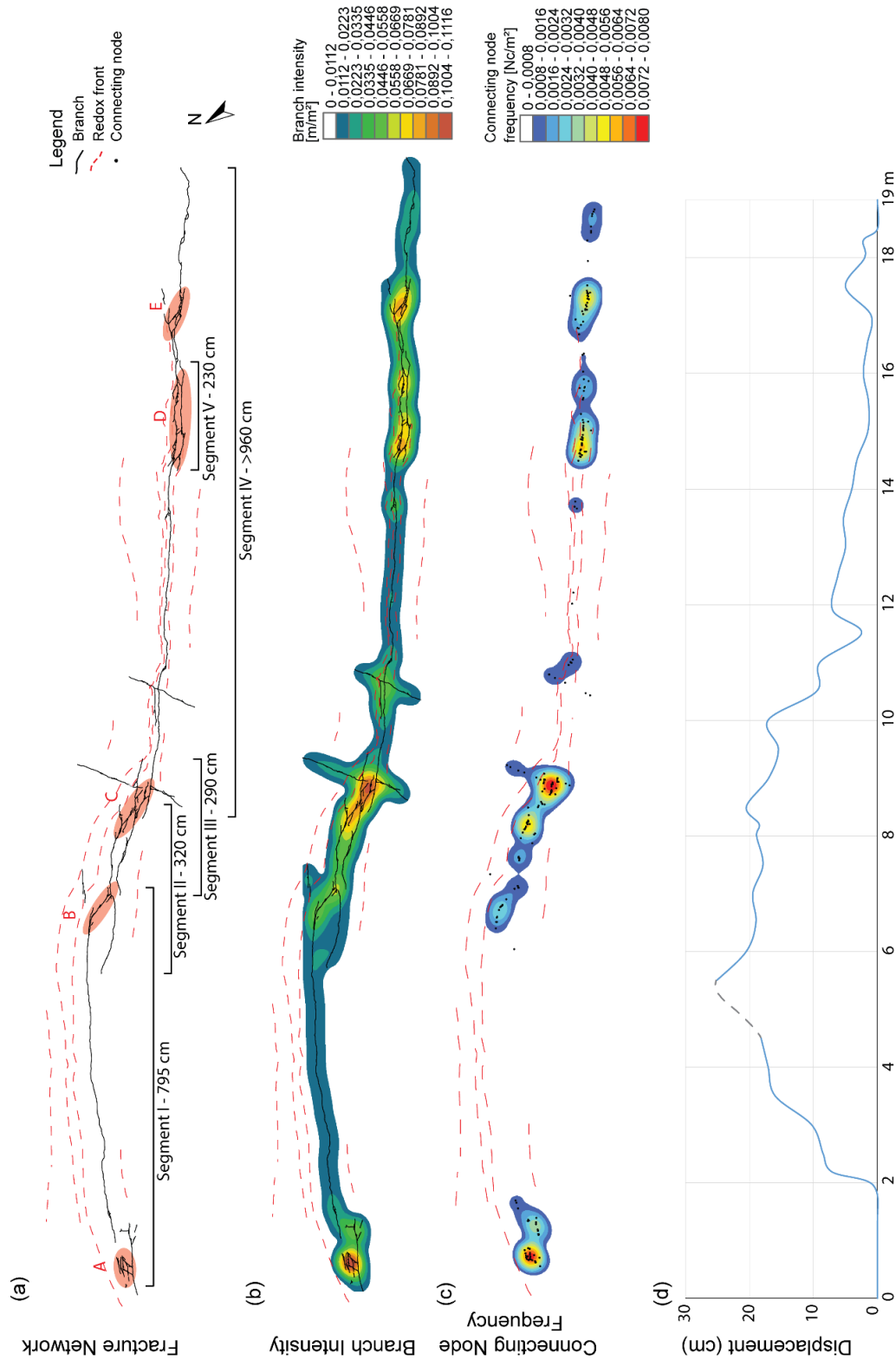


Figure 5.18. (a) Digitized map of the fracture network locality V5, with the oxidized rims showed as red dashed lines and complex zones highlighted with soft red color. (b) The branch intensity indicates higher density in linkage areas. (c) Connecting node frequency also increase in the areas where fault segments link. (d) Length-Displacement plot of the studied network. Dashed part of the curve indicates missing data due to erosion.

Corresponding contour maps of the branch intensity and the connecting node frequency are shown in Figure 5.18b and c. The redox fronts are also included in these maps, showed as red dashed lines. Areas of high branch intensity coincides with the areas of high connecting node frequency in the complex zones where the fault segments are linking. A length-displacement plot from the fault is presented in Figure 5.18d. It appears to be a correlation between the displacement and the width of the redox fronts in Figure 5.18a, b and c. The displacement is largest along segment I, and this is also where the redox fronts are at their widest. As the redox fronts narrows towards the SE, the displacement decreases. A correlation can also be seen between redox front width and higher branch intensity and connecting node frequency, as a vague trend of wider redox fronts around the complex zones can be observed, most prominent when looking at the outermost front. The redox fronts appear wider around complex zone B and C, and clearly get wider where they approach complex zone D.

Porosity estimations carried out from thin sections gathered in a section across the fault at locality V5 revealed that the porosity decrease from the footwall and towards the fault, before it shows a sudden increase again just before the fault plane, continuing to rise on the other side (Fig. 5.19).

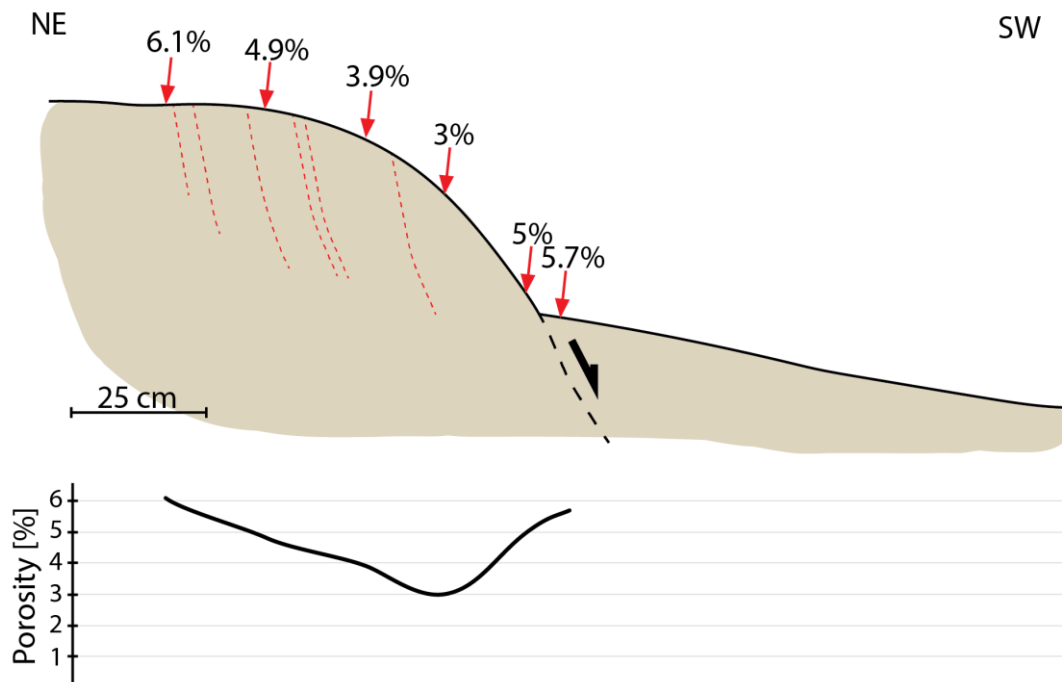


Figure 5.19. Sketch of profile through the fault at locality V5. The red dashed lines demonstrate redox fronts. The numbers are the estimated porosity of samples taken across the fault. The porosity decreases from the outermost sample in the footwall towards the center of the fault, where it quickly increases again as it reaches the fault plane. The graph demonstrates the gradual decrease and the following increase in porosity relative to the fault.

5.5.2 Redox locality V6

Locality V6 is located south of locality V9, in connection to fault F12 and F13 (Fig. 5.1b). Stratigraphically, it is situated in the uppermost part of the MGLM-C2A. The locality shows two cross cutting faults comprised by several fractures/minor faults showing displacements of 0-2.5 cm, all gathered within an area of about 4×4 m, and bound by a larger W-trending fault towards the south. A digitized map of the locality in Figure 5.20a show the network and the main segments included in this study, as well as three zones of complexity marked with red dashed lines and labeled A-C. The N-S oriented segment I is the largest fault of the locality, and the one with the largest displacement. It consists of two hard-linked segments, where the northernmost is running out of the ledge towards the north, and the southern one ends where it abuts against the W-trending fault towards the south. Complex zone C is found towards the southern end of segment I, while complex zone B is situated in the area where the two segments that comprise segment I is linked. Segment II is oriented perpendicular to segment I, and the two segments are linked by another fracture segment. Segment II is approximately 125 cm long, and does not show any displacement. In the western end the segment splays into two branches that curve up towards segment I. Complex zone A is situated in the eastern end of segment II, and constitutes the area of which segment II is linked to both segment III and IV, and the last segment which runs out of the studied area. Segment III and IV are both parallel to segment I, and run out from complex zone A.

The strongest and widest redox fronts on this location are found along segment I. A couple of strong fronts can be traced along the whole fault, while some weaker, discontinuous fronts can be observed in the southern end. The redox fronts digitized along with the fault/fracture network in Figure 5.20. The fronts appear to localize at one point in the southern end (Fig. 5.20a), and diverge along the fault towards the north. Around the linkage zone/complex zone B on segment I the fronts are widening. The redox fronts also appear to get wider as the fault approach segment II, and one of them can be traced as it curves and follow segment II eastwards. The fronts stop abruptly halfway along segment II. Further east, a very clear front can be traced out from complex zone A along both segment III and segment IV. These fronts are only stretching a couple of cm from the fracture.

The accompanying branch intensity map and connecting node frequency map of the location are presented in figure 5.20b and 5.20c. Both maps show higher values in the complex zones, as well as in the areas where segment I is linked to segment II. The area with the highest branch intensity is found in complex zone A, where segment II, III and IV diverge from the same relay

zone, while the area of highest connecting node frequency is found in complex zone C, south of the southernmost observed redox front.

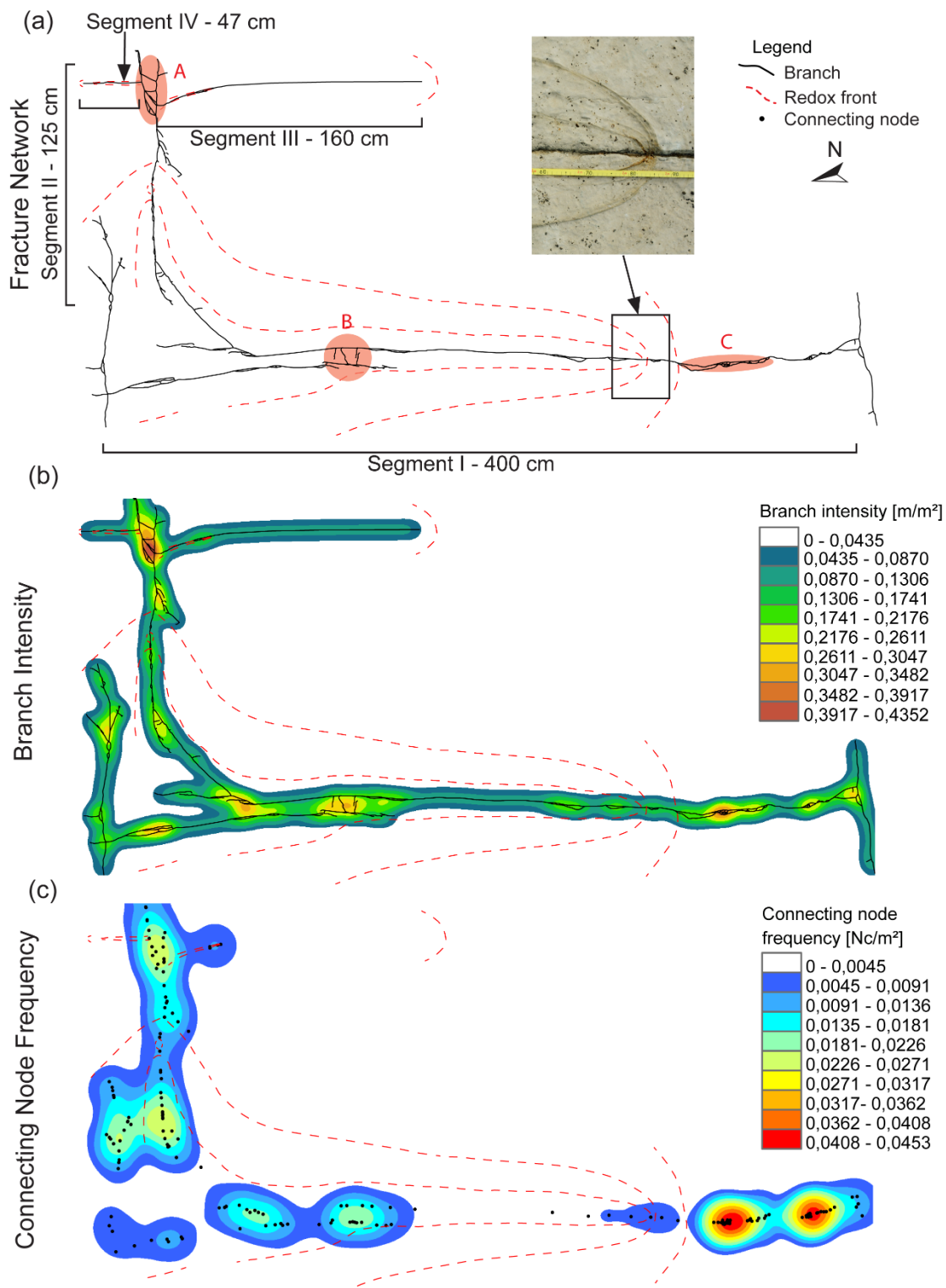


Figure 5. 21. (a) Digitized map of the fracture network at locality V6, with the oxidation fronts showed as red dashed lines and the more complex zones highlighted with a light red color. Photo of stagnated redox front included. (b) Branch intensity map indicating higher density in complex zones. (c) Connecting node frequency map of the locality, shows that zones with high branch intensity generally tend to coincide with high connecting node frequency.

5.6 Redox-type localities at Marsalforn (Gozo)

5.6.1 Local structure and stratigraphy of the Marsalforn study area

Since one of the localities are situated right west of Marsalforn, Gozo (Fig.5.1c), a short introduction to the structure and stratigraphy of this area is provided as context. Similar to the main island of Malta, Gozo is also characterized by ENE-WSW striking normal faults. However, the northwestern part of the island stands out, as the normal faults in this area is replaced by arrays of strike-slip faults that are also related to the Pantelleria rifting event (Kim et al., 2003). The faults occur in the LGLM in the study area (Fig. 5.2), which outcrops as a yellow to orange, massive wackestone, packed with foraminifers and bivalves. The thickness of the LGLM does not exceed 40 m on Gozo, and is capped by a hardground followed by the phosphoritic conglomerate layer (LGLM-C1) (Pedley et al., 1976).

The LGLM from Gozo show a porosity of 7.8% from analysis using optical microscopy, which is higher than the estimated porosity in the MGLM from Malta (4.1%).

5.6.2 Redox locality V10, Gozo

Locality V10 is situated at Gozo, by the salt pans at Reqqa point, west of the town of Marsalforn (Fig. 5.1c). The locality consists of a 2 m long fracture set that comprise a small part of a much longer fracture system that display evidence for dextral strike-parallel displacement in form of a series of small (cm-dm scale) pull-apart structures that appear along the fracture set. A bleached and an enriched zone occur around most of these (Fig. 5.21). A digitized map of the part of the fault/fracture network studied as locality V10 is presented in Figure 5.22a, where a light red color highlights more complex zones. The reduction fronts and oxidation fronts are showed as green and red dashed lines. The network is divided into four main segments labeled segment I-IV, where segment I is about 40 cm long and splays into two new segments in complex zone A. One of them constitutes the NE-trending segment II, while the other (unlabeled) splays into two additional fractures off the ridge of which the fracture network is situated. Segment II is linked to segment III, which is approximately 70 cm long, and oriented E-W. Segment III is connected to segment IV through complex zone B. Two additional fractures breach out from complex zone B, oriented the same way as the unlabeled segment breaching out form complex zone A.

The oxidized front can be traced almost continuously along segment I, III and IV, but is very sparsely present along segment II. The bleached fronts are more discontinuous, and are typically localized around the pull-aparts. The bleached front is also most present along segment I, III

and IV, and almost absent along segment II. A branch intensity map for the location is presented in Figure 5.22b, which can be compared to the density map of the connecting node frequency in Figure 5.22c. The branch intensity present very similar values along the whole fracture network on the locality, but an increase can be observed in the areas of complexity. These areas can also be recognized in the connecting node frequency map as areas with higher connecting node frequency. The connecting node frequency varies along segment I, II and IV, and along segment III it is $>0.0075 N_c/m^2$ for most of the segment.

5.7 Summary of results

Fault or fracture networks were investigated at a total of nine localities, whereof eight is situated in the area of Ras ir Raheb on Malta and one outside Marsalforn, Gozo. Six of the localities, all located at Ras ir Raheb, are mound localities which show topographic changes along the fracture network. The remaining three are redox-type localities, showing zones of bleaching or oxidation along the fracture network.

The mound localities all include varying degrees of structural complexity along strike. The more complex parts of each locality usually coincide with mounds (topographic highs) along the fracture network, and zones of higher branch intensity, connecting node frequency and fracture intensity. Porosity estimations done by analysis through optical microscopy show that three out of the six mound localities have higher porosity in the host rock compared to the corresponding mound, while porosity estimations by analysis through BSE-SEM images show higher values in host compared to corresponding mound for five of the six localities. The three redox-type localities are more varied in respect to the mound localities. Locality V5 shows zones of oxidation that correlate to the displacement of the fault. The redox front is at its widest where the displacement is at its largest, and decrease with decreasing displacement. Locality V6 shows a fault and fracture network with low displacement, where the redox fronts follow the main segments and widens toward the intersection point. Locality V10, situated on Gozo, includes both bleached and oxidized fronts concentrated around pull-apart structures along the fracture network

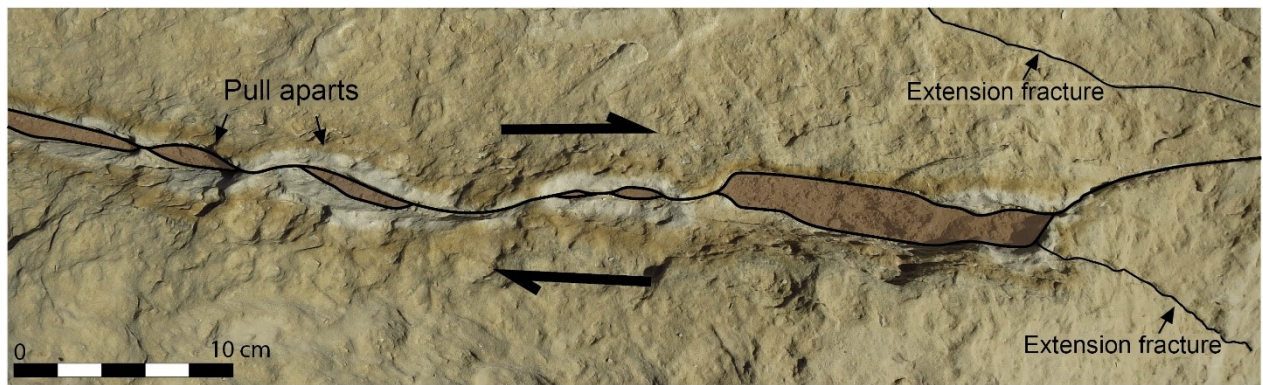


Figure 5.21. Close up of redox front at locality V10, where the depleted and enriched zones shows clearly. Extension fractures are marked with black lines, showing the dextral movement, and pull-aparts are highlighted with brown fill color.

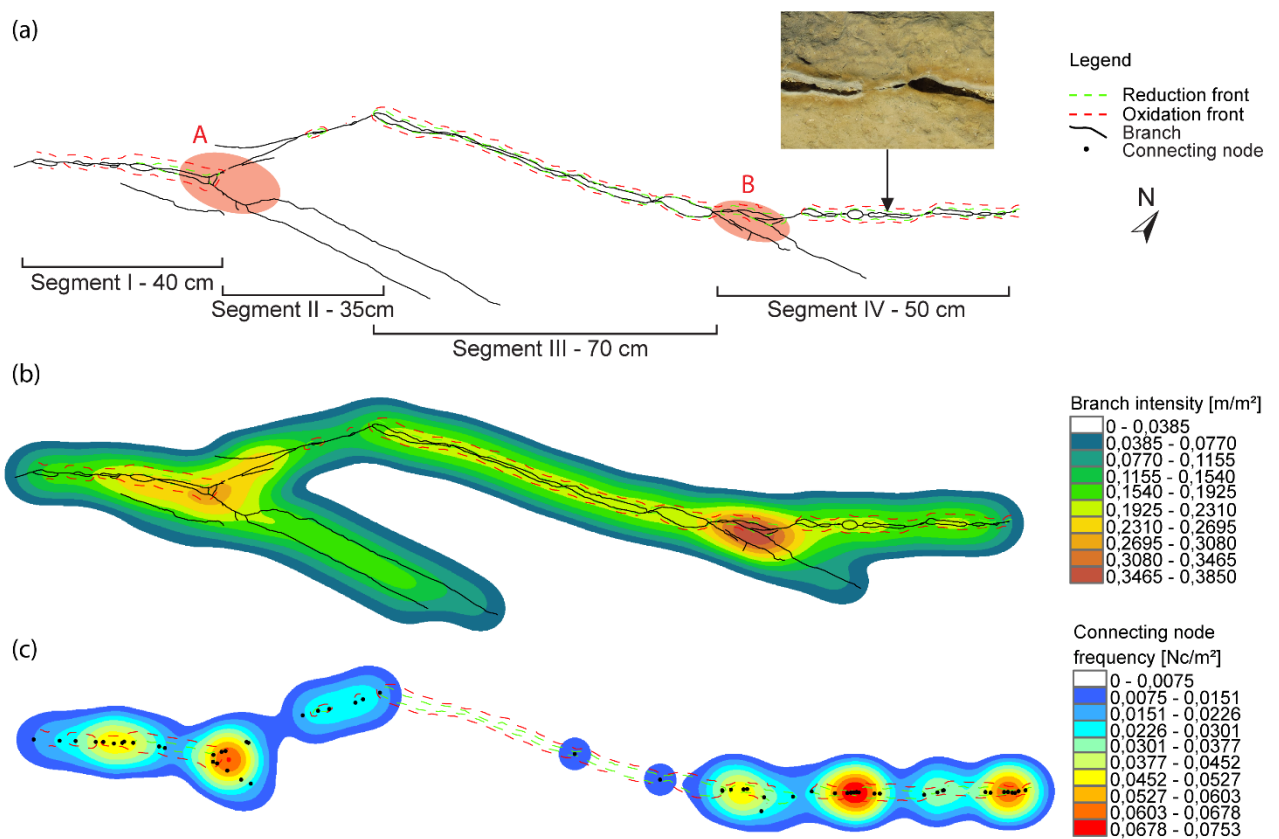


Figure 5.22. (a) Digitized map of the fracture network on locality V10, with the oxidation front showed as red dashed lines and the reduction front showed as green dashed lines. More complex zones are highlighted in light red. Field photo in right hand corner shows a close-up of pull-aparts. (b) The branch intensity map indicates higher branch intensity in the complex zones. (c) Connecting node frequency map of the locality, showing that there is a higher connecting node frequency in the complex zones.

6. DISCUSSION

In the foregoing chapters, data are presented to describe and quantify the relationship between structural complexities, connectivity and evidence of past fluid flow events (mounds and redox fronts). In this chapter, the results are interpreted and discussed in order to shed light on i) structural controls on fluid flow, ii) the drivers promoting fluid flow in structurally complex settings, and iii) the implications and applications of the presented research at a range of scales and settings.

6.1 What does the preferential location of mounds and redox fronts at structurally complex areas tell us?

The micro porosity of the MGLM are mainly found as primary intergranular and intragranular porosity through the intact foraminifer chambers. The porosity analysis carried out show a general trend of slightly lower porosity in the mounds compared to the corresponding host rock (Fig. 5.14). These porosity variations are interpreted to reflect the results of selective and localized cementation of the mounds, which was also the working hypothesis during data collection. Localized cementation can also explain the topographic relief of the mounds. The variation in porosity could also be due to local mechanical compaction; however, no other indicators supporting this hypothesis are observed, and it is unclear why mechanical compaction would preferentially localize around fractures. This hypothesis is therefore found unlikely and disregarded. Having established that differential cementation is the likely cause of the lower-porous mounds, a question arising is “what causes this preferential location of the cementation to take place?”

The results presented in Chapter 5 imply a strong relationship between mound localization and structural complexity. The six mound-type localities all show positive correlation, to various degrees, between the location of the mounds (topographic highs), and parameters quantifying structural complexity, like branch and fracture intensity, and connecting node frequency along the studied fracture networks. Not all zones can show a correlation that encompasses all the parameters at the same time, but the main trend is indicating a relationship between them. For example, three of the complex zones (zones C, D and E in Fig. 5.8a) at locality V1 show a positive correlation between all parameters, while the latter two (zones A and B in Fig. 5.8a) correlate through branch and fracture intensity and connecting node frequency, but does not show a deflection in the topography profile (Fig. 5.8a). Similarly, two of the complex zones at locality V7 (zones B and C Fig. 5.11a) correlates between all parameters, while zone A (Fig. 5.11a) is not observed in the topography profile (Fig. 5.11f), and zone D (Fig. 5.11a) is not

observed in neither the topography profile nor the fracture intensity profile (Fig. 5.11d and f). The bushes that were growing in some of the larger mounds could be responsible for the low values of branch and fracture intensity and connecting node frequency within the larger complex zones, due to the “holes” they leave in the network. An example can be seen within complex zone B in the branch density and connecting node frequency maps of locality V7 (Fig. 5.11), where this hole appears as a white area. As the connecting node frequency graph crosses this hole, it reflects a low at the crossing point. High branch intensity and fracture intensity means that the network is complex, while high connecting node frequency indicates that the branches are connected, -providing a highly connected network (Morley and Nixon, 2016). The mounds, illustrated by the highs in the topography profiles, indicate that they are more resistant to erosion than the host rock. This is in good agreement with them being subject to locally more cementation than the surrounding rock of less structural complexity. In sum, therefore, the dominating trend is that zones of structural complexity, and in particular those most complex, coincide with topographic highs.

At the three redox-type localities, a positive correlation is observed and documented between the degree of structural complexity and the spatial extent of the redox fronts. Patterns of paleo-fluid flow can be inferred from the extent of the redox fronts documented on each locality in relation to the local structures. The occurrence of redox fronts, as a result of migration of rare earth elements to the front of an oxidizing flow of water (Akagawa et al., 2006), has been investigated with different purposes and within different rock types by a handful of researchers. Akagawa et al. (2006) carried out studies in crystalline rock, while Yoshida et al. (2008) and Oyama et al. (2008) investigated the redox front in siliciclastic and pyroclastic rocks, respectively, as a safety assessment comprehending radioactive waste disposal. Ogata et al. (2014) did a study on the relationship between structural complexity and fluid flow directly through redox fronts in outcrops in the sandstones in Utah, while Missenard et al. (2014) did similar investigations in carbonate rocks at various locations around Malta and Gozo. All studies mentioned above found that there is often an observable correlation between structural complexity and the redox fronts. This is in agreement with the findings from the redox-type localities in this study, as it offers direct observational evidence for a relationship between structural complexity and the extent of the redox fronts. For example, locality V5 shows that the redox front is at its widest where the displacement of the fault is at the largest, and the redox front narrows as the displacement decreases (Fig. 5.18). Similar observations are made along the segments on locality V6, where the width of the redox fronts increase with increasing

structural complexity (Fig. 5.20). Redox fronts are seen to widen around relay zones, such as along the N-S trending segments on locality V6 (Fig 5.20). The curving and transfer of the redox front, from the N-S trending fault (segment I) to the E-W trending fracture segment (segment II), suggests that the two are connected, and the increased width of the redox front along the intersection points to increased fluid flow (Fig. 5.20).

In sum, both the redox fronts and the mounds show a preferential localization to areas of high structural complexity. The combination of observations from mound and redox localities are evidence that rock-fluid interactive processes (cementation, reduction, oxidation) appear to be focused to locations where structural complexity is high. Having made that observation, a key question arising is: “how and why do structurally complex zones form loci for fluid-rock interaction?”. To answer this, I first discuss the origin of structurally complex zones, before converging on the question of why they preferentially localize fluid-rock interactive processes.

6.2 How do the structurally complex zones form, and what is their role in controlling the localization of flow and fluid-rock interaction?

Normal fault zones are generally comprised of several fault segments which interact at different levels, where they jog, bifurcate and/or link, creating longer, continuous faults with irregularities like fault bends and intersections along the fault plane (e.g. Walsh et al., 2003, Rotevatn and Bastesen, 2014). Such irregularities may cause stress concentrations in local areas which further induce small scale fracturing along the respective fault plane, resulting in zones of higher complexity (Segall and Pollard, 1980, Maerten et al., 2002). An example could be linkage zones, where two fault segments interact and finally breach. The structural complexity will increase as the linkage evolves and what was initially a relay ramp becomes a breached relay (Peacock and Sanderson, 1994, Trudgill and Cartwright, 1994). High fracture intensity and fractures showing various orientations are expected. Perturbations of the stress field along faults during fault growth which affects the development of joints in proximity to the fault, making joints grow at high angles to the faults (Tamagawa and Pollard, 2008). The perturbation of the stress field is at its maxima close to the tip-line of faults, making this an area where secondary structures tend to initiate, creating higher structural complexity at fault tips (Barton and Zoback, 1994, Kattenhorn et al., 2000). Such structurally complex zones are well-known to act as fluid flow conduits (e.g. Berkowitz, 1995, Gartrell et al., 2004).

Fluids tend to localize and flow in and along faults, fractures, and structurally complex zones due to permeability contrasts between the structures and the matrix (Davatzes and Aydin, 2003). Open fractures encompass extraordinary permeability in contrast to the protolith, and a

structurally complex zone with high fracture intensity, various fracture orientation and high connectivity would hence favor fluid flow (e.g. Rotevatn and Bastesen, 2014). Stress perturbation and rotation of the stress field may also provide wider fracture apertures to increase permeability (Tamagawa and Pollard, 2008). Figure 6.1 illustrates some preferential pathways for fluid migration within a structurally complex area.

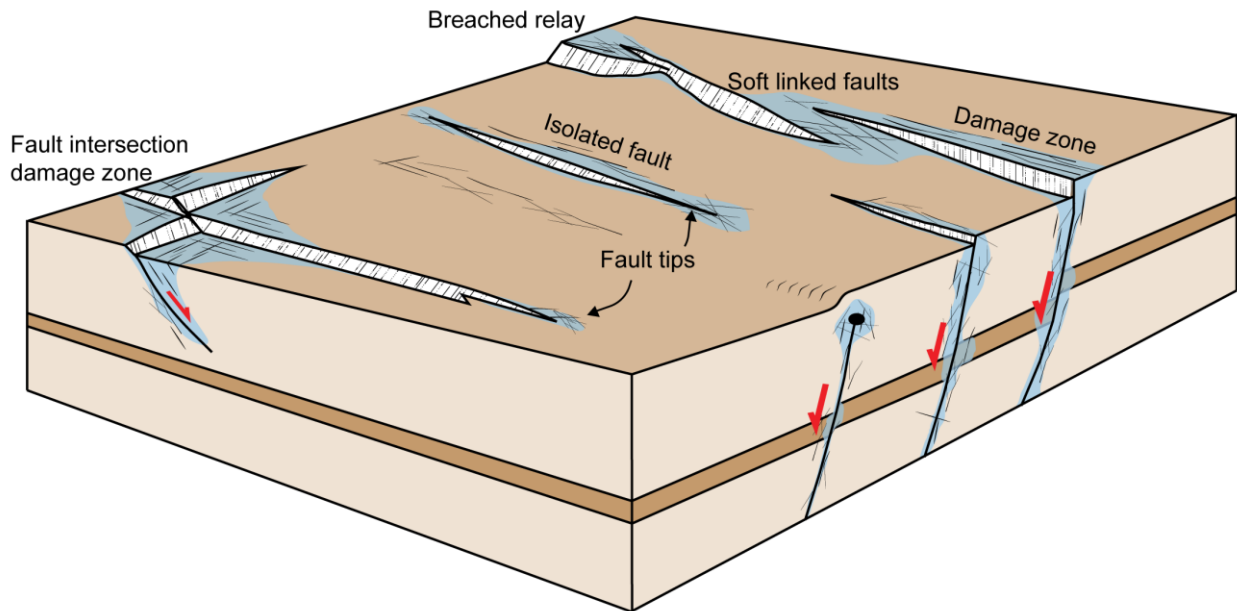


Figure 6.1. Schematic illustration of preferential fluid localization, illustrated by the blue color, along faults and fault intersections. After Peacock et al. (2016). The fluids may localize in fault damage zones and along fault planes, especially in more complex areas, like linkage points, fault tips and fault intersections.

Briefly, we can differentiate between two types of fluid flow conduits along active faults. The first one being conduits along the fault plane due to dilation associated with slip, and the second type being through secondary structures near fault tips etc. (Martel, 1990, Barton et al., 1995, Martel and Boger, 1998, Kattenhorn et al., 2000, Davatzes and Aydin, 2003, Tamagawa and Pollard, 2008). These secondary structures have been found to be an especially important passage for fluid flow in tight carbonate rocks with low matrix permeability (Tamagawa and Pollard, 2008, Casini et al., 2011, Rotevatn and Bastesen, 2014). The complex zones documented at the localities in this study show a high branch and fracture intensity, and serves as examples of such fluid migration pathways (e.g. complex zone B on locality V2, Fig.5.9, and complex zone B on locality V7, Fig. 5.11). As pointed out in Chapter 5, the concurrent of higher branch intensity and higher connecting node frequency means these zones have a higher connectivity. Vegetation in form of small bushes at some of the larger mounds indicate presence of nutrients and water, which may have its origin in the fracture network, supporting the hypothesis of these zones being loci for fluid flow. Figure 6.2, presenting a photo from locality

V4, shows how water localize along the fracture and serves as another example of how fluids localize in the vicinity of faults and fractures.

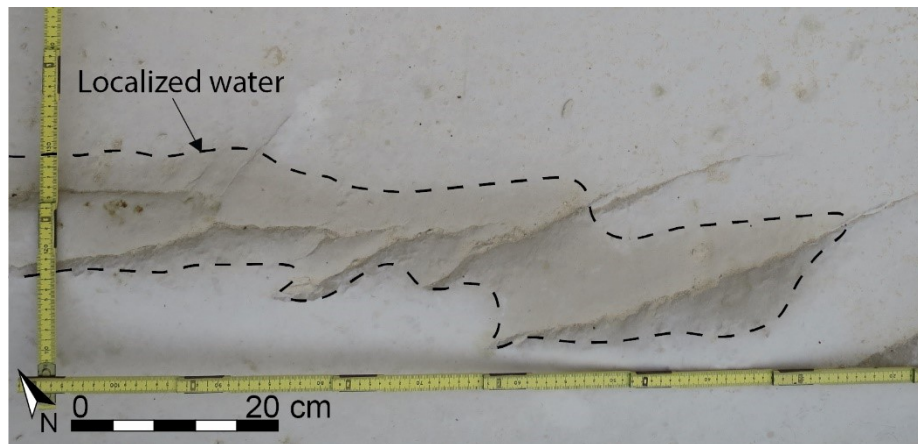


Figure 6.2. The figure shows some of the fractures at locality V4. The photo is taken after a night with heavy rain, and the darker area around the fractures (highlighted by the dashed line) shows how the water is localizing in the vicinity of the fractures.

However, one of the most important indicators of the localization of fluids in the complex zones presented throughout this thesis is the differential cementation observed between mounds and host rock. As stated, the mounds show slightly lower porosity than the host rock, interpreted to be a result of increased fluid flow as the mounds coincide with structurally complex zones. A question arising from this is “how does the increased fluid-rock interaction cause the increased cementation?”. It leaves two possible explanations; i) the increased cementation is solely a result of increased flow through the structural complex zone relative to the host rock, ii) the increased cementation is a result of a combination of increased flow and larger reactive surface area in the structural complex zone relative to the host rock.

It is already mentioned that increased fluid flow could cause more cementation, as more mineralizing fluids can pass through the rock (e.g. Flügel, 2010). However, the increased number of fractures in the complex zones also provide a larger reactive surface area for the fluid-rock interactions. The accessibility of surface area can give higher fluid-rock interaction rates, as the fluid get access to a larger area (Lüttge et al., 1999, Flügel, 2010). With the available information it is not possible to exclude this as a possible factor for enhancing the cementation. The preferred interpretation in this study is that both of these factors (increased flow and increased reactive surfaces area) contributed to cause localized cementation (and therefore mound formation) in areas of structural complexity.

6.3 An additional aspect of preferential flow localization in the redox-type localities

At locality V5 many more, and stronger redox fronts are observed in the footwall of the fault compared to the hanging wall (Fig. 6.3). At the widest, the outermost redox front in the footwall is located approximately 100 cm from the fault plane. It is a weak and discontinuous front, like the redox fronts in the hanging wall. A cluster of very closely spaced redox fronts is occupying a zone reaching from the fault plane and about 50 cm into the footwall at the widest. The zone shows some strong redox fronts with several weaker fronts in between. In the hanging wall the fronts are very weak and discontinuous, the outermost observed approximately 50 cm from the fault at the widest. Only a couple of other, discontinuous redox fronts were observed in the hanging wall, both much weaker than the ones in the footwall. Three hypotheses are considered to explain the preferential location of redox fronts to the footwall.

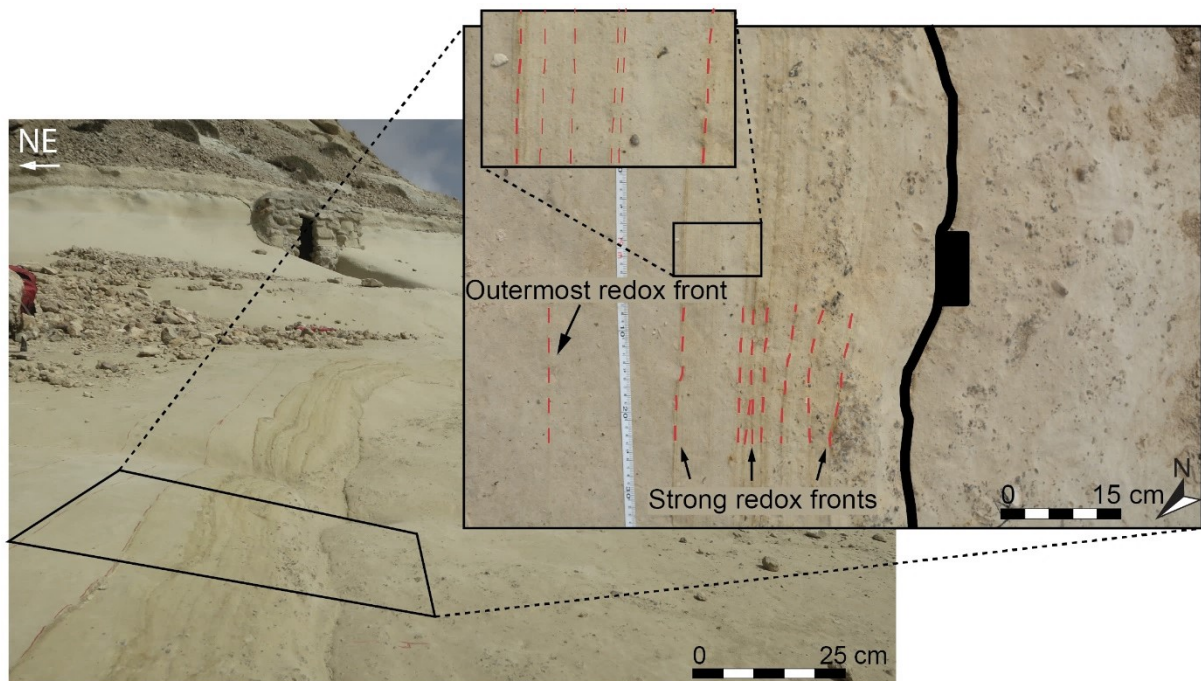


Figure 6.3. Photo of the redox fronts in relation to the fault on locality V5. The vast majority of the redox fronts are located within a range of 50 cm from the fault with various strength. The stronger fronts are marked by red dashed lines in the main photo. The enlarged area shows several weaker redox fronts between two stronger ones. No redox fronts can be observed in the hanging wall of this photo.

Firstly, investigations of fluid flow along faults, e.g. Davatzes (2005), Johansen (2005), Eichhubl et al.(2009), reveal that fluids might migrate vertically along a fault plane with conduit properties before intruding a permeable layer or bed outside the fault plane, in the hanging wall, footwall, or both, depending on the lithology and its' characteristics (Fig. 6.4a). This could explain why the redox fronts are mainly found in the footwall along the fault at locality V5. But as the lithology in this case is the same on both sides, the variations would have to be very local, at a microscopic level, if one side of the fault is more prone to fluid flow than the other. No

observations to support this have been made in this study, and therefore this hypothesis is considered unlikely. A second hypothesis to be considered is based upon the source of the fluid (Fig. 6.4b). In a pictured situation where the fluids approach the fault from the NW (the footwall side of the fault), and the fault acts as a barrier, the fluids would pond and preferentially accumulate/flow at the footwall side of the fault. However, no other observations indicate that the fault is sealing, e.g. formation of impermeable fault rocks or cementation along the fault plane, and the hypothesis is thus also considered unlikely. A third hypothesis is that these different appearances of the redox fronts on each side of the fault are due to variations in deformation through the fault zone (Fig. 6.4c).

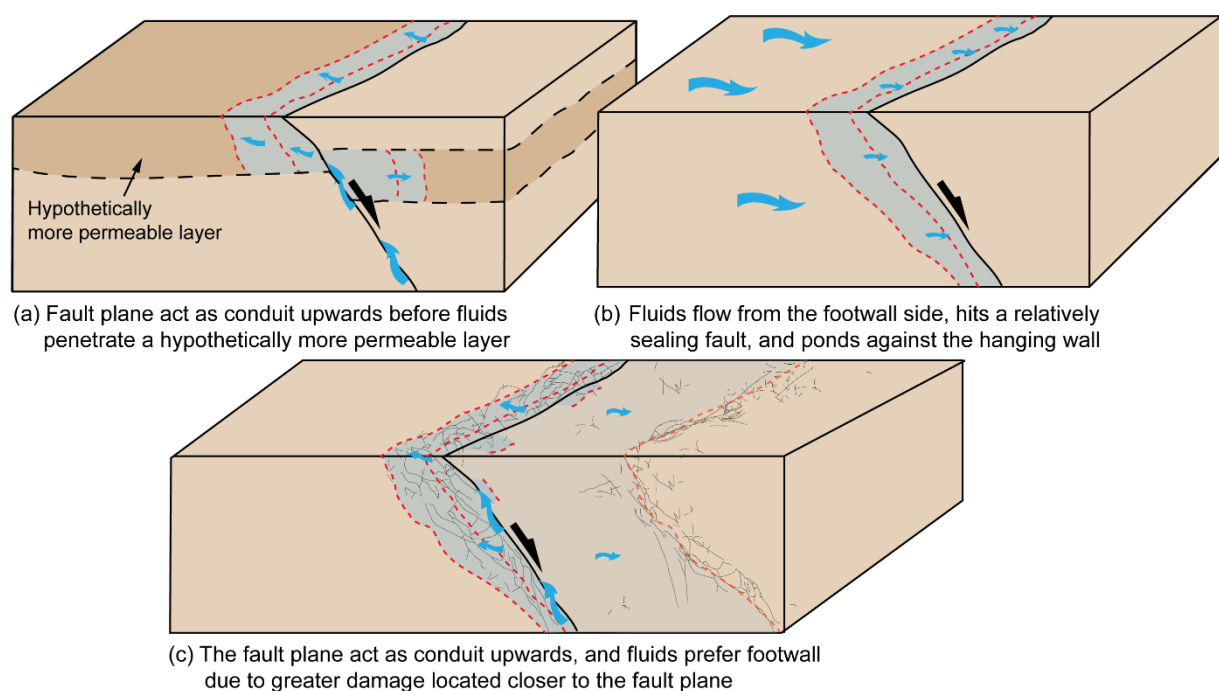


Figure 6.4. Schematic illustrations of three competing hypothesis to explain flow patterns forming the redox fronts at locality V5. **(a)** The fluids migrate upwards along the fault plane, which act as a conduit, before they intrude a more permeable layer in the fault blocks. **(b)** The fluids approach a relatively sealing fault from the footwall side, where they pond against the fault and accumulate in the footwall. **(c)** The fluids migrate upwards along the fault plane which act as a conduit. Due to high deformation close to the fault in the footwall, the fluids prefer the footwall block. In the hanging wall the deformation is located further away from the fault plane.

The deformation might be higher close to the fault in the footwall block, while in the hanging wall the deformation is located more distant from the fault plane, causing fluid flow, and hence oxidation, to occur further away from the fault. In the case of locality V5, the deformation could then have been situated in a part of the hanging wall outside of the outcropping area (not exposed/removed by erosion). Such varieties in the deformation in relation to the fault have been observed in plaster modeling experiments carried out by Blækkan (2016) (Fig. 6.5). In general, her experiments show that deformation in the footwall mainly occur in a relatively

narrow zone close to the fault plane, while the hanging wall deformation is localized further away from the fault plane. The results from the accompanying topological analysis show that the connectivity coincides with the deformation, and is generally higher in the immediate footwall than in the hanging wall throughout the extension phase. It further shows that the footwall damage zone is more narrow than the hanging wall damage zone and located close to the fault plane, while the deformation in the hanging wall is distributed over a wider area further away from the fault, leaving an un-deformed zone along the fault plane.

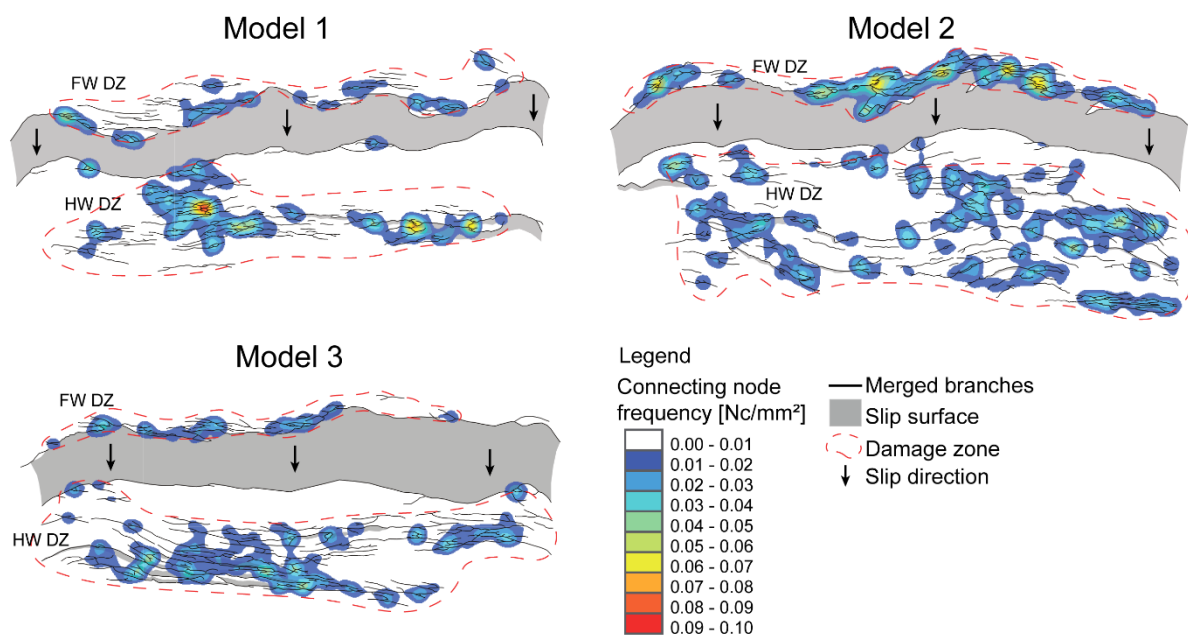


Figure 6.5. Contour plots of three different plaster modeling experiments carried out by Blækkan (2016), showing the connecting node frequency in the footwall and hanging wall of a fault in the final extensional stage. The figure shows a two-dimensional reproduction of a three-dimensional surface. The deformation and connecting node frequency are located in a narrow zone close to the slip surface in the footwall damage zone (FW DZ), while the hanging wall damage zone (HW DZ) shows more wide spread deformation located further away from the slip surface, leaving a narrow zone of undeformed rock along the fault plane. Modified from Blækkan (2016).

6.4 Why are structural controls on fluid flow important to understand?

A range of studies have demonstrated the importance of understanding structural controls on fluid flow in a range of different settings, and for a range of different applications (e.g. Kerrich, 1986, Curewitz and Karson, 1997, Aydin, 2000, Gartrell et al., 2004, Rowland and Sibson, 2004, Shipton et al., 2004, Yoshida et al., 2008, Verhaert et al., 2009, Micallé et al., 2011, Bense et al., 2013, Rotevatn and Bastesen, 2014, Davidson et al., 2016). As faults and fractures exert strong control on fluid flow, and may permit or prevent fluid migration, they may also control a series of processes in the earth's crust. Examples of some well-known processes and areas of application are:

- Geological hazards: e.g. earthquake localization and volcanic eruptions

- Economic applications: e.g. ore deposits and petroleum
- Environmental applications: e.g. CO₂ storage, nuclear waste disposal, and contaminant transport
- Public health/resource management: e.g. groundwater and geothermal energy

For example, Davidson et al. (2016) recently examined radon (²²²Rn) anomalies due to upward migration of fluids along fault zones in New Zealand, and found that the concentration of radon isotopes is generally higher near faults, indicating a positive correlation between structural complexity and fluid flow. As ²²²Rn got a half-life of only 3.85 days, it would not have the chance to move far without a fast-flowing fluid to carry it, making it highly independent on an evolved fracture network, and a great indicator of fluid flow and fault activity (Tanner, 1980, King et al., 1996, Katsanou et al., 2010). Similar results to the ones of Davidson et al. (2016), regarding radon concentrations, have previously been found in proximity to active faults several other places around the world, e.g. in India (Virk and Singh, 1993), California (King et al., 1996), Egypt (Moussa and El Arabi, 2003), and Japan (Igarashi et al., 1995). Rowland and Sibson (2004) and Curewitz and Karson (1997) identify the relationship between structural complex zones and hydrothermal activity in fault step overs and fault arrays, as concentrations of geothermal zones appear to coincide with increased vertical flow in the complex zones, and the position of hot springs coincide with structurally more complex zones as fault interaction areas. Gartrell et al. (2004) examined fault intersections as hydrocarbon leakage zones through three-dimensional numerical modeling, and found that zones of high dilation were generated close to fault intersections, leading to high permeable zones with a concentration of open fractures ideal for fluid migration. As such, understanding the locations of structural complexity may be of economic importance in terms of understanding the risk for hydrocarbon leakage, or the location of economically significant ore deposits (Beukes et al., 2013, Rotevatn and Fossen, 2011). Ore deposits was early mentioned in the literature in relation to structural complexity (Newhouse, 1942, McKinstry, 1948). Since then they have been the subject of several studies (Sibson, 1996, Zhang et al., 2003, Marchev et al., 2005, Xiao-Shuang et al., 2005). Sibson (1996) investigated self-generation of structural permeability by fluid migration, and its role comprehending the volume of fluid flow required to form hydrothermal ore deposits. He found that fluid overpressures in the crust hold great control on faulting and mineralization, and that mineralizing environments can be understood through varying seismic style in different tectonic settings. It is widely agreed that faults and fractures serve as an efficient migration pathway for hydrocarbons, e.g. Møller-Pedersen and Koestler (1997), Aydin (2000), Nelson (2001) and

Harris et al. (2003). Their high influence often make the faults and fractures determine the hydrocarbon distribution within a field, making knowledge about them highly valuable for the hydrocarbon industry (Harris et al., 2003). Carbonate rocks, in which this project has been carried out, serve as a prominent reservoir rock around the world, and account for 50-60% of oil and gas reserves according to Mazzullo (2004) and Schlumberger (2016). As carbonates usually are strongly heterogeneous and can show high variations in porosity and permeability within a small area, they can be difficult to characterize, and structurally complex zones may be a crucial feature for the recovery factor of a reservoir (Aydin, 2000, Sun and Sloan, 2003, Casini et al., 2011). However, the areas of the faults and damage zones' geometry and architecture that contribute the most to fluid flow often fall beneath the resolution of seismic imaging and/or exceed the lateral extent of wellbore data (Walsh et al., 1998, Rotevatn et al., 2009a). That is where outcrop analogues, such as presented herein, can serve as important sources of information which can be incorporated to subsurface reservoirs.

An improved understanding of fluid flow and structural complexity can also help predicting geo-hazards such as earthquakes and volcanic eruptions. Fault intersections have become recognized to act as locations for earthquake rupture, as the structural complexity and higher fracture density promotes fluid flow, increase fluid pressure, and provide localized weak areas (Sibson, 1996, Talwani, 1999, Kim et al., 2004). Increased flow of fluids can lead to high rates of outgassing from the earth, like variations in radon concentrations in soil-gas or groundwater. High radon concentrations are very often associated with active faults, and abrupt changes in radon concentration have been documented to appear as precursors of earthquakes, studied by e.g. King (1986), Moussa and El Arabi (2003), and Katsanou et al. (2010). Finzi and Langer (2012) carried out earthquake simulations, and propose that weakness in fault step-overs due to accumulated damage may empower cascading earthquakes. Earthquakes are also known to serve as a trigger for landslides and volcanic eruptions, and Carracedo (1994) found that rift zones play a significant role in eruptions and growth of the volcanoes in the Canary Islands. The ability to predict earthquakes and volcanic eruptions is a great safety asset, but also contains economic value since predictions increase the possibility of preventive actions to save e.g. buildings and infrastructure (Keilis-Borok, 2002, Halvorson and Parker Hamilton, 2010).

Faults, fractures, and structurally complex zones in the shallow crust also strongly applies to environmental issues, like storage of CO₂, radioactive waste deposal contaminant transport, and flow patterns of groundwater (Yoshida et al., 2008, Dockrill and Shipton, 2010, Bense et al., 2013). Mechanisms associated with deeper situated (below groundwater table), high-level

radioactive waste, e.g. groundwater radiolysis, can form redox fronts around the zones with high-level radioactive waste (Akagawa et al., 2006, Yoshida et al., 2006, Yoshida et al., 2008). This makes the redox fronts, and hence the fluid flow and structural complexity, important for the understanding of radioactive waste migration. Another fluid stored in underground repositories is CO₂, which also are highly dependent on structures acting as conduits or barriers. Shipton et al. (2004) examined evidence of CO₂ migration along normal faults, and found that geysers and hydrocarbon seep were localizing along the faults. Their observations are supported by Dockrill and Shipton (2010) who investigated the structural control on CO₂ leakage from a natural storage site, and did field observations of bleaching and mineralization indicating that the paleo-fluid flow followed the fracture network in the damage zone of the faults. The results of Shipton et al. (2004) and Dockrill and Shipton (2010) show the importance of knowledge about the structure characteristics to prevent CO₂ seepage into the atmosphere. Structural complexity exerts strong controls on groundwater flow direction and flow obstruction, studied by e.g. Bense et al. (2003), Bense and Person (2006), Mayer et al. (2007), and Burbey (2008). The results of Bense and Persons' (2006) study show that faults can form a preferential, vertical fluid migration pathway between aquifers situated several hundred meters apart when the permeability of the fault is strongly anisotropic. Simultaneously, they found that diverging hydraulic head gradients across the fault occurred, which suggest that the fault still act as a barrier to lateral flow. Such findings are important in relation spreading of contaminated groundwater, and other kinds of contamination.

The various fields and processes affected by fluid flow which have been portrayed through this section are only some of many more, showing the great value of understanding how fluid flow behave in the subsurface, and the possible implications of in this thesis. Structural complexity is recognized and proven to exert great controls on the fluid flow properties and fluid-rock interaction, as portrayed through the studies described above, and within this project.

7. FINAL CONCLUSIONS AND FURTHER WORK

7.1 Conclusions

The main aims of this project have been to improve the understanding of structurally controlled fluid flow, and to constrain and quantify the relationship between fluid flow and structural complexity. These aims were reached through field-based investigations of two different locality types, documenting the geometry and topology of fracture networks along small scale faults and fault damage zones, documenting the evidence of paleo-fluid flow in the form of diagenetically altered zones, and determining porosity variations between host rocks and elevated zones with higher structural complexity. From the results and discussion presented herein, the following conclusions are drawn:

- Porosity estimations show a general trend of lower porosity (0.3-6% difference) in mounds compared to host rock, concluded to be a result of differential cementation and hence an indicator of a preferential fluid flow pathway.
- The results following documentation and topological analyses show clear evidence of structurally complex zones acting as preferred fluid flow pathways. This have been documented and quantified through the following:
 1. At mound-type localities, the structurally complex zones are documented to coincide spatially with structurally complex zones characterized by increased branch intensity, higher connectivity, and topographic highs in form of cemented mounds that represent evidence for localized paleo-fluid flow.
 2. At redox-type localities, the structurally complex zones coincide with more spatially extensive redox fronts, proving increased, localized paleo-fluid flow.

Through these findings this study provides a quantification of the relationship between structural complexity and fluid flow, documenting and confirming the role of complex zones as loci for fluid flow and fluid-rock interaction in the subsurface. The findings have great implications for understanding the fundamentals of the relationship between structural complexity and fluid flow, as such a quantification has never been done before.

Even though this study have been carried out at a relatively small scale (meter size), it is hypothesized and considered likely that the results can be incorporated to a range of different scales, in accordance with earlier documentation within the literature. As the geometry and architecture of small-scale fracture networks contributing to fluid flow often fall beneath seismic resolution, the prediction of subsurface flow is very complicated. In such situations, it is highly valuable with outcrop analogues and field-based documentation as presented herein

to help generate as reliable predictions as possible. Hence, quantification of the relationship between structural complexity and flow, such as that documented in this study, has the potential to bring about improvements in the prediction of fluid flow properties in the subsurface. For example, topological characterization of seismic-scale fault networks based on subsurface data, combined with similar data from analogue studies, may offer a more direct route to predict subsurface flow properties. As such, this can be utilized as a backdrop and framework for future work within a wide variety of fields (e.g. hydrocarbon investigations, groundwater management, geothermal systems, subsurface depositing, ore deposition), as presented within the discussion.

7.2 Suggestions for further work

This study offers direct documentation and quantification of the control structural complexity holds on fluid flow in the shallow crust. Building out from this, there are several outstanding questions and venues for future work. Some suggestions for further research are listed below:

- It would be interesting to do a more detailed thin section analysis from the mounds and host rocks, studying the random distribution of the differential cementation, estimating the actual amount of cementation and determine its origin and formation history to gain a better understanding of the fluid flow behavior and history.
- Numerical modeling to simulate fluid flow in structurally complex zones can be done to investigate the influence such zones would have within different host rocks (e.g. varying the porosity and permeability of the host rock).
- Perform laboratory flow experiments on large samples (meter size) containing complex fracture zones, and directly monitor fluid flow behavior in structurally complex zones in three dimensions would be an interesting next step, as the topological characterizations herein are based on the two-dimensional surface of the fracture networks.
- One could compile earlier studies which document fluid flow in relation to structural complexity, and perform topological characterization of these to expand the database regarding the relationship between topology and fluid flow. A more extensive database would make this relationship more predicative.

8. REFERENCES

- AKAGAWA, F., YOSHIDA, H., YOGO, S. & YAMOMOTO, K. 2006. Redox front formation in fractured crystalline rock: an analogue of matrix diffusion in an oxidizing front along water-conducting fractures. *Geochemistry: Exploration, Environment, Analysis*, 6, 49-56.
- ARGNANI, A. 1990. The Strait of Sicily rift zone: foreland deformation related to the evolution of a back-arc basin. *Journal of Geodynamics*, 12, 311-331.
- AYDIN, A. 2000. Fractures, faults, and hydrocarbon entrapment, migration and flow. *Marine and petroleum geology*, 17, 797-814.
- BARNETT, J. A., MORTIMER, J., RIPPON, J. H., WALSH, J. J. & WATTERSON, J. 1987. Displacement geometry in the volume containing a single normal fault. *AAPG Bulletin*, 71, 925-937.
- BARTON, C. A. & ZOBACK, M. D. 1994. Stress perturbations associated with active faults penetrated by boreholes: Possible evidence for near-complete stress drop and a new technique for stress magnitude measurement. *Journal of Geophysical Research: Solid Earth*, 99, 9373-9390.
- BARTON, C. A., ZOBACK, M. D. & MOOS, D. 1995. Fluid flow along potentially active faults in crystalline rock. *Geology*, 23, 683-686.
- BASTESEN, E. & BRAATHEN, A. 2010. Extensional faults in fine grained carbonates – analysis of fault core lithology and thickness–displacement relationships. *Journal of Structural Geology*, 32, 1609-1628.
- BASTESEN, E., BRAATHEN, A. & SKAR, T. 2013. Comparison of scaling relationships of extensional fault cores in tight carbonate and porous sandstone reservoirs. *Petroleum Geoscience*, 19, 385-398.
- BEN-AVRAHAM, Z., GINZBURG, A., MAKRIS, J. & EPELBAUM, L. 2002. Crustal structure of the Levant Basin, eastern Mediterranean. *Tectonophysics*, 346, 23-43.
- BEN-AVRAHAM, Z., NUR, A. & GIUSEPPE, C. 1987. Sedimentary basins within the Dead Sea and other rift zones Active transcurrent fault system along the north African passive margin. *Tectonophysics*, 141, 249-260.
- BENSE, V., VAN DEN BERG, E. & VAN BALEN, R. 2003. Deformation mechanisms and hydraulic properties of fault zones in unconsolidated sediments; the Roer Valley Rift System, The Netherlands. *Hydrogeology Journal*, 11, 319-332.
- BENSE, V. F., GLEESON, T., LOVELESS, S. E., BOUR, O. & SCIBEK, J. 2013. Fault zone hydrogeology. *Earth-Science Reviews*, 127, 171-192.
- BENSE, V. F. & PERSON, M. A. 2006. Faults as conduit-barrier systems to fluid flow in siliciclastic sedimentary aquifers. *Water Resources Research*, 42, W05421.
- BENSE, V. F. & VAN BALEN, R. 2004. The effect of fault relay and clay smearing on groundwater flow patterns in the Lower Rhine Embayment. *Basin Research*, 16, 397-411.
- BERKOWITZ, B. 1995. Analysis of fracture network connectivity using percolation theory. *Mathematical Geology*, 27, 467-483.
- BEUKES, N. J., GUTZMER, J. & MUKHOPADHYAY, J. 2013. The geology and genesis of high-grade hematite iron ore deposits. *Applied Earth Science: Transactions of the Institutions of Mining and Metallurgy: Section B*, 112, 18-25.
- BILLI, A., SALVINI, F. & STORTI, F. 2003. The damage zone-fault core transition in carbonate rocks: implications for fault growth, structure and permeability. *Journal of Structural Geology*, 25, 1779-1794.
- BLÆKKAN, I. 2016. *Evolution of normal faults and fault-related damage: insights from physical experiments*. MSc. Thesis, University of Bergen, unpublished, 86.
- BOCCALETTI, M., NICOLICH, R. & TORTORICI, L. 1984. Geological and Geodynamical Aspects on the Mediterranean The Calabrian Arc and the Ionian Sea in the dynamic evolution of the Central Mediterranean. *Marine Geology*, 55, 219-245.
- BONSON, C. G., CHILDS, C., WALSH, J. J., SCHÖPFER, M. P. J. & CARBONI, V. 2007. Geometric and kinematic controls on the internal structure of a large normal fault in massive limestones: the Maghlaq Fault, Malta. *Journal of Structural Geology*, 29, 336-354.

- BOUVIER, J., KAARS-SIJPESTEIJN, C., KLUESNER, D., ONYEJEKWE, C. & VAN DER PAL, R. 1989. Three-dimensional seismic interpretation and fault sealing investigations, Nun River Field, Nigeria. *AAPG Bulletin*, 73, 1397-1414.
- BURBEY, T. J. 2008. The influence of geologic structures on deformation due to ground water withdrawal. *Ground water*, 46, 202-211.
- CAINE, J. S., EVANS, J. P. & FORSTER, C. B. 1996. Fault zone architecture and permeability structure. *Geology (Boulder)*, 24, 1025-1028.
- CAINE, J. S. & FORSTER, C. B. 1999. Fault zone architecture and fluid flow: Insights from field data and numerical modeling. *Geophysical Monograph*, 113, 101-127.
- CARRACEDO, J. 1994. The Canary Islands: an example of structural control on the growth of large oceanic-island volcanoes. *Journal of Volcanology and Geothermal Research*, 60, 225-241.
- CARTWRIGHT, J. A., TRUDGILL, B. D. & MANSFIELD, C. S. 1995. Fault growth by segment linkage: an explanation for scatter in maximum displacement and trace length data from the Canyonlands Grabens of SE Utah. *Journal of Structural Geology*, 17, 1319-1326.
- CASINI, G., GILLESPIE, P., VERGÉS, J., ROMAIRE, I., FERNÁNDEZ, N., CASCIELLO, E., SAURA, E., MEHL, C., HOMKE, S. & EMBRY, J.-C. 2011. Sub-seismic fractures in foreland fold and thrust belts: insight from the Lurestan Province, Zagros Mountains, Iran. *Petroleum Geoscience*, 17, 263-282.
- CATALANO, S., DE GUIDI, G., LANZAFAME, G., MONACO, C. & TORTORICI, L. 2009. Late Quaternary deformation on the island on Pantelleria: New constraints for the recent tectonic evolution of the Sicily Channel Rift (southern Italy). *Journal of Geodynamics*, 48, 75-82.
- CAVAZZA, W. & WEZEL, F. C. 2003. The Mediterranean region-a geological primer. *Episodes*, 26, 160-168.
- CHESTER, F. M. & LOGAN, J. M. 1987. Composite planar fabric of gouge from the Punchbowl Fault, California. *Journal of Structural Geology*, 9, 621-634.
- CHILDS, C., WALSH, J. J. & WATTERSON, J. 1997. Complexity in fault zone structure and implications for fault seal prediction. *Norwegian Petroleum Society Special Publications*, Volume 7, 61-72.
- CHILDS, C., WATTERSON, J. & WALSH, J. 1995. Fault overlap zones within developing normal fault systems. *Journal of the Geological Society*, 152, 535-549.
- CHOI, J.-H., EDWARDS, P., KO, K. & KIM, Y.-S. 2016. Definition and classification of fault damage zones: A review and a new methodological approach. *Earth-Science Reviews*, 152, 70-87.
- CIVILE, D., LODOLO, E., ACCETTELLA, D., GELETTI, R., BEN-AVRAHAM, Z., DEPONTE, M., FACCHIN, L., RAMELLA, R. & ROMEO, R. 2010. The Pantelleria graben (Sicily Channel, Central Mediterranean): an example of intraplate 'passive' rift. *Tectonophysics*, 490, 173-183.
- COWIE, P. A. & SCHOLZ, C. H. 1992a. Displacement-length scaling relationship for faults: data synthesis and discussion. *Journal of Structural Geology*, 14, 1149-1156.
- COWIE, P. A. & SCHOLZ, C. H. 1992b. Growth of faults by accumulation of seismic slip. *Journal of Geophysical Research: Solid Earth*, 97, 11085-11095.
- COWIE, P. A. & SCHOLZ, C. H. 1992c. Physical explanation for the displacement-length relationship of faults using a post-yield fracture mechanics model. *Journal of Structural Geology*, 14, 1133-1148.
- COWIE, P. A. & SHIPTON, Z. K. 1998. Fault tip displacement gradients and process zone dimensions. *Journal of Structural Geology*, 20, 983-997.
- CRIDER, J. G. & PEACOCK, D. C. 2004. Initiation of brittle faults in the upper crust: a review of field observations. *Journal of Structural Geology*, 26, 691-707.
- CRUIKSHANK, K. M., ZHAO, G. & JOHNSON, A. M. 1991. Analysis of minor fractures associated with joints and faulted joints. *Journal of Structural Geology*, 13, 865-886.
- CUREWITZ, D. & KARSON, J. A. 1997. Structural settings of hydrothermal outflow: Fracture permeability maintained by fault propagation and interaction. *Journal of Volcanology and Geothermal Research*, 79, 149-168.
- DART, C., BOSENCE, D. & MCCLAY, K. 1993. Stratigraphy and structure of the Maltese graben system. *Journal of the Geological Society of London*, 150, 1153-1166.

- DAVATZES, N. C. & AYDIN, A. 2003. Overprinting faulting mechanisms in high porosity sandstones of SE Utah. *Journal of Structural Geology*, 25, 1795-1813.
- DAVATZES, N. C., EICHHUBL, P. & AYDIN, A. 2005. Structural evolution of fault zones in sandstone by multiple deformation mechanisms: Moab fault, southeast Utah. *Geological Society of America Bulletin*, 117, 135-148.
- DAVIDSON, J. R. J., FAIRLEY, J., NICOL, A., GRAVLEY, D. & RING, U. 2016. The origin of radon anomalies along normal faults in an active rift and geothermal area. *Geosphere*, 12, 1656-1669.
- DI BUCCI, D., BURRATO, P., VANNOLI, P. & VALENSISE, G. 2010. Tectonic evidence for the ongoing Africa-Eurasia convergence in central Mediterranean foreland areas: A journey among long-lived shear zones, large earthquakes, and elusive fault motions. *Journal of Geophysical Research: Solid Earth*, 115, B12404.
- DOCKRILL, B. & SHIPTON, Z. K. 2010. Structural controls on leakage from a natural CO₂ geologic storage site: Central Utah, USA. *Journal of Structural Geology*, 32, 1768-1782.
- DUNHAM, R. J. 1962. Classification of carbonate rocks according to depositional textures, Classification of carbonate rocks. *AAPG Memoir*, Volume 1, 108-121.
- EGERTON, R. F. 2006. *Physical principles of electron microscopy an introduction to TEM, SEM, and AEM*, New York, N.Y., Springer Science & Business Media.
- EICHHUBL, P., DAVATZES, N. C. & BECKER, S. P. 2009. Structural and diagenetic control of fluid migration and cementation along the Moab fault, Utah. *AAPG bulletin*, 93, 653-681.
- EICHHUBL, P., GREENE, H., NAEHR, T. & MAHER, N. 2000. Structural control of fluid flow: offshore fluid seepage in the Santa Barbara Basin, California. *Journal of Geochemical Exploration*, 69, 545-549.
- ELTER, P., GRASSO, M., PAROTTO, M. & VEZZANI, L. 2003. Structural setting of the Apennine-Maghrebian thrust belt. *Episodes*, 26, 205-211.
- EVANS, J. P., FORSTER, C. B. & GODDARD, J. V. 1997. Permeability of fault-related rocks, and implications for hydraulic structure of fault zones. *Journal of Structural Geology*, 19, 1393-1404.
- FELIX, R. 1973. *Oligo-Miocene stratigraphy of Malta and Gozo*. PhD thesis, University of Utrecht.
- FERREIRA, T. & RASBAND, W. 2012. ImageJ user guide IJ1. 46r. Available: <https://imagej.nih.gov/ij/docs/guide/> [Accessed 10.05.2016].
- FINZI, Y. & LANGER, S. 2012. Damage in step-overs may enable large cascading earthquakes. *Geophysical Research Letters*, 39, L16303.
- FISHER, Q. & KNIPE, R. J. 1998. Fault sealing processes in siliciclastic sediments. *Geological Society, London, Special Publications*, 147, 117-134.
- FLÜGEL, E. 2010. *Microfacies of Carbonate Rocks, Analysis, Interpretation and Application*, Heidelberg, Springer.
- FOSSSEN, H. & HESTHAMMER, J. 1997. Geometric analysis and scaling relations of deformation bands in porous sandstone. *Journal of Structural Geology*, 19, 1479-1493.
- FOSSSEN, H., JOHANSEN, T. E. S., HESTHAMMER, J. & ROTEVATN, A. 2005. Fault interaction in porous sandstone and implications for reservoir management; examples from southern Utah. *AAPG bulletin*, 89, 1593-1606.
- FOSSSEN, H. & ROTEVATN, A. 2016. Fault linkage and relay structures in extensional settings—A review. *Earth-Science Reviews*, 154, 14-28.
- FOSSMARK, H. S. S. 2015. *Petrophysical properties of deformation bands and their influence on fluid flow in carbonate grainstones: insight from the Maghlaq Fault, Malta*. MSc. Thesis, University of Bergen, unpublished, 102.
- GALEA, P. 2007. Seismic history of the Maltese islands and considerations on seismic risk. *Annals of geophysics*, 50, 725-760.
- GARDINER, W., GRASSO, M. & SEDGELEY, D. 1995. Plio-pleistocene fault movement as evidence for mega-block kinematics within the Hyblean—Malta Plateau, Central Mediterranean. *Journal of geodynamics*, 19, 35-51.

- GARTRELL, A., ZHANG, Y., LISK, M. & DEWHURST, D. 2004. Fault intersections as critical hydrocarbon leakage zones: integrated field study and numerical modelling of an example from the Timor Sea, Australia. *Marine and Petroleum Geology*, 21, 1165-1179.
- GIBA, M., WALSH, J. & NICOL, A. 2012. Segmentation and growth of an obliquely reactivated normal fault. *Journal of Structural Geology*, 39, 253-267.
- GILLESPIE, P., WALSH, J. T. & WATTERSON, J. 1992. Limitations of dimension and displacement data from single faults and the consequences for data analysis and interpretation. *Journal of Structural Geology*, 14, 1157-1172.
- GRANATH, J. W. & CASERO, P. 2004. Tectonic setting of the petroleum systems of Sicily. *AAPG Hedberg Series*, 1, 391-411.
- GRASSO, M., REUTHER, C.-D., BAUMANN, H. & BECKER, A. 1986. Shallow crustal stress and neotectonic framework of the Malta Platform and the Southeastern Pantelleria Rift (Central Mediterranean). *Geol. Romana*, 25, 191-212.
- GUEGUEN, E., DOGLIONI, C. & FERNANDEZ, M. 1997. Lithospheric boudinage in the Western Mediterranean back-arc basin. *Terra Nova*, 9, 184-187.
- GUEGUEN, E., DOGLIONI, C. & FERNANDEZ, M. 1998. On the post-25 Ma geodynamic evolution of the western Mediterranean. *Tectonophysics*, 298, 259-269.
- HALVORSON, S. J. & PARKER HAMILTON, J. 2010. In the aftermath of the Qa'yamat: 1 the Kashmir earthquake disaster in northern Pakistan. *Disasters*, 34, 184-204.
- HARRIS, S., MCALLISTER, E., KNIPE, R. & ODLING, N. 2003. Predicting the three-dimensional population characteristics of fault zones: a study using stochastic models. *Journal of Structural Geology*, 25, 1281-1299.
- IGARASHI, G., SAEKI, S., TAKAHATA, N. & SUMIKAWA, K. 1995. Ground-water radon anomaly before the Kobe earthquake in Japan. *Science*, 269, 60.
- ILLIES, J. H. 1981. Graben formation — the Maltese Islands — a case history. *Tectonophysics*, 73, 151-168.
- INSTRUMENTS, N. 2016. *Scanning Electron Microscopy* [Online]. Available: <http://www.nanoscience.com/technology/sem-technology/> [Accessed 23.05 2016].
- JACKSON, C. A.-L., BELL, R. E., ROTEVATN, A. & TVEDT, A. B. M. Techniques to determine the style of growth of normal seismic-scale syn-sedimentary normal faults. *Geological Society, London, Special Publications*, In press.
- JOHANSEN, T. E. S., FOSSEN, H. & KLUGE, R. 2005. The impact of syn-faulting porosity reduction on damage zone architecture in porous sandstone: an outcrop example from the Moab Fault, Utah. *Journal of Structural Geology*, 27, 1469-1485.
- JOHNSTON, K., VER HOEF, J. M., KRIVORUCHKO, K. & LUCAS, N. 2001. Using ArcGIS geostatistical analyst. ESRI Redlands.
- JOLIVET, L. & FACCENNA, C. 2000. Mediterranean extension and the Africa-Eurasia collision. *Tectonics*, 19, 1095-1106.
- JOLLEY, S. J., BARR, D., WALSH, J. & KNIPE, R. 2007. Structurally complex reservoirs: an introduction. *Geological Society, London, Special Publications*, 292, 1-24.
- JONGSMA, D., VAN HINTE, J. E. & WOODSIDE, J. M. 1985. Geologic structure and neotectonics of the North African continental margin south of Sicily. *Marine and Petroleum Geology*, 2, 156-179.
- KATSANOOU, K., STRATIPOPOULOS, K., ZAGANA, E. & LAMBRAKIS, N. 2010. Radon changes along main faults in the broader Aigion region, NW Peloponnese. *Bulletin of the Geological Society of Greece*, 43, 1726-1736.
- KATTENHORN, S. A., AYDIN, A. & POLLARD, D. D. 2000. Joints at high angles to normal fault strike: an explanation using 3-D numerical models of fault-perturbed stress fields. *Journal of structural Geology*, 22, 1-23.
- KEILIS-BOROK, V. 2002. Earthquake prediction: State-of-the-art and emerging possibilities. *Annual review of earth and planetary sciences*, 30, 1-33.
- KERRICH, R. 1986. Fluid infiltration into fault zones: chemical, isotopic, and mechanical effects. *Pure and applied geophysics*, 124, 225-268.

- KIM, Y.-S., PEACOCK, D. C. P. & SANDERSON, D. J. 2003. Mesoscale strike-slip faults and damage zones at Marsalforn, Gozo Island, Malta. *Journal of Structural Geology*, 25, 793-812.
- KIM, Y.-S., PEACOCK, D. C. P. & SANDERSON, D. J. 2004. Fault damage zones. *Journal of Structural Geology*, 26, 503-517.
- KIM, Y.-S. & SANDERSON, D. J. 2005. The relationship between displacement and length of faults: a review. *Earth-Science Reviews*, 68, 317-334.
- KING, C.-Y., KING, B.-S., EVANS, W. C. & ZHANG, W. 1996. Spatial radon anomalies on active faults in California. *Applied Geochemistry*, 11, 497-510.
- KING, C. Y. 1986. Gas geochemistry applied to earthquake prediction: An overview. *Journal of Geophysical Research: Solid Earth*, 91, 12269-12281.
- KRISTENSEN, T. B., ROTEVATN, A., PEACOCK, D. C., HENSTRA, G. A., MIDTKANDAL, I. & GRUNDVÅG, S.-A. 2016. Structure and flow properties of syn-rift border faults: The interplay between fault damage and fault-related chemical alteration (Dombjerg Fault, Wollaston Forland, NE Greenland). *Journal of Structural Geology*, 92, 99-115.
- LARSEN, P.-H. 1988. Relay structures in a Lower Permian basement-involved extension system, East Greenland. *Journal of Structural Geology*, 10, 3-8.
- LÜTTGE, A., BOLTON, E. W. & LASAGA, A. C. 1999. An interferometric study of the dissolution kinetics of anorthite: the role of reactive surface area. *American Journal of Science*, 299, 652-678.
- MAERTEN, L., GILLESPIE, P. & POLLARD, D. D. 2002. Effects of local stress perturbation on secondary fault development. *Journal of Structural Geology*, 24, 145-153.
- MAILLOUX, B. J., PERSON, M., KELLEY, S., DUNBAR, N., CATHER, S., STRAYER, L. & HUDLESTON, P. 1999. Tectonic controls on the hydrogeology of the Rio Grande Rift, New Mexico. *Water Resources Research*, 35, 2641-2659.
- MANZOCCHI, T. 2002. The connectivity of two-dimensional networks of spatially correlated fractures. *Water Resources Research*, 38, 1-20.
- MARCHEV, P., KAISER-ROHRMEIER, M., HEINRICH, C., OVTCHAROVA, M., VON QUADT, A. & RAICHEVA, R. 2005. 2: Hydrothermal ore deposits related to post-orogenic extensional magmatism and core complex formation: The Rhodope Massif of Bulgaria and Greece. *Ore Geology Reviews*, 27, 53-89.
- MARRETT, R. & ALLMENDINGER, R. W. 1991. Estimates of strain due to brittle faulting: sampling of fault populations. *Journal of Structural Geology*, 13, 735-738.
- MARTEL, S. J. 1990. Formation of compound strike-slip fault zones, Mount Abbot quadrangle, California. *Journal of Structural Geology*, 12, 869-882.
- MARTEL, S. J. & BOGER, W. A. 1998. Geometry and mechanics of secondary fracturing around small three-dimensional faults in granitic rock. *Journal of Geophysical Research: Solid Earth*, 103, 21299-21314.
- MAYER, A., MAY, W., LUKKARILA, C. & DIEHL, J. 2007. Estimation of fault-zone conductance by calibration of a regional groundwater flow model: Desert Hot Springs, California. *Hydrogeology Journal*, 15, 1093-1106.
- MAZZULLO, S. 2004. Overview of porosity evolution in carbonate reservoirs. *Kansas Geological Society Bulletin*, 79, 20-28.
- MCKINSTRY, H. E. 1948. *Mining Geology*. Englewood Cliffs, New Jersey: Prentice-Hall
- MICALLEF, A., BERNDT, C. & DEBONO, G. 2011. Fluid flow systems of the Malta Plateau, Central Mediterranean Sea. *Marine Geology*, 284, 74-85.
- MICALLEF, A., FOGLINI, F., LE BAS, T., ANGELETTI, L., MASELLI, V., PASUTO, A. & TAVIANI, M. 2013. The submerged paleolandscape of the Maltese Islands: Morphology, evolution and relation to Quaternary environmental change. *Marine Geology*, 335, 129-147.
- MICHIE, E., HAINES, T., HEALY, D., NEILSON, J., TIMMS, N. E. & WIBBERLEY, C. 2014. Influence of carbonate facies on fault zone architecture. *Journal of Structural Geology*, 65, 82-99.
- MISSENARD, Y., BERTRAND, A., VERGÉLY, P., BENEDICTO, A., CUSHING, M.-E. & ROCHER, M. 2014. Fracture-fluid relationships: implications for the sealing capacity of clay layers—Insights from

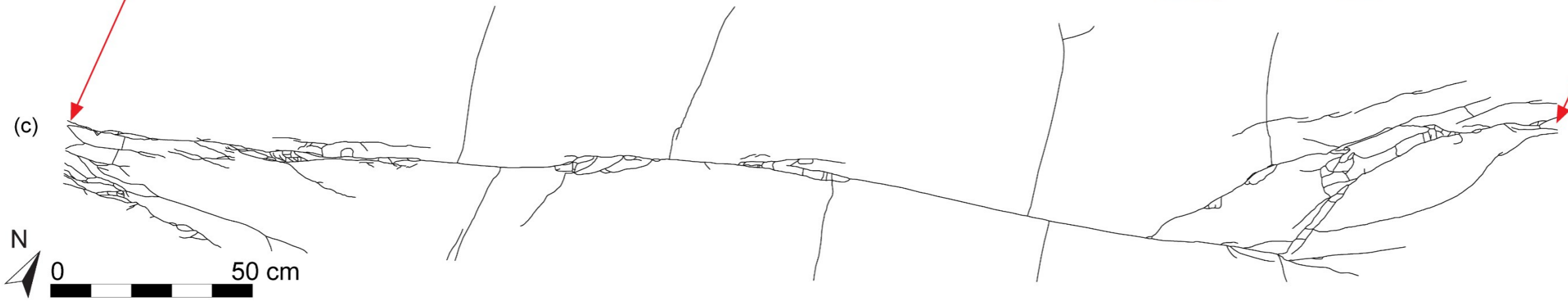
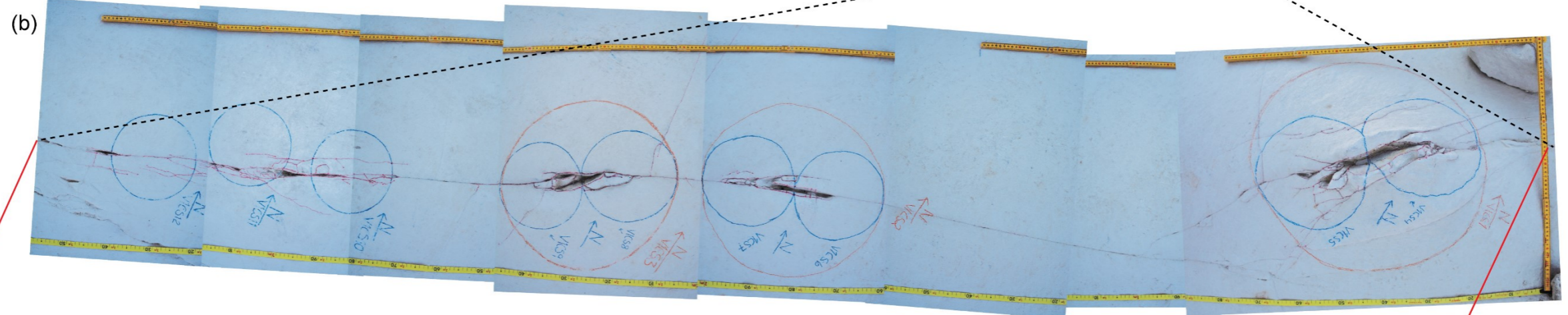
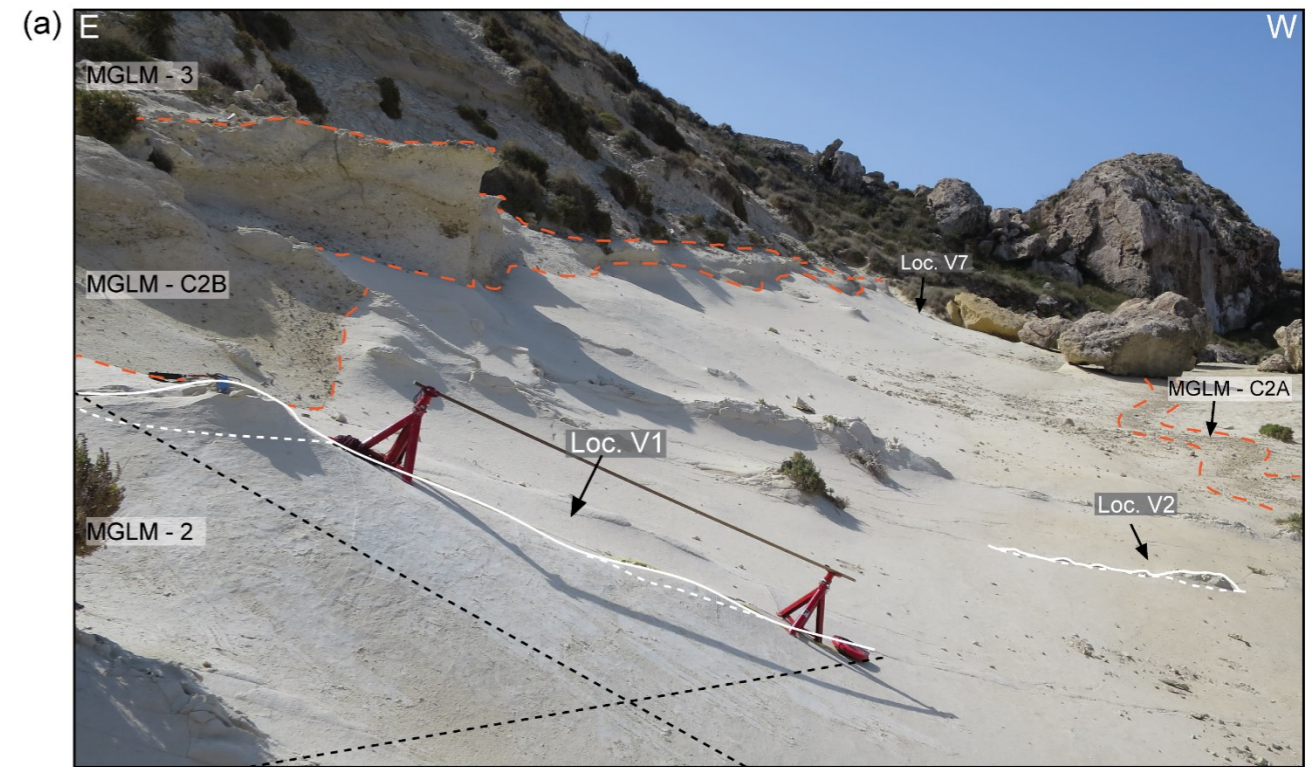
- field study of the Blue Clay formation, Maltese islands. *Bulletin de la Société Géologique de France*, 185, 51-63.
- MORLEY, C. & NIXON, C. 2016. Topological characteristics of simple and complex normal fault networks. *Journal of Structural Geology*, 84, 68-84.
- MORLEY, C. K. 2002. Evolution of large normal faults: Evidence from seismic reflection data. *AAPG bulletin*, 86, 961-978.
- MOUSSA, M. M. & EL ARABI, A.-G. M. 2003. Soil radon survey for tracing active fault: a case study along Qena-Safaga road, Eastern Desert, Egypt. *Radiation Measurements*, 37, 211-216.
- MØLLER-PEDERSEN, P. & KOESTLER, A. G. 1997. *Hydrocarbon Seals: Importance for Exploration and Production*, Singapore, Elsevier Science.
- NELSON, R. A. 2001. *Geologic analysis of naturally fractured reservoirs*, Houston, Texas, Gulf Publishing Co.
- NEWHOUSE, W. H. 1942. *Ore deposits as related to structural features*, Princeton, New Jersey, Princeton University Press.
- OGATA, K., SENGHER, K., BRAATHEN, A. & TVERANGER, J. 2014. Fracture corridors as seal-bypass systems in siliciclastic reservoir-cap rock successions: Field-based insights from the Jurassic Entrada Formation (SE Utah, USA). *Journal of Structural Geology*, 66, 162-187.
- OLIVER, N. 1996. Review and classification of structural controls on fluid flow during regional metamorphism. *Journal of Metamorphic Geology*, 14, 477-492.
- ONO, T., YOSHIDA, H. & METCALFE, R. 2016. Use of fracture filling mineral assemblages for characterizing water-rock interactions during exhumation of an accretionary complex: An example from the Shimanto Belt, southern Kyushu Japan. *Journal of Structural Geology*, 87, 81-94.
- ORTEGA, O. & MARRETT, R. 2000. Prediction of macrofracture properties using microfracture information, Mesaverde Group sandstones, San Juan basin, New Mexico. *Journal of Structural Geology*, 22, 571-588.
- PEACOCK, D. C. P., NIXON, C., ROTEVATN, A., SANDERSON, D. & ZULUAGA, L. 2016. Glossary of fault and other fracture networks. *Journal of Structural Geology*, 92, 12-29.
- PEACOCK, D. C. P. & SANDERSON, D. J. 1991. Displacements, segment linkage and relay ramps in normal fault zones. *Journal of Structural Geology*, 13, 721-733.
- PEACOCK, D. C. P. & SANDERSON, D. J. 1994. Geometry and development of relay ramps in normal fault systems. *AAPG bulletin*, 78, 147-165.
- PEDLEY, H., HOUSE, M. & WAUGH, B. 1976. The geology of Malta and Gozo. *Proceedings of the Geologists' Association*, 87, 325-341.
- PUTZ-PERRIER, M. W. & SANDERSON, D. J. 2010. Distribution of faults and extensional strain in fractured carbonates of the North Malta Graben. *AAPG Bulletin*, 94, 435-456.
- REUTHER, C.-D. & EISBACHER, G. 1985. Pantelleria Rift—crustal extension in a convergent intraplate setting. *Geologische Rundschau*, 74, 585-597.
- RIPPON, J. 1985. Contoured patterns of the throw and hade of normal faults in the Coal Measures (Westphalian) of north-east Derbyshire. *Proceedings of the Yorkshire Geological and Polytechnic Society*, 45, 147-161.
- ROSENBAUM, G., LISTER, G. S. & DUBOZ, C. 2002. Reconstruction of the tectonic evolution of the western Mediterranean since the Oligocene. *Journal of the Virtual Explorer*, 8, 107-130.
- ROTEVATN, A. & BASTESSEN, E. 2014. Fault linkage and damage zone architecture in tight carbonate rocks in the Suez Rift (Egypt): implications for permeability structure along segmented normal faults. *Geological Society, London, Special Publications*, 374, 79-95.
- ROTEVATN, A., BUCKLEY, S. J., HOWELL, J. A. & FOSSEN, H. 2009a. Overlapping faults and their effect on fluid flow in different reservoir types: A LIDAR-based outcrop modeling and flow simulation study. *AAPG bulletin*, 93, 407-427.
- ROTEVATN, A. & FOSSEN, H. 2011. Simulating the effect of subseismic fault tails and process zones in a siliciclastic reservoir analogue: implications for aquifer support and trap definition. *Marine and Petroleum Geology*, 28, 1648-1662.

- ROTEVATN, A., FOSSEN, H., HESTHAMMER, J., AAS, T. E. & HOWELL, J. A. 2007. Are relay ramps conduits for fluid flow? Structural analysis of a relay ramp in Arches National Park, Utah. *Geological Society, London, Special Publications*, 270, 55-71.
- ROTEVATN, A., THORSHEIM, E., BASTESEN, E., FOSSMARK, H. S. S., TORABI, A. & SÆLEN, G. 2016. Sequential growth of deformation bands in carbonate grainstones in the hangingwall of an active growth fault: Implications for deformation mechanisms in different tectonic regimes. *Journal of Structural Geology*, 90, 27-47.
- ROTEVATN, A., TVERANGER, J., HOWELL, J. & FOSSEN, H. 2009b. Dynamic investigation of the effect of a relay ramp on simulated fluid flow: geocellular modelling of the Delicate Arch Ramp, Utah. *Petroleum Geoscience*, 15, 45-58.
- ROWLAND, J. & SIBSON, R. 2004. Structural controls on hydrothermal flow in a segmented rift system, Taupo Volcanic Zone, New Zealand. *Geofluids*, 4, 259-283.
- RYKKELID, E. & FOSSEN, H. 2002. Layer rotation around vertical fault overlap zones: observations from seismic data, field examples, and physical experiments. *Marine and Petroleum Geology*, 19, 181-192.
- SANDERSON, D. J. & NIXON, C. W. 2015. The use of topology in fracture network characterization. *Journal of Structural Geology*, 72, 55-66.
- SCHLUMBERGER. 2016. *Carbonate Reservoirs* [Online]. www.slb.com: Schlumberger Limited. Available: http://www.slb.com/services/technical_challenges/carbonates.aspx [Accessed 05.11 2016].
- SEGALL, P. & POLLARD, D. D. 1980. Mechanics of discontinuous faults. *Journal of Geophysical Research: Solid Earth*, 85, 4337-4350.
- SEGALL, P. & POLLARD, D. D. 1983. Nucleation and growth of strike slip faults in granite. *Journal of Geophysical Research: Solid Earth*, 88, 555-568.
- SHIPTON, Z. K., EVANS, J. P., KIRSCHNER, D., KOLESAR, P. T., WILLIAMS, A. P. & HEATH, J. 2004. Analysis of CO₂ leakage through 'low-permeability' faults from natural reservoirs in the Colorado Plateau, east-central Utah. *Geological Society, London, Special Publications*, 233, 43-58.
- SHIPTON, Z. K., EVANS, J. P. & THOMPSON, L. B. 2005. The geometry and thickness of deformation-band fault core and its influence on sealing characteristics of deformation-band fault zones. *AAPG Memoir*, 85, 181-195.
- SIBSON, R. H. 1996. Structural permeability of fluid-driven fault-fracture meshes. *Journal of Structural Geology*, 18, 1031-1042.
- SUN, Q. S. & SLOAN, R. Quantification of uncertainty in recovery efficiency predictions: lessons learned from 250 mature carbonate fields. SPE Annual Technical Conference and Exhibition, 2003. Society of Petroleum Engineers.
- TALWANI, P. 1999. Fault geometry and earthquakes in continental interiors. *Tectonophysics*, 305, 371-379.
- TAMAGAWA, T. & POLLARD, D. D. 2008. Fracture permeability created by perturbed stress fields around active faults in a fractured basement reservoir. *AAPG bulletin*, 92, 743-764.
- TANNER, A. B. 1980. Radon migration in the ground: a supplementary review. *Natural radiation environment III: Springfield*, 1, 5-56.
- THORSHEIM, E. 2015. *The geometry and evolution of deformation bands in carbonate grainstones along the Maghlaq Fault, Malta*. MSc. Thesis, University of Bergen, unpublished, 91.
- TRUDGILL, B. & CARTWRIGHT, J. 1994. Relay-ramp forms and normal-fault linkages, Canyonlands National Park, Utah. *Geological Society of America Bulletin*, 106, 1143-1157.
- VERHAERT, G., MUCHEZ, P., KEPPENS, E. & SINTUBIN, M. 2009. Fluid impact and spatial and temporal evolution of normal faulting in limestones. A case study in the Burdur-Isparta Region (SW Turkey). *Geologica Belgica*, 12, 59-73.
- VERMILYE, J. M. & SCHOLZ, C. H. 1998. The process zone: A microstructural view of fault growth. *Journal of Geophysical Research: Solid Earth*, 103, 12223-12237.
- VIRK, H. & SINGH, B. 1993. Radon anomalies in soil-gas and groundwater as earthquake precursor phenomena. *Tectonophysics*, 227, 215-224.

- WALSH, J., BAILEY, W., CHILDS, C., NICOL, A. & BONSON, C. 2003. Formation of segmented normal faults: a 3-D perspective. *Journal of Structural Geology*, 25, 1251-1262.
- WALSH, J., WATTERSON, J., HEATH, A., GILLESPIE, P. & CHILDS, C. 1998. Assessment of the effects of sub-seismic faults on bulk permeabilities of reservoir sequences. *Geological Society, London, Special Publications*, 127, 99-114.
- WALSH, J. J., NICOL, A. & CHILDS, C. 2002. An alternative model for the growth of faults. *Journal of Structural Geology*, 24, 1669-1675.
- WALSH, J. J. & WATTERSON, J. 1988. Analysis of the relationship between displacements and dimensions of faults. *Journal of Structural Geology*, 10, 239-247.
- WALSH, J. J. & WATTERSON, J. 1991. Geometric and kinematic coherence and scale effects in normal fault systems. *Geological Society, London, Special Publications*, 56, 193-203.
- WATTERSON, J. 1986. Fault dimensions, displacements and growth. *pure and applied geophysics*, 124, 365-373.
- WILKINS, S. J., GROSS, M. R., WACKER, M., EYAL, Y. & ENGELDER, T. 2001. Faulted joints: kinematics, displacement-length scaling relations and criteria for their identification. *Journal of Structural Geology*, 23, 315-327.
- WITTKKE, J. H. 2015. *Electron Microanalysis Core Facility* [Online]. Northern Arizona University, Flagstaff, Arizona. Available: <http://nau.edu/cefns/labs/electron-microprobe/glg-510-class-notes/instrumentation/> [Accessed 11.07 2016].
- XIAO-SHUANG, X., JING-RU, T., HUA, K. & SHAO-XUN, H. 2005. Control of relay structure on mineralization of sedimentary-exhalative ore deposit in growth faults of graben systems. *Journal of Central South University of Technology*, 12, 340-345.
- YELLIN-DROR, A., GRASSO, M., BEN-AVRAHAM, Z. & TIBOR, G. 1997. The subsidence history of the northern Hyblean plateau margin, southeastern Sicily. *Tectonophysics*, 282, 277-289.
- YOSHIDA, H., METCALFE, R., YAMAMOTO, K., MURAKAMI, Y., HOSHII, D., KANEKIYO, A., NAGANUMA, T. & HAYASHI, T. 2008. Redox front formation in an uplifting sedimentary rock sequence: An analogue for redox-controlling processes in the geosphere around deep geological repositories for radioactive waste. *Applied Geochemistry*, 23, 2364-2381.
- YOSHIDA, H., YAMAMOTO, K., YOGO, S. & MURAKAMI, Y. 2006. An analogue of matrix diffusion enhanced by biogenic redox reaction in fractured sedimentary rock. *Journal of Geochemical Exploration*, 90, 134-142.
- ZEEB, C., GOMEZ-RIVAS, E., BONS, P. D. & BLUM, P. 2013. Evaluation of sampling methods for fracture network characterization using outcrops. *AAPG Bulletin*, 97, 1545-1566.
- ZHANG, Y., HOBBS, B. E., ORD, A., BARNICOAT, A., ZHAO, C., WALSH, J. L. & LIN, G. 2003. The influence of faulting on host-rock permeability, fluid flow and ore genesis of gold deposits: a theoretical 2D numerical model. *Journal of Geochemical Exploration*, 78, 279-284.
- ZHOU, W., APKARIAN, R., WANG, Z. L. & JOY, D. 2007. Fundamentals of Scanning Electron Microscopy (SEM). In: ZHOU, W. & WANG, Z. L. (eds.) *Scanning Microscopy for Nanotechnology: Techniques and Applications*. Springer New York, NY.
- ZIMMERMAN, R. & MAIN, I. 2003. Hydromechanical behavior of fractured rocks. *International geophysics*, 89, 363-421.

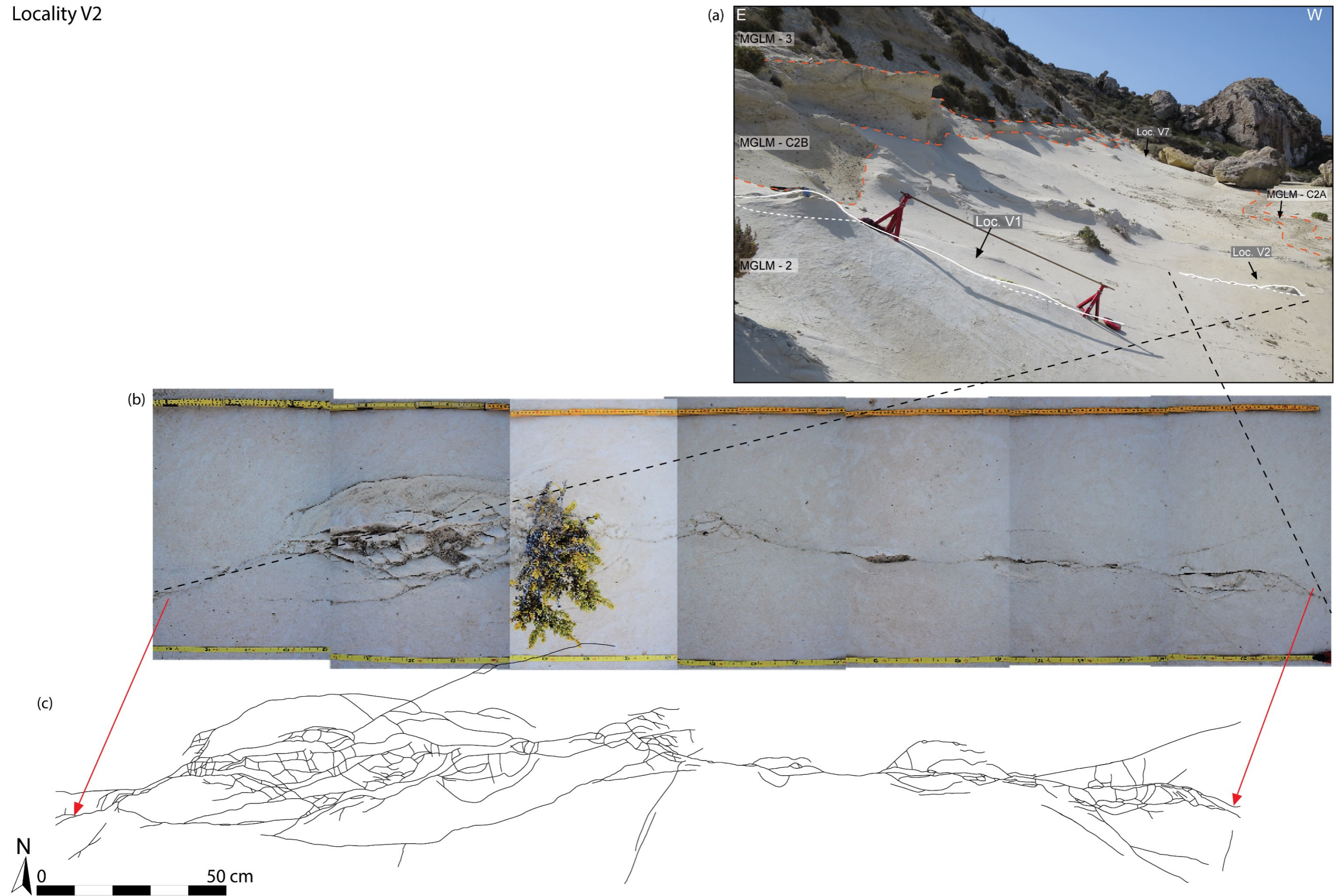
Appendix I: Locality overviews

Locality V1



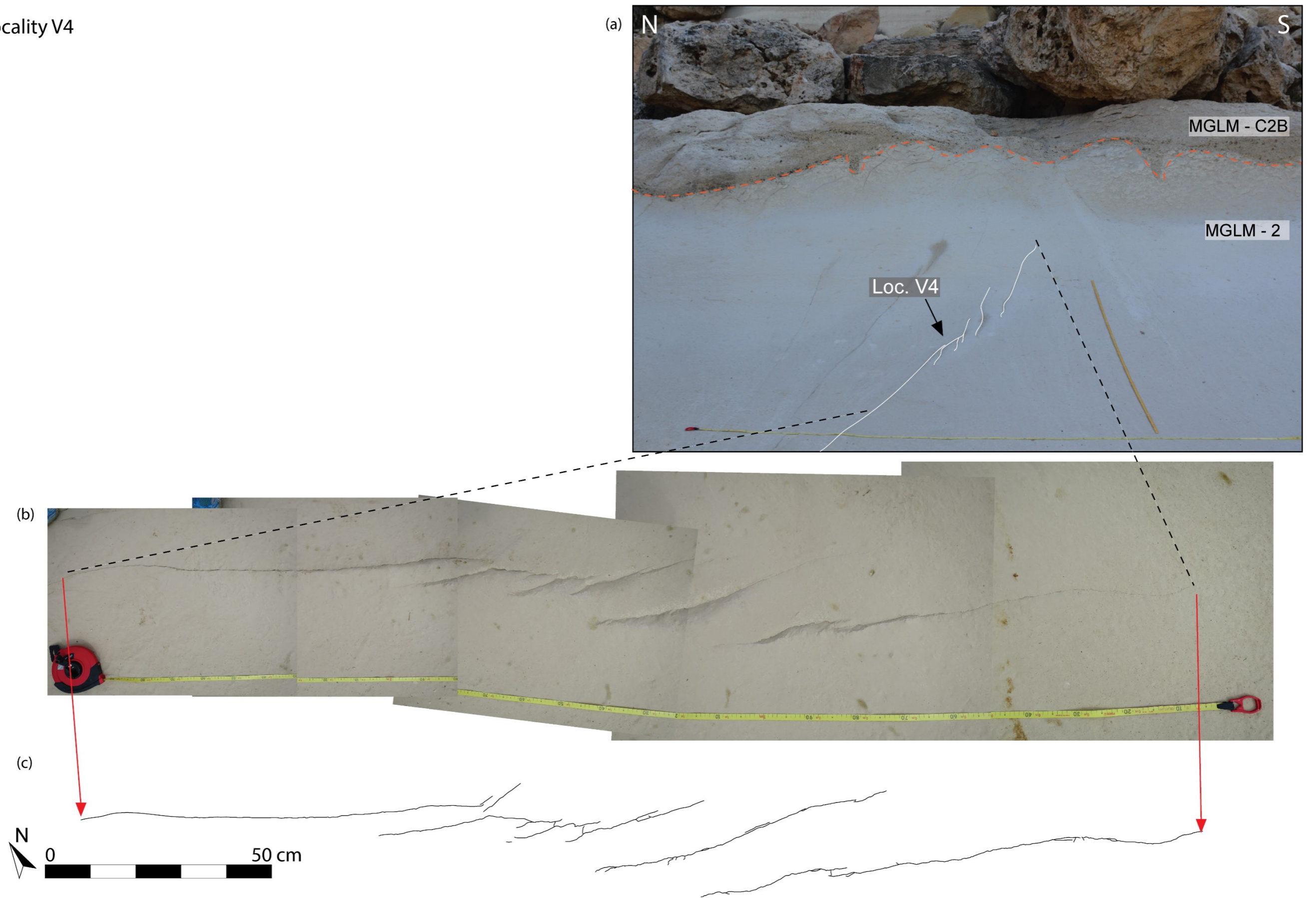
Locality V1: showing (a) overview field photo, with locality V1 in the front of the photo, highlighted by white lines. Car jacks approximately 30 cm high. (b) photomosaic of the locality. (c) digitized map of fracture network on the locality, based on the photomosaic.

Locality V2



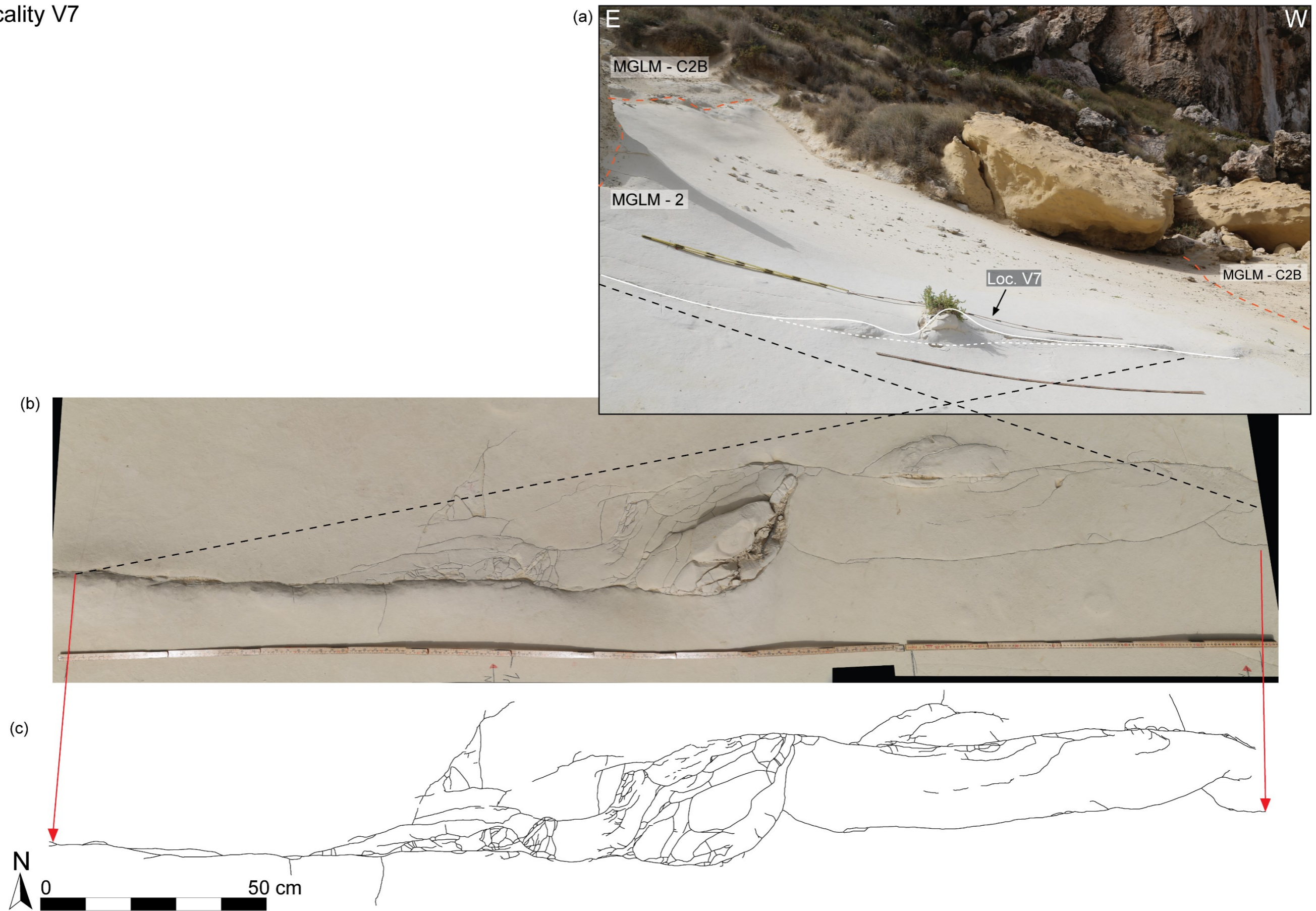
Locality V2: showing (a) overview field photo, with locality V2 in the back of the photo, highlighted by white lines. Car jacks approximately 30 cm high. (b) photomosaic of the locality. (c) digitized map of fracture network on the locality, based on the photomosaic.

Locality V4



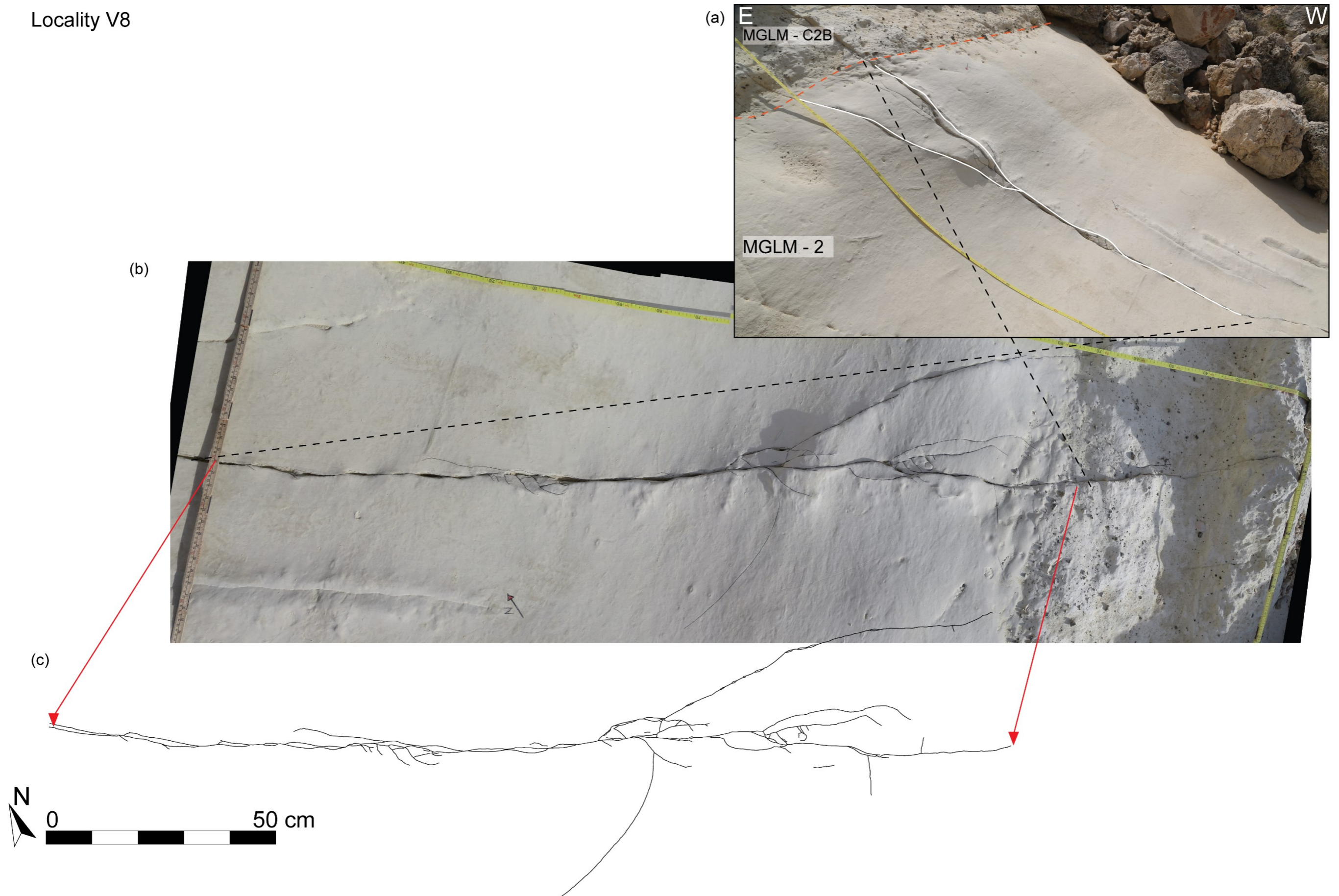
Locality V4: showing (a) overview field photo of the locality. E-W oriented yardstick, 2 m, for scale. (b) photomosaic of the locality. (c) digitized map of fracture network on the locality, based on the photomosaic.

Locality V7



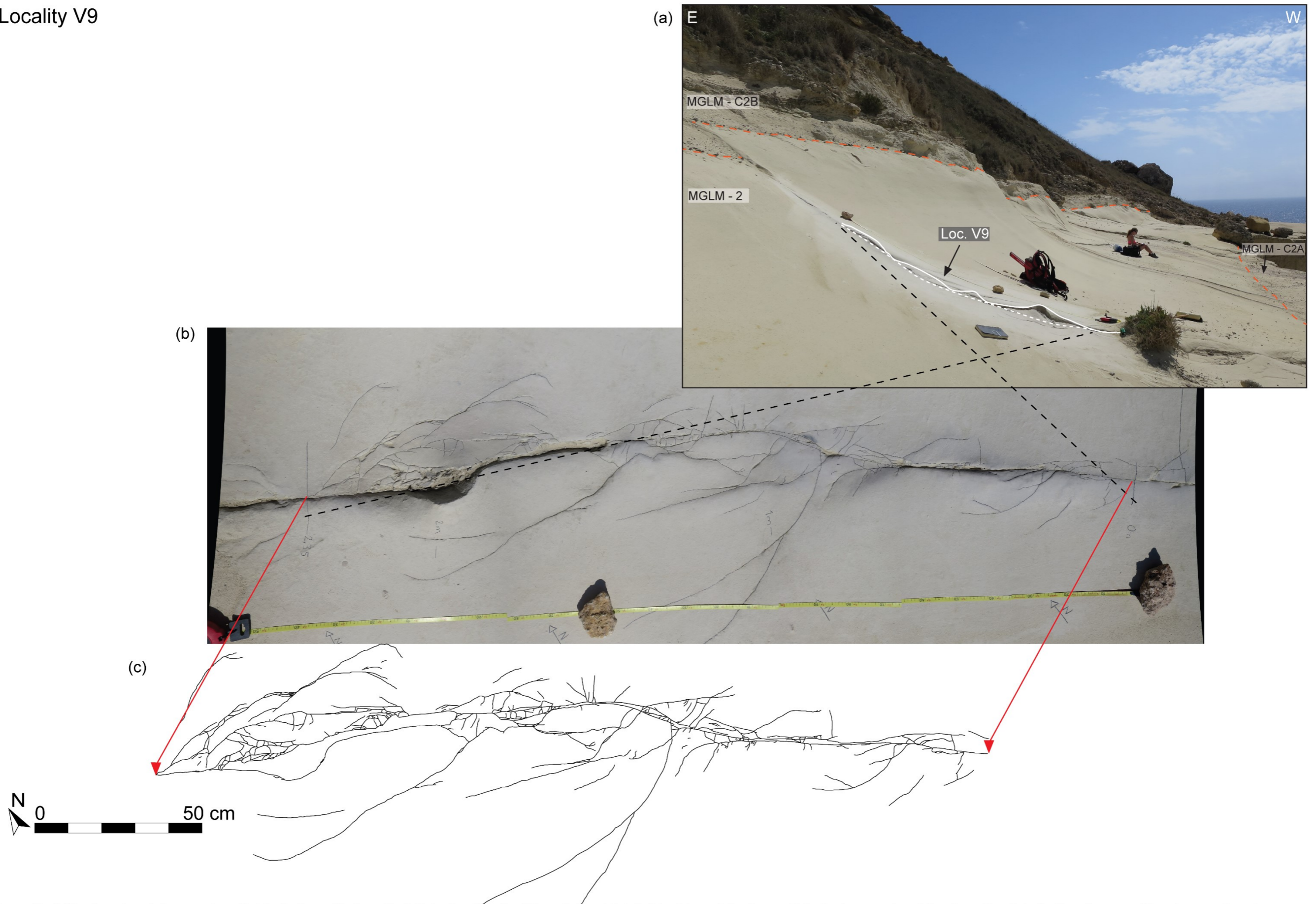
Locality V7: showing (a) overview field photo where the topographic variations can be seen highlighted by the white lines. (b) photomosaic of the locality. (c) digitized map of fracture network on the locality, based on the photomosaic.

Locality V8



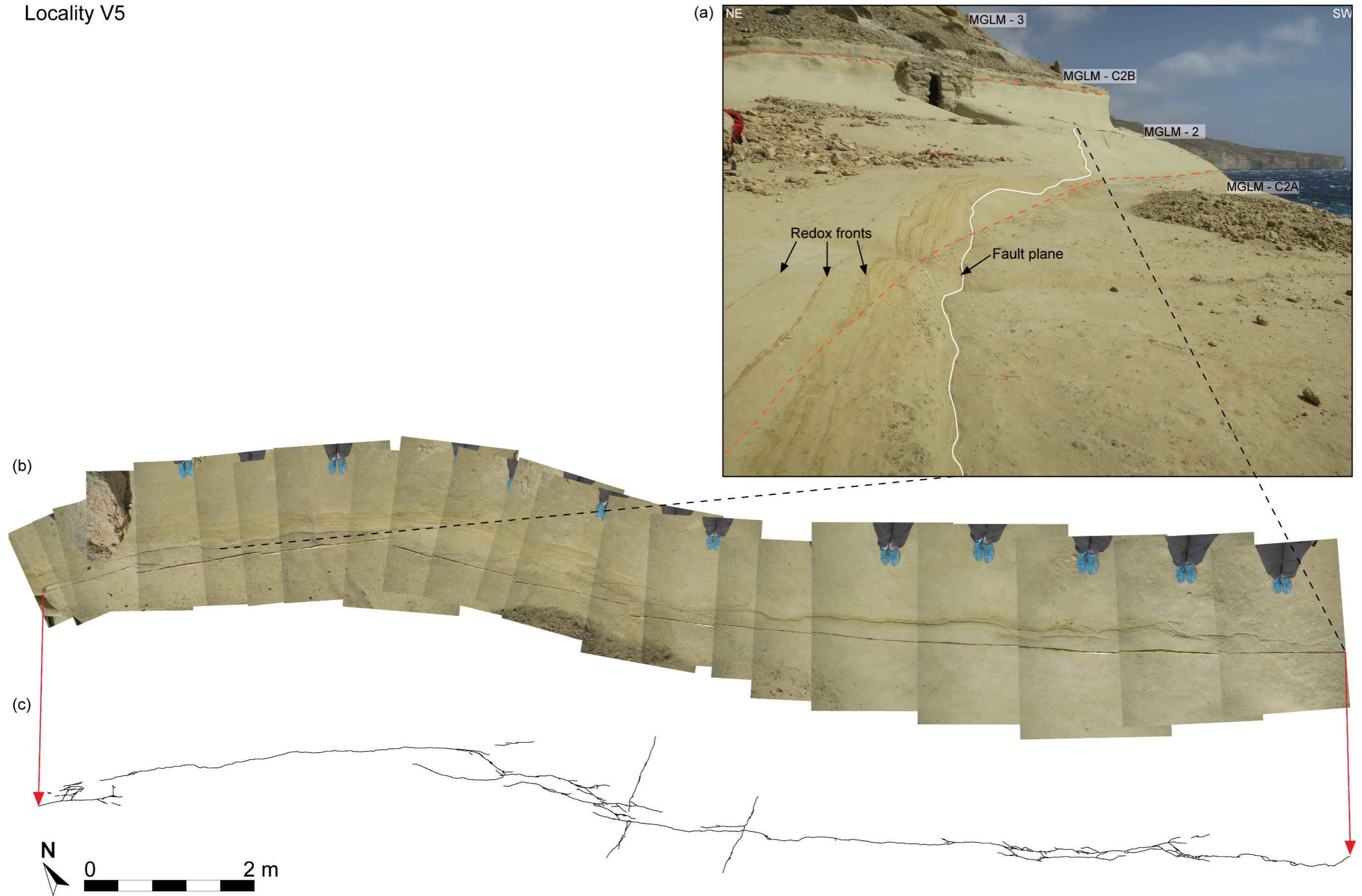
Locality V8: showing (a) overview field photo with the placement of the fracture network highlighted by white lines. (b) photomosaic of the locality. (c) digitized map of fracture network on the locality, based on the photomosaic.

Locality V9



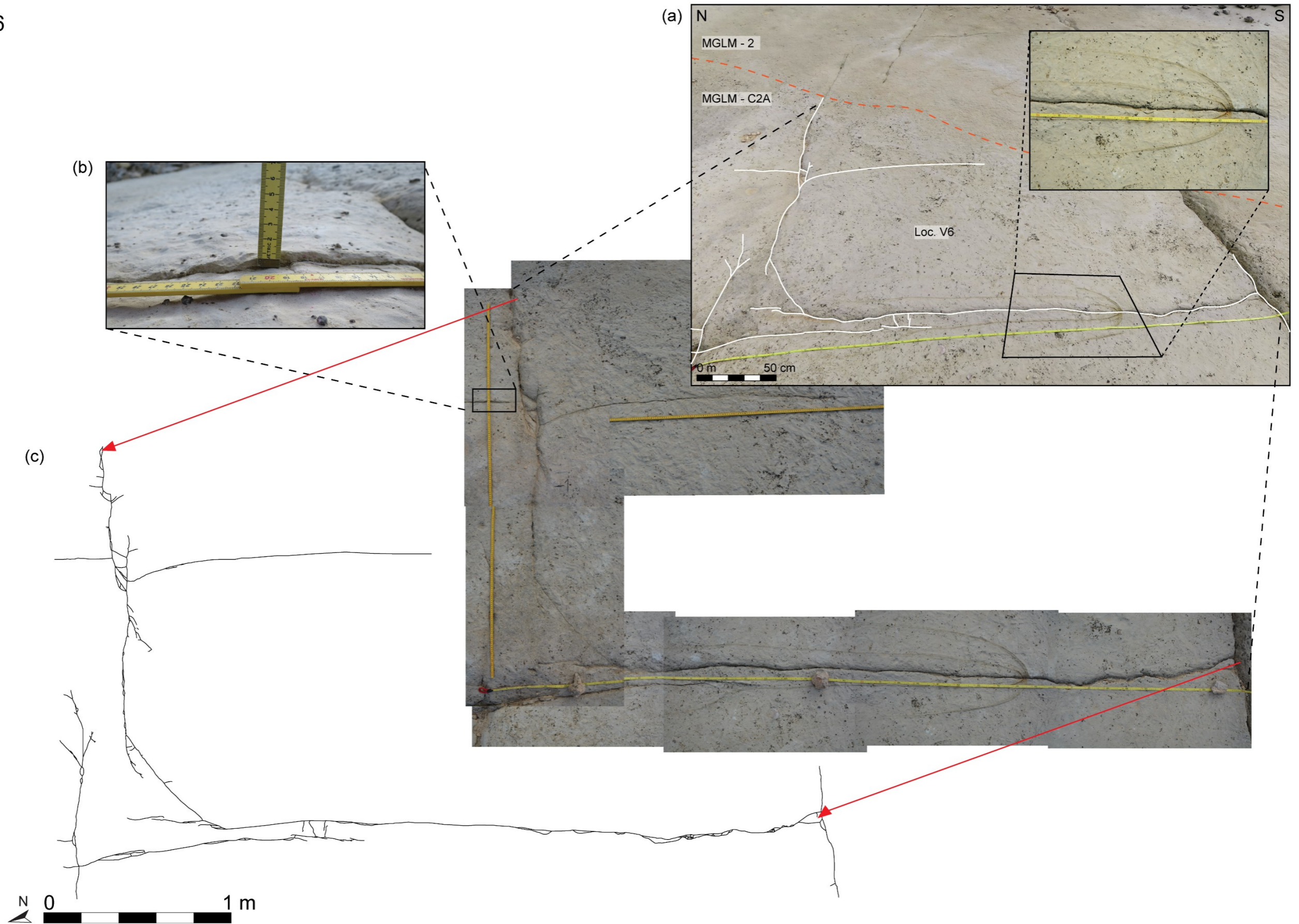
Locality V9: showing (a) overview field photo, with locality V1 in the front of the photo, highlighted by white lines. (b) photomosaic of the locality. (c) digitized map of fracture network on the locality, based on the photomosaic.

Locality V5



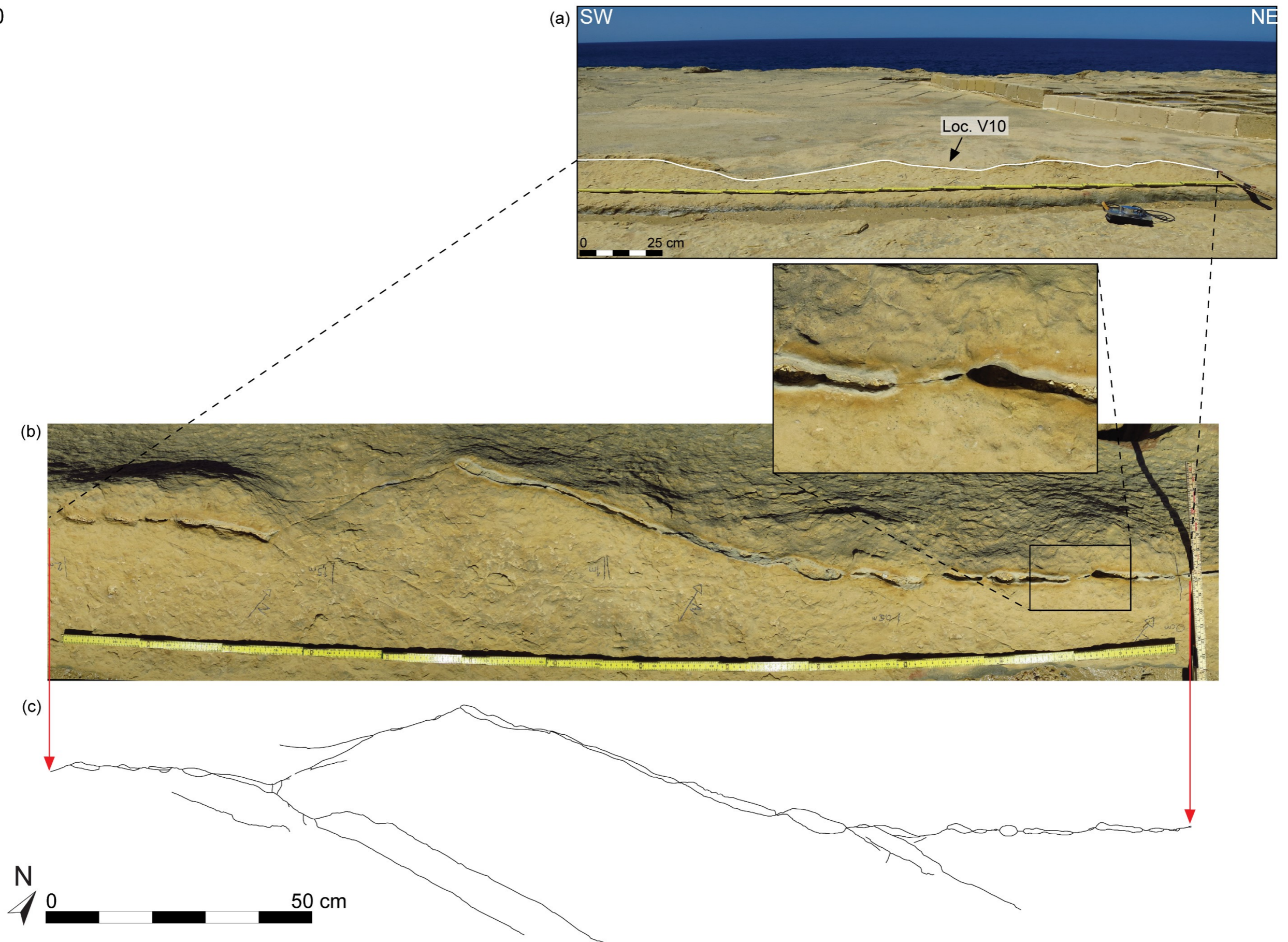
Locality V5: showing (a) overview field photo, where the fault plane is marked by a white line. Width of photo in the front approximately 150 cm. (b) photomosaic of the locality. (c) digitized map of fracture network on the locality, based on the photomosaic.

Locality V6



Locality V6: showing (a) overview field photo, with the fracture network briefly sketched in white. (b) photomosaic of the locality, including a close up showing the mm-scale displacement along the segment. (c) digitized map of fracture network on the locality, based on the photomosaic.

Locality V10

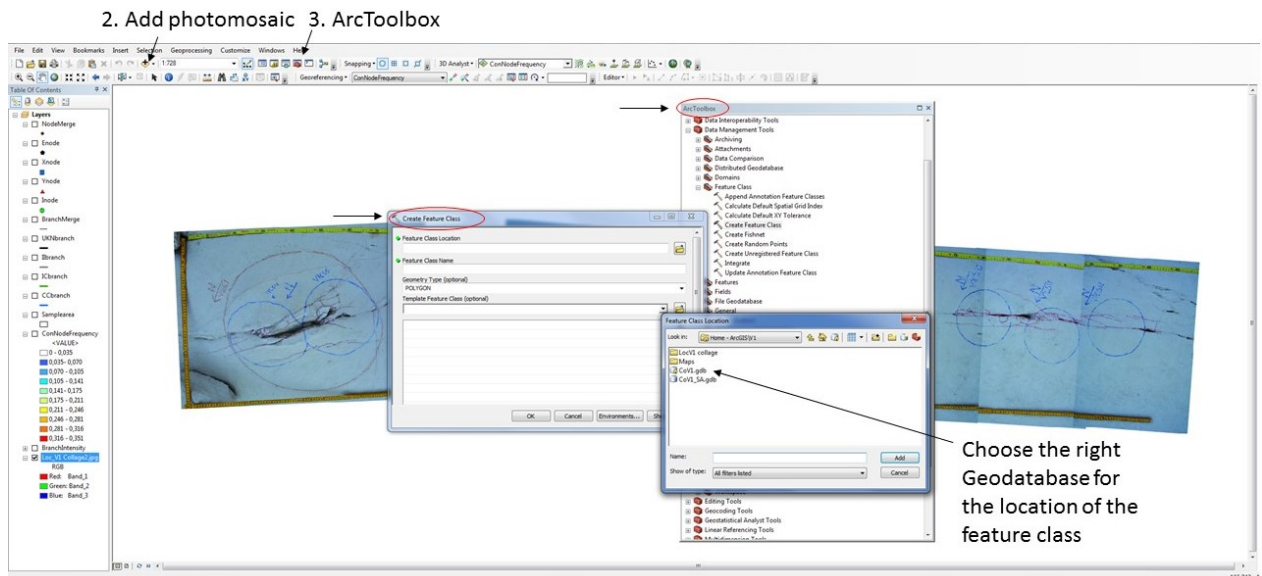


Locality V10: showing (a) overview field photo, with locality V10 highlighted by a white line in the front of the photo. (b) photomosaic of the locality, with enlarged section showing the reduced and oxidized rim around small pull-aparts. (c) digitized map of fracture network on the locality, based on the photomosaic.

Appendix II: ArcGIS workflow

Getting started – Create nodes and branches

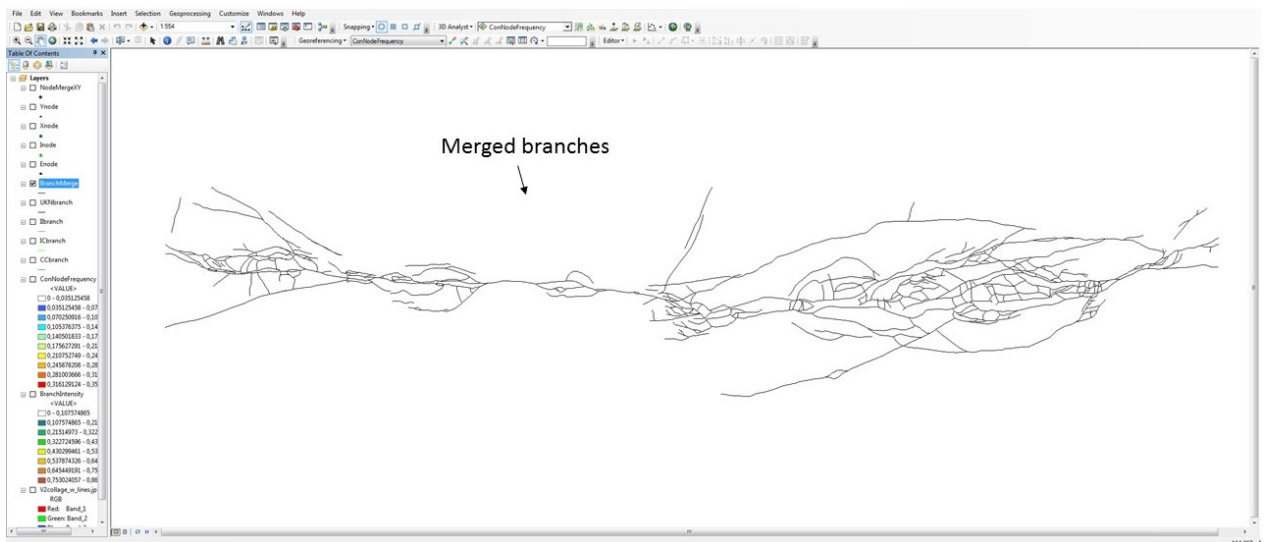
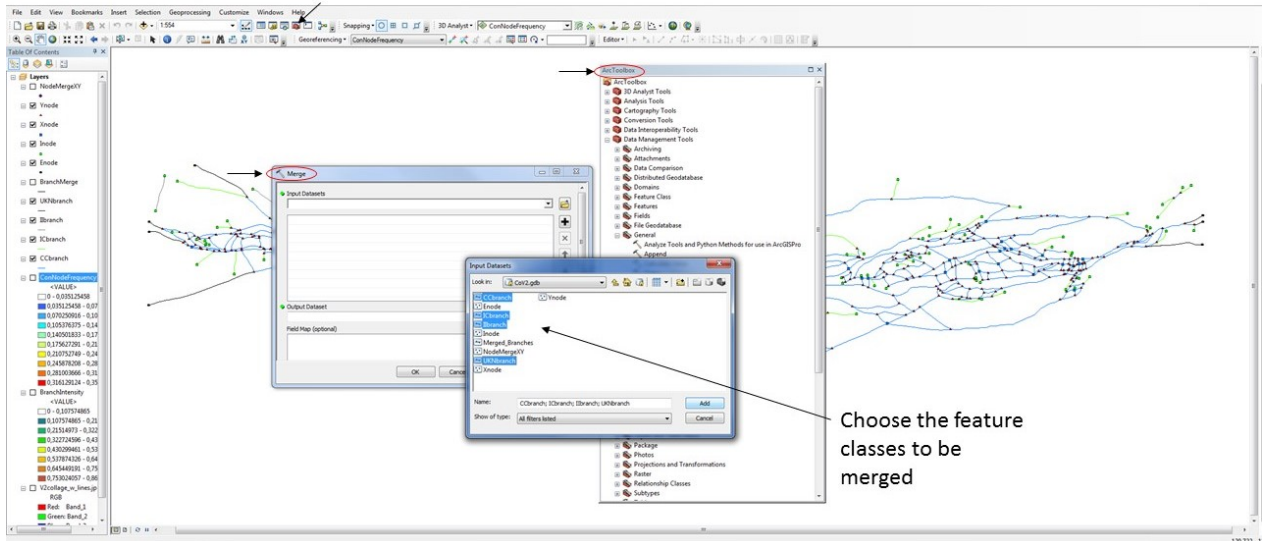
1. A new Geo-database (gdb. file) is made for every new project to keep the created feature classes of the project organized.
2. The right coordinate settings are chosen in the “data frame properties” found by right clicking on the new canvas, then the photomosaic is imported and the scale is set.
3. Feature classes for the different elements of the network is created from the ArcToolbox, as these are used for the interpretation. The nodes (I, Y, X and E) are created as a point feature class, while the branches (I-I, I-C, C-C and Unknown) are created as polylines. To get the length of the branches calculated automatically this function has to be enabled when the feature classes are created.



Merge feature classes

- Use the “merge” tool in the ArcToolbox and choose all the feature classes that shall be merged from the geodatabase. In this case the connecting nodes (X and Y) were merged, and all or the branches.

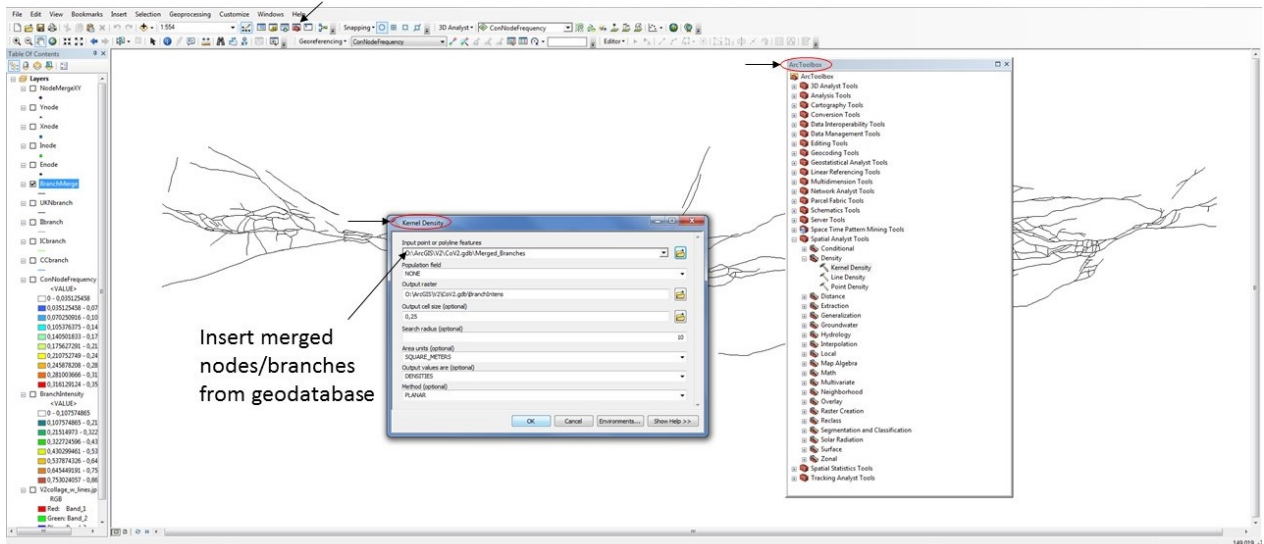
3. ArcToolbox



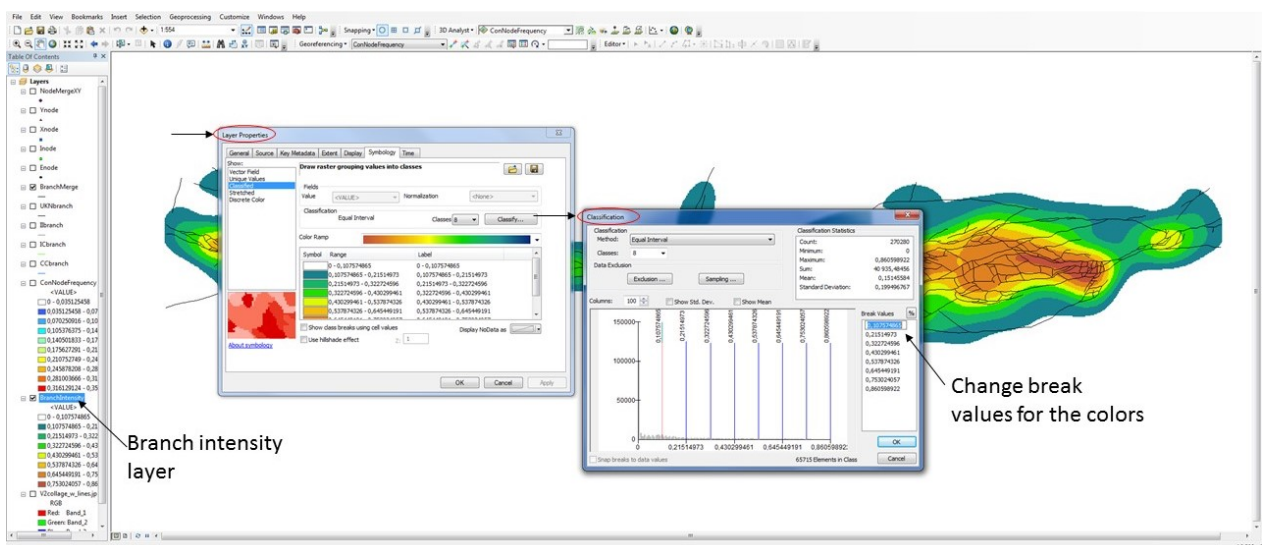
Create contour maps

- The “Kernel density” tool under “Spatial analyst tools” in the ArcToolbox is used to create density maps of the Connecting node frequency and the Branch intensity.

3. ArcToolbox



- Colors and range values for the density maps can be changed in the layer properties, which is found by right clicking the layer. This is done to get the same intervals for all the different localities. The colors can be changed in the color ramp under the “symbology” tab, and the break values for each color can be specified by clicking on “classify” just above the color ramp.



Extracted data

- Data extracted from ArcGIS is plotted in a Microsoft Excel sheet (designed for topology data sampling by Casey Nixon) where node and branch proportion is calculated along with branch length, intensity and frequency, and number of lines, average line length and connections per line.

The data that is plotted in excel automatically transfers to another excel sheet where it can be used to create triangular plots.

The screenshot shows an Excel spreadsheet with the following columns:

- Basic Data:** Sample No, Damage Type, Sample Area, Total, Trace length, I, V, X, E.
- Node Analysis:** No. Lines, No. Branch, Average Line Leng, Average Branch Len, Connections.
- Branch Analysis:** No. Branch, Cs.

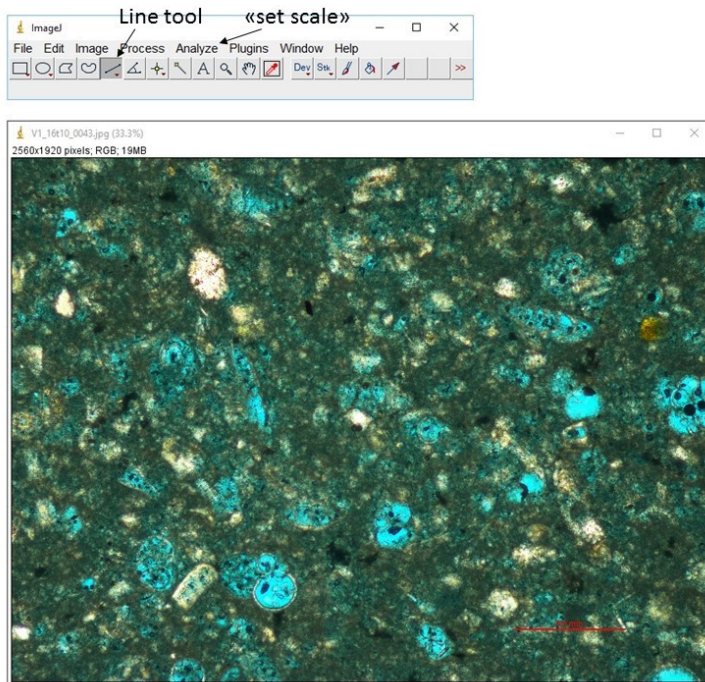
Two red boxes highlight columns in the 'Basic Data' and 'Branch Analysis' sections, with arrows pointing to them from the text "Data extracted from ArcGIS".

The screenshot displays an Excel spreadsheet with several data tables and diagrams. The main table on the left is titled 'Node Triangle Data' and contains columns for 'Node No.', 'X', 'Y', 'K', 'X Value', 'Y Value', 'K', 'X Value', and 'Y Value'. It lists data for nodes 1 through 10. To the right, there are two smaller tables: 'AV TRIANGLE DATA' and 'Nodes Around', both with similar column structures. Below these tables are two diagrams: 'I' and 'B'. Diagram 'I' shows a triangle with nodes 1, 2, and 3 at the vertices and nodes 4 through 10 along its edges. Diagram 'B' shows a similar triangle with nodes 1, 2, and 3 at the vertices and nodes 4 through 10 along its edges, but with a different internal structure. Annotations include 'Data automatically transferred from sheet 1' with arrows pointing to the data tables, and 'Sheet 1 Sheet 2' with arrows pointing to the diagrams. The Excel interface shows the 'Formler' (Formulas) ribbon and various toolbars.

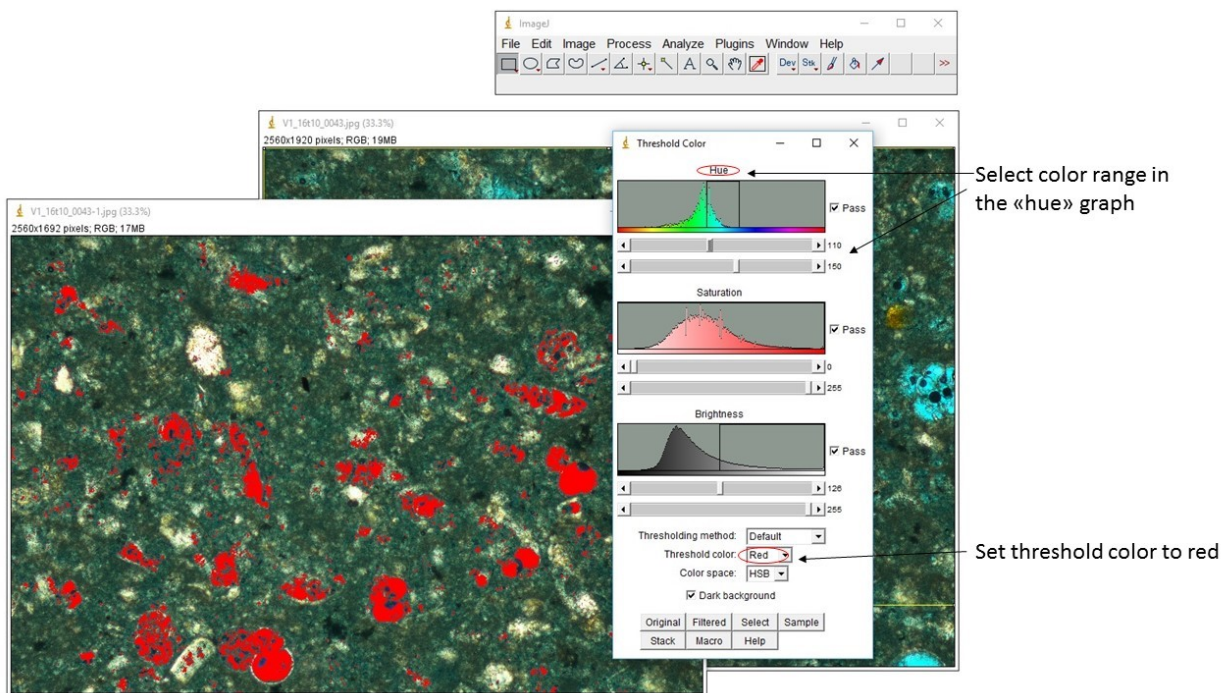
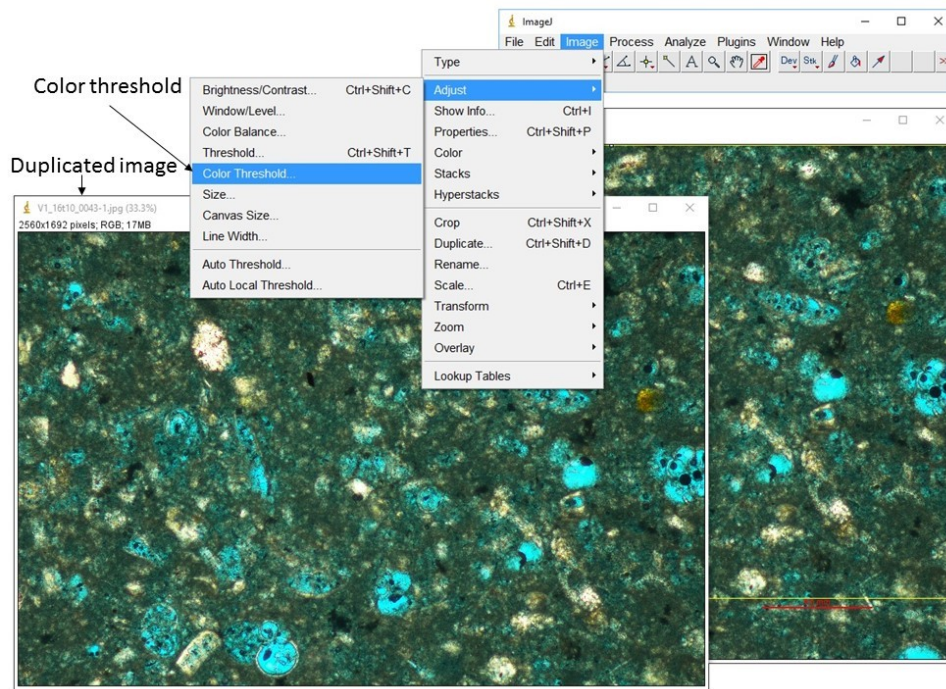
Appendix III: ImageJ workflow

Workflow for photomicrographs

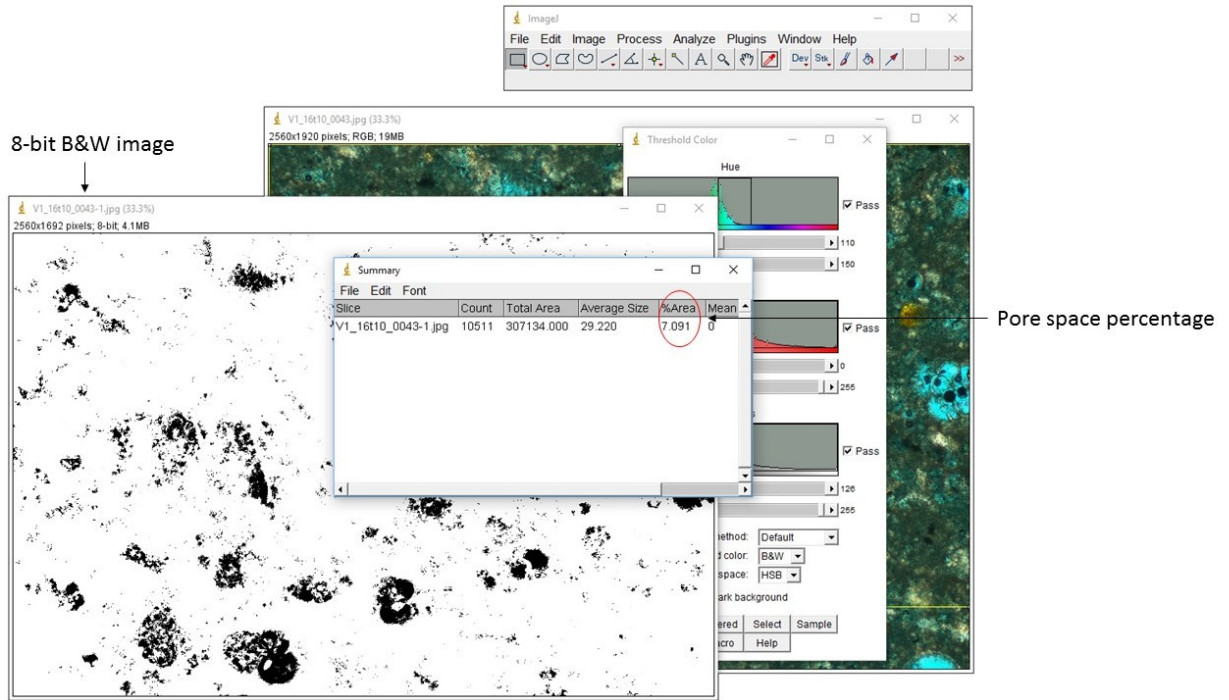
1. The color image is imported to ImageJ, and the scale is set using the “line tool”. The length of the line is given in pixels, and the known distance is plotted in the “set scale” window found under the analyze-tab.



2. To minimize errors in the measured area the red scale bar already in the photomicrograph has to be excluded. This is done by duplicating the relevant area of the photo. Area is chosen with the rectangular tool, and duplicated by clicking “duplicate” in the image-tab.
3. The color threshold is adjusted so that the clear blue (epoxy filled pore space) is selected with a red threshold color, using the “hue” graph. When the covering of the blue area is satisfying, the threshold color is shifted to black and white – B&W.

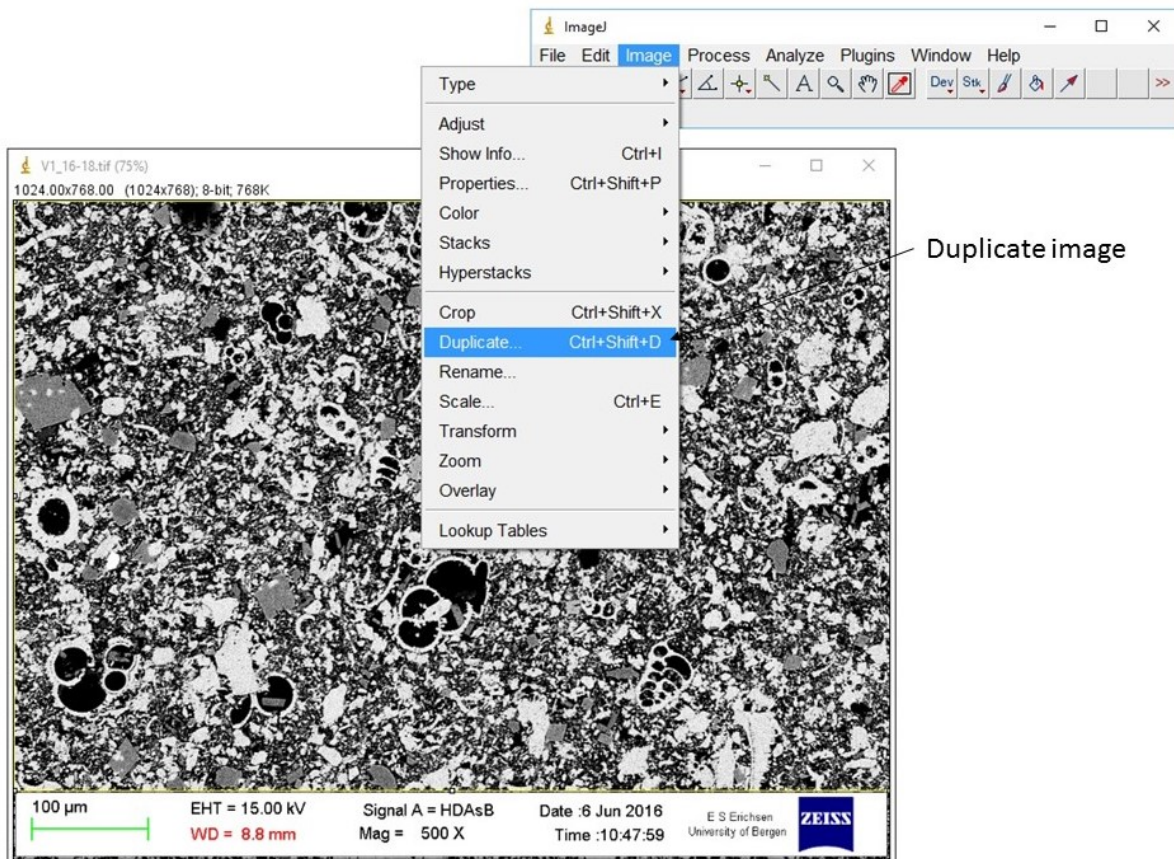


- The image is converted to an 8-bit (B&W) type to enable counting of pore space/particles by clicking “8-bit” under “type” in the image-tab.
- By clicking “analyze particles” under the analyze-tab, choose the particle sizes to be included, and click “ok”. The pore space percentage is calculated from the amount of black “grains” in the photo.

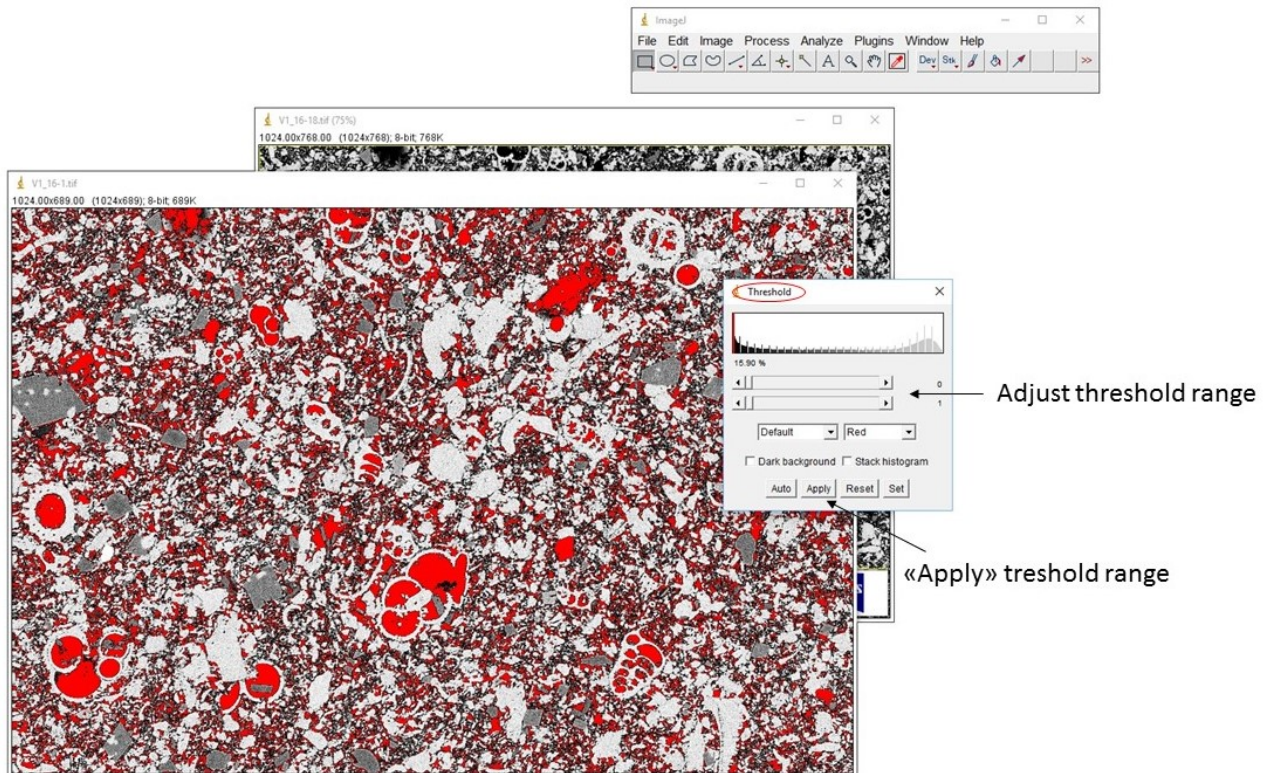


Workflow for BSE-SEM images

1. The black and white BSE-SEM image is imported, and the scale is set the same way as for the colored photomicrograph.
2. The legend-bar at the base of the image is removed by duplicating the relevant area of the image.



3. Threshold is chosen so that only the totally black areas (which represent pore space) are covered.



4. The image is converted to 8-bit to enable counting of pore space/particles, the same way as for the photomicrographs.
5. The pore space percentage is calculated from the amount of black grains in the photo, just like it is for the microphotographs. Click “analyze particles” under the analyze-tab, choose the particle sizes to be included, and press “ok”. The percentage is shown in the %Area column in the result table.

